THE EFFECT OF A DILUTE, DRAG-REDUCING MACROMOLECULAR SOLUTION ON THE TURBULENT BURSTING PROCESS

By

GEORGE L. CUSTER DONOHUE

Bachelor of Science in Mechanical Engineering
University of Houston
Houston, Texas
1967

Master of Science
Oklahoma State University
Stillwater, Oklahoma
1968

Submitted to the Faculty of the
Graduate College of the
Oklahoma State University
in partial fulfillment of
the requirements for
the Degree of
DOCTOR OF PHILOSOPHY
May, 1972

THE EFFECT OF A DILUTE, DRAG-REDUCING MACROMOLECULAR SOLUTION ON THE TURBULENT BURSTING PROCESS

Thesis Approved:

W. A. Iiederman Jr.
Thesis Adviser

H. B. Brooke

Dennis K McLaughlin

R. T. Lowery

Ernest M. Hodnett

D. D. Durham
Dean of the Graduate College

ACKNOWLEDGMENTS

I would like to personally thank my adviser, Dr. William Tiederman, for his excellent guidance throughout my research. I would also like to thank Dr. John Wiebelt and Dr. Dennis McLaughlin for many hours of discussion about laser anemometers, Mrs. Judy Lambert for typing this manuscript, and my wife Andreana for putting up with me. Part of my graduate study was financed by a National Defense Education Act Fellowship, which was greatly appreciated.

TABLE OF CONTENTS

Chapter		Page
I.	INTRODUCTION	1
	The Drag Reduction Phenomena	2
	Turbulent Wall Structure	5
	Scope of the Present Study	8
II.	EXPERIMENTAL TECHNIQUES	11
	Water Channel and Circulation System	11
	Flow Visualization	12
	Flow Visualization Techniques	12
	Burst Counting and Streak Spacing	14
	Laser Velocimeter	15
	Laser Velocimeter Techniques	16
	Reference-Scatter	17
	Scatter-Scatter Systems	20
	Laser Data Recording and Processing Equipment	22
	Sample Size Estimates	26
III.	EXPERIMENTAL DATA	29
	Qualifying Data	31
	Friction-Reduction Measurements	34
	Bursting Rates and Streak Spacing in a Drag-Reducing Solution	37
IV.	DISCUSSION	41
	Nondimensional Groupings Used to Characterize Drag Reduction	41
	Discussion of Drag Reduction Mechanisms	44
	Laser Velocimtery	48
V.	SUMMARY AND CONCLUSIONS	51
	Summary	51
	Constant Flow Rate Comparison	51
	Constant Wall Shear Comparison	52
	Conclusions	53
BIBLIOGRAPHY		55

Chapter Page

APPENDIXES 60

A. LASER PROBE VOLUME GEOMETRY 60

B. SCATTERING PARTICLE FREQUENCY RESPONSE 62

C. UNCERTAINTY ESTIMATES 64

D. POLYMER CHARACTERIZATION 67

E. DATA TABULATIONS 72

F. FIGURES AND ILLUSTRATIONS 75

LIST OF TABLES

Table		Page
I.	Number of Realizations Needed for Desired Accuracy	28
II.	Test Conditions Covered in This Study	30
III.	Summary of Results	35
IV.	Comparison of Drag Reduction Onset Parameters	42
V.	LAMIR Velocity Profile Data	73
VI.	Friction-Reduction Data	74

LIST OF FIGURES

Figure		Page
1.	Water Channel and Circulation System	76
2.	Photograph of Water Channel	77
3.	Photograph of Pressurized Storage Container	77
4.	Photograph of Test Section; Dye Slots and Laser Optics	78
5.	Channel Cross Section Optical Arrangement	79
6.	Turbulence Measurements by Spectral Broadening	80
7.	Beam Crossover Fringes	81
8.	Scatter-Scatter Electro-Optical System	82
9.	Unfiltered Doppler Frequency Burst	83
10.	LAMIR Data Processing System	84
11.	High Pass Filtered Doppler Frequency Burst	85
12.	Normalized Channel Velocity Profiles	86
13.	Turbulent Channel Velocity Profile--Law of the Wall Plot	87
14.	Turbulent Channel Velocity Profile--Velocity Defect Plot	88
15.	Typical Velocity Distribution Histogram	89
16.	Axial Turbulent Intensity Profile	90
17a.	Local Mean Velocity Profile in the Viscous Sublayer	91
17b.	Turbulent Channel Velocity Profile--Sublayer ($U^+ = Y^+$)	92
17c.	Nondimensionalized Channel Wall Shear Velocity for Water	93
18.	Photograph of Dye Injected Into Laminar Flow	94
19.	Photograph of Streak Spacing in Water--(U_{avg} = 0.23 ft/sec)	94

Figure Page

20. Photograph of Streak Spacing in Water--(U_{avg} = 0.43 ft/sec) 95

21. Photograph of Streak Spacing in Water--(U_{avg} = 0.69 ft/sec) 95

22. Bursting Rates in Water 96

23. Pressure Gradient Effect on Bursting Rates 97

24. Nondimensional Streak Spacing in Water 98

25. Per Cent Friction Reduction 99

26. Photograph of Streak Spacing in Polymer Solution (U_{avg} = 0.43 ft/sec., 139 wppm PEO) 100

27. Photograph of Streak Spacing in Polymer Solution (U_{avg} = 0.69 ft/sec., 139 wppm PEO) 100

28. Nondimensional Streak Spacing in Water and Polymer Solution 101

29. Bursting Rates in Water and Polymer Solution 102

30. Average Time Between Bursts in Water and Polymer Solution 103

31. Per Cent Bursting Reduction and Per Cent Friction Reduction 104

32. Per Cent Bursting Reduction in Relation to Per Cent Turbulence Reduction 105

33. Probability Density Function and Energy Density Function . 106

34. Relative Signal Amplitude Ellipsoids 107

35. Laser Scattering Angle in Water 108

36. Probe Volume Traverse Scaling Geometry 109

37. Scattering Particle Size Histogram 110

38. Weir Flow Meter Calibration Curve 111

39. Macromolecule Rotating in a Simple Shear Field 112

40. Intrinsic Viscosity $[\eta]$ Extrapolation 112

NOMENCLATURE

A_c channel cross sectional area

$\bar{b}$ time averaged number of bursts

D_H channel hydraulic diameter, $D_H = 2W/(1 + W/H)$

C polymer concentration in weight parts per million

F spatially averaged bursting frequency defined as $F = \bar{b}/\Delta Z \Delta t$

f friction factor, $f = \tau_w / \frac{1}{2} \rho U^2_{avg}$

K pressure gradient parameter defined as $K = \frac{4\nu}{\rho D_H} \frac{\tau_w}{U^2_{max}}$

P static pressure

p(u) probability density

$\bar{M}_{wt}$ weight averaged molecular weight

N number

n index of refraction

R_{11} spatially averaged correlation coefficient defined as $\overline{U(Z)\ U(Z+Z_0)}/\bar{u}^2$

Re Reynolds number, $U_{avg}\ D_H/\nu$

$\bar{T}_B$ average time between bursts, $\bar{T}_B = 1/F\lambda$

t time

U instantaneous streamwise (X) velocity $U = \bar{U} + u$

U_τ wall shear velocity, $U_\tau = (\tau_w/\rho)^{\frac{1}{2}}$

u' rms streamwise velocity fluctuation level, $u' = (\bar{u}^2)^{\frac{1}{2}}$

U^+ nondimensional velocity, $U^+ = \bar{U}/U_\tau$

U_{avg} mass averaged channel velocity

U_f velocity equivalent of the 80 db/decade high pass filter break point

v', w' normal and spanwise rms fluctuation velocities

W channel width

X, Y, Z streamwise, normal and spanwise orthogonal space coordinates

Y^+ nondimensional distance from the channel wall, $Y^+ = Y/(\nu/U_\tau)$

z polymer rms radius of gyration

Greek Letters

Δ difference

$\epsilon(u)$ energy density function for u velocity

η absolute viscosity

η_{sp} specific viscosity $\eta_{sp} = \eta/\eta_s - 1$

η_r relative viscosity $\eta_r = \eta/\eta_s$

$[\eta]$ intrinsic viscosity $\lim_{C \to 0} (\eta_{sp}/C)$ or $\lim_{C \to 0} (\ell n\, \eta_r/C)$

θ laser beam intersection half angle

λ streak spacing

λ^+ nondimensional streak spacing, $\lambda^+ = \lambda/(\nu/U_\tau)$

λ_o wavelength of light in a vacuum

μ mean of a sample space

ν kinematic viscosity of the fluid

ν frequency of light

ρ density of fluid

σ standard deviation of a sample space

τ_w wall shear defined as $\tau_w = \eta \left.\frac{\partial \overline{U}}{\partial Y}\right|_{Y=0}$

Subscripts

DPS dilute polymer solution

L laminar

P particle

S solvent

T turbulent

Special Symbols

$\%_{BR}$ per cent bursting reduction for a constant flow rate,

$$\%_{BR} = \frac{F_S - F_{DPS}}{F_S}$$

$\%_{FR}$ per cent friction reduction for a constant flow rate,

$$\%_{FR} = \frac{\Delta P_S - \Delta P_{DPS}}{\Delta P_S} = \frac{\tau_{w_S} - \tau_{w_{DPS}}}{\tau_{w_S}}$$

$\%_{TR}$ per cent turbulence reduction for a constant flow rate,

$$\%_{TR} = \frac{f_T - f_{DPS}}{f_T - f_L}$$

CHAPTER I

INTRODUCTION

The purpose of this investigation was to experimentally determine if (and if so, how) a drag-reducing macromolecule might modify 1) the production of turbulent kinetic energy in a turbulent wall flow, and 2) the structure of the viscous sublayer. Specifically, dye was injected into the sublayer of a two-dimensional turbulent channel flow in order to visualize the affect that a drag-reducing polymer might have on the spacing and bursting rate of the low speed streaks that are present in the viscous sublayer. An attempt was then made to relate the observed structural changes produced by the drag-reducing polymer to the friction-reduction phenomena.

Friction-reduction (drag-reduction) refers to the decrease in wall shear (pressure drop in pipe flow) at a given flow rate when small amounts (e.g., less than 250 wppm) of certain long-chain molecules are added to a Newtonian solvent. The small amount of polymer does not significantly affect the density or viscosity of the solvent. Friction reduction has been extensively verified over the last ten years and certain characteristics now seem to be generally well confirmed. Two of the most interesting characteristics are that friction-reduction is a wall phenomenon and occurs only when the flow of the Newtonian solvent would be turbulent. Recent studies have also shown that the near wall region is vitally important to the production of turbulent

kinetic energy. These facts provided a strong motivation to study the physical influence of the polymers on the viscous sublayer in order to gain a more complete understanding of both the drag-reduction phenomena and the structure of turbulent wall flows.

The Drag-Reduction Phenomena

Friction reduction was first reported in the open literature by Toms (50) in 1948 and a considerable number of papers have been published since. Many of these have been devoted to the investigation of the integrated characteristics of the effect--for example, the dependence of the drag reduction on the Reynolds number, concentration of the polymer solution, type of polymer, etc. More recently, interest has turned toward study of the turbulent structure in drag-reducing solutions. Hoyt (23) and Lumley (35) have written excellent reviews discussing the important results of most of the drag-reduction studies that have been conducted.

Several properties of drag-reducing solutions are becoming clear. The molecules must be long, flexible, simple and unbranching. A good solvent is one in which polymer-solvent interactions are favored over polymer-polymer interactions, so that the polymer is relatively extended. One of the most striking characteristics of drag-reducing solutions is their tendency to form long, coherent, tenuous filaments. This is apparently due to the fact that the intrinsic viscosity is vastly larger in axisymmetric strain than in simple shear.

The skin friction coefficient and the Reynolds number do not seem to be the proper similarity variables for drag-reducing solutions; therefore, considerable effort has gone into finding a new similarity

parameter containing molecular properties that will characterize the flow. Basically, two different characteristics of macromolecules have been hypothesized as the proper scaling parameter--length and time. Virk (54) hypothesized that the new similarity parameter should be the ratio of the polymer rms radius of gyration to the wall length scale ν/U_τ. Fabula (8) has pointed out that this hypothesis implies that the macromolecule is interfering with turbulence scales considerably larger than the rms diameter of the randomly coiled polymer.

If the polymer solution is modeled as a spring-mass-damper system, a characteristic relaxation time may be calculated for the solution (see Zimm (61)). Seyer and Metzner (49) and Hershey and Zakin (21) have both proposed a ratio of this molecular relaxation time to the wall layer characteristic time (ν/U_τ^2). There have been difficulties correlating a wide range of experimental evidence with this parameter but the two characteristic times are of the same order of magnitude. The difficulty may lie in the fact that the molecular relaxation time is calculated from molecular properties that are often poorly controlled in experimental studies. This parameter is referred to as the Deborah number and is physically very appealing.

Gadd (11) seems to be the first person to suggest that the drag-reduction mechanism may be linked to a suppression of the bursting process in the viscous sublayer. Based on this idea, Walsh (56) performed a detailed analysis of the strain absorbing ability of the molecule and compared this to the turbulent energy diffusion term. His result is essentially a concentration dependent Deborah number. It correlates some data very well, but predicts a concentration dependent critical wall shear which is not found by other investigators.

Virk (53), among others, has noted that for a given polymer series-solvent combination there is a critical wall shear value below which drag reduction does not occur. Substances with the highest molecular weights have the lowest threshold values. It should be noted that the requirements of flow visualization (low wall shear) and drag reduction (high wall shear) are in conflict. In fact, the highest molecular weight polyethylene oxide (the best water soluble drag reducing agent) has a critical wall shear value just below the upper limits on wall shear for good flow visualization.

Perhaps the most interesting characteristic of drag reduction is the fact that it is a wall phenomenon. Fabula (8), measuring the energy spectra in grid generated turbulence, found no difference between a drag-reducing solution and the corresponding Newtonian solvent. Similarly, Goldstein (14) using a laser anemometer found no change in the turbulent intensity at the centerline of a pipe in a drag reducing solution from a non-drag reducing solution. Velocity profiles measured by Virk (54) (hot wire anemometer) and Rudd (47) (laser anemometer) in pipe flows show that the sublayer is thickened and the logarithmic region is merely displaced upward. Specifically, Rudd observed that the linear regions of both the mean velocity and the rms fluctuation velocity were extended further from the wall than in a similar Newtonian flow. The experiments by Wells and Spangler (58) conclusively demonstrated that the polymers have no effect in pipe flow unless they are present in the wall region. They injected a polymer solution at the centerline of a pipe and also through a wall slot. Drag reduction did not begin until the polymer solution injected at the centerline diffused into the wall region; however, the

wall slot injected polymer solution gave drag reduction immediately. This fact has since led many experimenters to use only wall slot polymer injections in their studies and has important application in ship drag-reduction studies.

A central question is now raised that has not been answered. Physically, what are the drag-reducing macromolecules doing to the structure of the viscous sublayer of a turbulent wall flow?

Turbulent Wall Structure

In the last decade, considerable effort has been expended in studies of the physics of turbulent flows and gradually a physical picture is becoming clear (Mollo-Christensen (41)). Turbulent wall layers are of particular interest because all aspects of turbulent kinetic energy production, dissipation, and convection are present. This should be contrasted with free field turbulence, which having once been generated, will slowly decay to smaller and smaller sizes through an energy cascade until it is destroyed by viscous dissipation. In turbulent wall layers, however, the production of turbulence balances with the dissipation so that the turbulence never dies out. Consequently, an understanding of the production mechanism is a necessary step in the understanding of turbulent wall flows. Since Laufer (32) and Klebanoff (26) have shown that virtually all of the production (and dissipation) of turbulence takes place in the region very close to the wall, $Y^+ < 30$, the near wall region deserves special attention.

A series of experiments have been performed in the last decade at Stanford University (reported by Kline, et al. (28) in which the

physical structure of the near wall region of bound turbulent shear flows has been studied. Their visual studies of the viscous sublayer have revealed a longitudinal, streaky pattern aligned in the flow direction. This pattern may be made visible by injecting a tracer into the wall layer. The streaks appear because the tracer collects in low mean speed regions and is washed away in faster regions. All of these characteristics are readily seen when hydrogen bubble time lines are used to visualize the wall region. R_{11} cross correlations have also been formed from instantaneous measurements of the spanwise velocity profile, and these correlations show peaks at spacings comparable to the spacings observed visually. This streaky structure has a non-dimensional spacing (λ^+) that is a fundamental characteristic of the viscous sublayer.

In general, as the streaks move downstream very near the wall, they lift, begin to oscillate, and then chaotically move out away from the wall.. Kim (25) has performed a detailed study of this bursting process and has identified some of the following characteristics.

The velocity fluctuations during the bursting period are well-organized compared with the random background of turbulence. During bursting, the Reynolds stress is much greater than that of the background turbulence. Measurement of the production during bursting and non-bursting periods shows that approximately 70% of all of the production occurs during the bursting period for $Y^+ < 100$.

At about the same time, Corino and Brodkey (5), performing similar visual studies in a pipe, noted that in addition to the bursting process reported by Kline, et al., the lifting and bursting

of the low speed fluid alternated with a rapid downwash of high momentum fluid filling the void left by the burst. A very recent study by Wallace, et al. (55) has shown that both the inward sweeps and outward bursts contribute approximately 70% each to the total production that occurs when the Reynolds stresses are negative. Their study also indicates that the wall layer spends essentially all of its time producing turbulent energy. The large amount of dissipation in the wall layer occurs in the locally intense shear produced in the bursting, downwash process.

Measuring turbulent burst rates and streak spacings is difficult except at very low wall shear velocities. Recently, Rao, et al. (43) have attempted to measure bursting rates in air at much higher wall shear velocities by observing a band-passed hot wire anemometer signal and measuring the time between periods of large amplitude velocity fluctuations. There are many difficulties associated with the conditional sampling of anemometer signals and the significance of their results is not yet clear. They claim to have found, however, that the bursting rates scale on "outer" variables rather than on the "inner" wall parameters suggested by Kline's research. Although these results are not conclusive, it raises the question once again as to whether the production of turbulence is generated at the wall or in the outer regions of the turbulent boundary layer. This controversy has been continuing for many years and some feel that it is the central question in turbulence research today.

This controversy can be avoided, however, by assuming that the basic nature of the turbulent boundary layer energy chain is similar to a negative feedback loop. Within the total cycle, low momentum

fluid becomes unstable and bursts away from the wall giving rise to large scale turbulence in the outer layer. Continuity considerations demand a return flow which sweeps back into the wall region triggering instabilities and more "bursts". In a cyclic process such as this, there is no beginning or end. However, if one could suppress any element of the chain, one could drastically alter the turbulent energy balance.

Several very interesting studies have shown that suppression of the turbulent bursting rate by acceleration (Kline and Schraub (30) and Moretti and Kays (42)) and coriolis forces (Halleen and Johnston (19) and Lezius and Johnston (34)) is accompanied by the flow assuming laminar-like properties. In particular, Halleen's data show that the wall shear stress is reduced simultaneously with the reduction of the bursting rates at a given Reynolds number.

Scope of the Present Study

The large body of evidence indicating that drag reduction is a turbulent wall phenomenon coupled with the data of Halleen (decreasing wall shear with decreasing bursting) and Kim (production of turbulent energy associated with the bursting process) led to this investigation. The concept was to construct a flow facility that would allow visualization of the viscous sublayer under the influence of a drag reducing macromolecule. Specifically, the channel was designed to allow the visualization of the characteristic low speed streak spacing and bursting rates by means of a wall slot dye injection technique. This technique is practically limited to wall shear velocities of less than 0.04 ft/sec in water. This is a significant limitation because the

best water soluble drag-reducing polymer (the highest molecular weight polyethylene oxide) has a critical wall shear value of approximately 0.01 ft/sec when it is handled with care to avoid degradation. Consequently, our flow visualization studies have been limited to relatively small amounts of drag reduction (i.e., 26 per cent).

It was crucial to determine the amount of drag reduction that was taking place in the channel when the motion picture data was being taken. Since the pressure drop in the channel was too small to measure accurately, the reduced wall shear in the channel was determined from pressure drop measurements in adjacent pipes and a correlation of friction reduction that is independent of hydraulic diameter. This correlation was established by measuring the amount of friction reduction which occurred when the same solution flowed through a 0.425-inch diameter pipe, a 0.835-inch diameter pipe, and the 2.93-inch hydraulic diameter channel. The amount of friction reduction in the pipes was determined by pressure-drop measurements while the friction reduction in the channel was determined from measurements of wall shear. Since the dilute polymer solution has essentially a Newtonian viscosity in simple shear, the channel wall shear was determined by measuring the velocity gradient at the wall with a laser velocimeter. The correlation established here is in agreement with previous investigations which have shown that the percentage of friction reduction is a unique function of the wall shear for a given solution.

The section on Friction-Reduction Measurements gives the details of the per cent drag reduction correlation used to determine the reduced wall shear values in the channel. Table II gives an overview of all of the visual and laser velocimeter data that was obtained in

this study. The major results in the form of wall shear velocities, bursting rates and streak spacings may be found in Table III and Figures 28, 29, 30 and 31. The major conclusions which are largely based on these results are given in Chapter V.

CHAPTER II

EXPERIMENTAL TECHNIQUES

This chapter presents the details of the channel flow facility, flow visualization and data reduction techniques. The individual realization laser velocimeter system is also described and compared to other laser systems.

Water Channel and Circulation System

Figure 1 shows a sketch of the water channel and its circulation system. The channel, the upstream settling chamber, and the downstream constant head chamber are made of ½-inch plexiglas; the rest of the flow loop is constructed of stainless steel. The upstream storage container is a 600 gallon pressurized tank. By controlling the pressure and flow rate of compressed air entering the tank, a constant flow of water through the channel is maintained. The flow loop is operated from a central control point by the use of remotely controlled pneumatically actuated ball valves. Water enters the settling chamber from the pressurized tank through a 3½-inch diameter stainless steel pipe and then flows through a perforated plexiglas baffle plate used to disrupt the entering jet. Next, the flow must pass through a ½ inch x ½ inch plastic honeycomb and a 64 mesh stainless steel screen before entering the remainder of the settling chamber (24 inches long, 18 inches wide, and 18 inches high).

The entrance to the channel from the settling chamber is a two-dimensional bell mouth with a 3 inch radius. The side walls of the channel were made from a continuous piece of plexiglas 100 inches long (L) and 17.75 inches high (H). With a width of 1.59 inches (W), the channel has an aspect ratio (H/W) of 11 and a length-to-width ratio (L/W) of 63. The flow exits from the channel into an overflow, constant head tank (12 inches long by 12 inches wide). The water flow rate is measured by noting the water height above a weir located on the constant head overflow tank. A 600 gallon open-topped tank catches and stores this overflow during the course of the runs. At the end of a run, the upstream tank is depressurized and the water in the downstream tank is allowed to gravity drain back into the upstream tank at which time the loop may be recycled.

Dye slots are located 44 and 51 channel widths downstream from the channel entrance. The dye is injected by gravitational feed into the wall layer through 0.005 inch slots. Velocity profiles were taken just downstream of the first dye slot. This system was designed to use no pumps in order to minimize polymer degradation and flow disturbances. The make-up water is filtered tap water and the entire flow loop is thoroughly flushed after each polymer solution is discarded. Operating times vary from approximately 20 minutes at a Reynolds number of 6000 to approximately 7 minutes at a Reynolds number of 18,000.

Flow Visualization

Flow Visualization Techniques

The flow visualization techniques in this study are similar to the ones described by Kline and Schraub (30) and Kline, Runstadler,

and Reynolds (29). A dilute (8%) solution of blue food coloring carefully introduced into the boundary through a thin nonperturbing slot in the wall has been shown to be a good method of visualizing the structure of the viscous sublayer. The slots, which are approximately 7 inches long, were machined normal to the wall surface and in the spanwise direction. A needle valve and adjustable head gravity feed system combine to produce a uniform rate of dye injection. The upstream dye slot was used for measuring low-speed-streak bursting rates. It was masked to a 0.67-inch span so that only a few low speed streaks were marked and thus these few streaks do not obscure each other in the bursting process. The downstream dye slot was left unmasked and was used for measuring streak spacing.

Figure 5 is a cross section of the channel showing the split image optical arrangement used in photographing the low speed streak bursting. The lighting, which is provided by a bank of fluorescent lights (160 watts), is diffused by a translucent plate before it shines upon the test section area. Additional lighting is provided by a 500 watt tungsten filament overhead projector aimed at a 45^{o} mirror directing the light up from the bottom to the top of the channel. With this arrangement of lighting and mirrors, the camera sees a split image with the top view looking down through the channel to observe the streaks lifting away from the wall and with the bottom view looking directly through the channel to see the 0.67 inch dye slot. Streak spacing is photographed using only the fluorescent back lighting and is viewed directly through the channel.

The camera used to record the visual data was a Bolex H16 Reflex with a 75mm f1.9 lens. Depending upon the flow rate, the framing rate

was 16, 32, or 64 frames per second. A high speed Ektachrome film (Kodak 7242) with an ASA rating of 125 was used. All films were spatially calibrated with a grid which has 10 divisions to the inch. Bursting rate films were separately timed to ± 0.01 minutes with an electric timer.

Burst Counting and Streak Spacing

All films were analyzed in slow motion with a 16mm Bell & Howell Time & Motion Study projector. Streak spacing was measured by randomly stopping the film and counting the number of streaks visible in a 4 inch span. The streaks were counted along a line which is parallel to the dye slot and from 1½ to 3 inches downstream of the dye slot. The counting location is dependent upon the distance it takes for the dye to collect into identifiable streaks and yet close enough to the marking origin that bursting has not begun. A consistent location was established for each flow condition. Having counted the number of streaks in a 4 inch span from randomly sampled frames, an average streak spacing was calculated for each flow condition. These counting procedures give the same nondimensional streak spacings as found by others and are believed to be consistent with the counting philosophy used by previous investigators.

The field of view over which the low speed streak bursts are counted is approximately 8 inches long by 0.67 inches wide. The number of observed bursts were counted by 4 independent and unbiased observers for each flow condition. Counts were made with the film running both forward and backward. Based on all of this data, average bursting rates were computed for each flow condition. Bursting rates

in the water without polymer were found to be in agreement with the favorable pressure gradient data of Schraub (30).

Laser Velocimetry

Initially, the laser anemometer was to be used in measuring both mean velocity and axial intensity profiles in both water and dilute polymer solutions. Due to equipment limitations the study was limited to an initial survey of the mean velocity and turbulent intensity profiles in water and only one mean velocity and turbulent intensity point in the dilute polymer solution. This point was used to obtain a measure of the wall shear in the polymer solution and to confirm that the per cent friction reduction is a unique function of the wall shear velocity.

Practical difficulties involved in operating the more conventional continuous Doppler signal laser anemometer systems in highly fluctuating turbulent flow fields led to the development of a new laser anemometer measuring individual realizations (LAMIR). This system differs from other laser anemometer systems in that it accurately measures the Doppler frequency from individual particles passing through the scattering volume. The system was found to essentially eliminate two of the limitations of continuous signal laser anemometers (i.e., the Doppler ambiguity and signal "drop out"). This development is an important result even though it is not necessarily crucial to the major objective of this investigation.

However, it is difficult to measure the velocity in dilute polymer solutions. In particular, Friehe (10) has recently completed an extensive study to determine the applicability of hot wire and impact

pressure probes in dilute polymer solutions and has found that the most common velocity measuring techniques are ambiguous.

Hot wire anemometers are based on the fact that the heat transfer from a wire is proportional to the square root of the Reynolds number based upon the diameter of the wire. Friehe found that this relation no longer holds in solutions of viscoelastic polymers. In fact, he found regions of the Reynolds number range (e.g., at velocities under 4 feet/second) where the heat transfer coefficient was independent of the Reynolds number.

Impact pressure probes were found to be in error as the ratio of probe diameter to velocity was decreased (i.e., the characteristic "time" of the probe was decreased). This problem may be attributed to the "elastic" nature of the solution at high shear rates. The normal calculation of velocity based on the difference between the total and static pressures is questionable. Consequently, both of these measurement techniques are undesirable for measuring turbulent velocities close to a wall, even though many of the previous studies of dilute polymer solutions have used either impact tube or hot wire velocity measuring techniques. Laser velocimeters are able to accurately measure fluid velocities at a point in the flow field without altering the flow field or being affected by the type of fluid (as long as the fluid is not opaque).

Laser Velocimeter Techniques

Basically two electro-optical systems are presently being employed in laser velocimetry--reference-scatter and scatter-scatter. The former, first introduced by Yeh and Cummins (60) and used most

notably by Goldstein and Kried (16), can be used in a relatively straight-forward manner to measure velocities in laminar flows under carefully controlled laboratory conditions. Recently, however, attention has been directed toward measuring velocities in turbulent flow situations. Here the laser velocimeter offers the advantage of small probe volume, linear response characteristics, one-dimensionality, no adjustable calibration constants and no flow perturbation. The most notable attempts at measuring turbulence quantities have been those of Goldstein and Hagen (15) and Lumley, et al. (36). Both teams used a reference-scatter optical system similar to the one introduced earlier by Goldstein and Kried (16).

The common feature of essentially all of the electro-optical systems presently being used to measure turbulent velocities is that the Doppler signal is basically continuous. A relatively continuous signal is achieved by adding a large number of small scattering centers to the fluid. The objective is to have a large enough number of scattering centers in the probe volume to always yield an operational signal to noise ratio. Brief descriptions of continuous wave reference-scatter and scatter-scatter systems are presented here in order that the advantages of an individual realization scatter-scatter laser anemometer system may be pointed out.

Reference-Scatter. A reference-scatter system works as follows: A reference beam (approximately 1% of the laser light) and a scattering beam (approximately 99% of the light) are focused to a common point in the flow field. When a small particle (scattering center) passes through this common focal point (scattering volume) light is scattered

by the particle. Some of the light that is scattered is along the same direction as the unscattered reference beam but is of a slightly Doppler-shifted frequency. When these radiations strike the face of a photodetector and their intensities are approximately equal, the frequency difference between the scattered and unscattered radiation is obtained. For this optical arrangement, only one component of velocity is obtained and that component is the velocity of a particle in the plane of the two beams and normal to the bisector of the angle between the two beams. The difference frequency is (16) (37) (46)

$$\nu_D = (2n \sin \theta/\lambda_o)U_p$$

where $\nu_D = \nu_{scattered} - \nu_{unscattered}$

U_p = velocity of particle

λ_o = wavelength of light (6328Å)

n = index of refraction of fluid

θ = beam intersection half angle

In practice, more than one frequency is typically observed with this system. The signal received by the photodetector is the sum of the signals produced by all of the scatter centers in the scattering volume (and many are needed) at each instant; each has the same frequency, but a phase dependent on its origin in the volume as well as an intensity dependent on the particle size and place in the scattering volume. As the scatterers leave the scattering volume and new ones enter, the signal loses coherence. Lumley (36) and Greated (18) have pointed out that this random phase fluctuation (sometimes called the Doppler ambiguity) presents a fundamental high frequency limitation for all continuous wave laser anemometer systems.

Other factors that may contribute to a loss of coherence are velocity gradients in the scattering volume, finite receiver aperture, turbulent velocity fluctuations and electronic noise. These influences all tend to decrease the signal-to-noise ratio and broaden the range of frequencies observed at the photomultiplier tube in a continuous wave system.

Goethert (13) has pointed out a potentially more serious limitation to continuous wave systems, however. His analysis indicates that signal "drop out" (the momentary loss of frequency information) can be caused by longitudinal velocity gradients and may be intrinsic to all continuous wave systems. Signal "drop out" presents a major problem in the interpretation of turbulence intensity and energy spectra. In fact, considerable signal "drop out" difficulty has been experienced by researchers who have tried to utilize continuous wave laser anemometers to study regions of high turbulence intensity. This problem may possibly be overcome if high seed densities and/or expensive conditional sampling electronics are utilized.

Besides longitudinal velocity gradients, signal "drop out" may be caused in continuous wave systems by insufficient scattering centers in the probe volume or the presence of particles whose size gives inefficient hetrodyning. The amount of light that a particle may scatter depends greatly upon its diameter. In a reference-scatter system, efficient hetrodyning occurs only when the scattered light is of the same magnitude as the unscattered reference light. Particles that are too large or too small will only add noise to the system. This fact may present a more severe cleanliness requirement on the fluid than now exists for hot wire anemometers.

In order to avoid the problems involved in tracking the low SNR, frequency broadened, instantaneous frequency as it fluctuates in a turbulent flow, Goldstein and Hagen analyze the frequency spectrum of the photodetector output. The peak of the spectrum is taken as the mean velocity. To measure the turbulent intensity, the frequency spread (due to broadening) about the mean frequency for laminar flow is subtracted from the frequency spread about the mean frequency in turbulent flow (see Fig. 6) and the increased spread is attributed to the turbulent intensity.

At the pipe centerline, the turbulence is approximately Gaussian and the turbulent intensity is small (approximately 4% of the local mean), thus this method works reasonably well. As the wall is approached, however, the turbulent intensity may become as high as 40% of the local mean and is no longer closely approximated by a Gaussian distribution. Frequency broadening under these conditions seriously limits the accuracy of mean velocity and turbulence intensity measurements.

Scatter-Scatter Systems. An alternative optical system to the one suggested by Goldstein is proposed by Rudd (46). The scattering physics of this system can be explained in terms of an interference fringe pattern (see Fig. 7). Mixing two equal intensity spatially and temporarily coherent light beams produces a set of interference fringes at the focal point (i.e., beam intersection point or scattering volume). (These fringes may actually be visualized by projecting the image of the scattering volume with a concave lens that is focused on the beam intersection point.) When a scattering center crosses this set of fringes in the scattering volume, it produces a frequency

corresponding to the rate at which the fringes are crossed. From this standpoint, the particle is either in or out of a fringe, independent of the viewing angle. The reference-scatter signal is always limited by the amount of scattered light that it may receive. With the scatter-scatter system, however, one looks at only scattered light from as large a solid angle as possible. This viewpoint leads to an improved electro-optical system that greatly increases the signal-to-noise ratio and essentially eliminates frequency broadening due to finite receiver aperture (37) and signal drop outs caused by particle size variations. This optical system was selected because of its high signal-to-noise ratio and is shown schematically in Figure 8. Even though this system gives a much better signal-to-noise ratio, it still suffers the limitations of Doppler ambiguity, signal drop out from insufficient seed, and signal drop out from longitudinal velocity gradients when operated with a continuous signal. For these reasons, a new scatter-scatter technique was developed.

Due to the increased signal-to-noise ratio, the addition of scattering centers was found to be unnecessary. Residual impurities in typical working fluids are enough to yield very high SNR signals. Specifically, the Doppler signal of individual particles passing through the scattering volume can be observed. Each separate particle that passes through the probe volume provides an instantaneous, randomly sampled realization of the velocity at that point in space. Repeated sampling builds up the probability density function of the velocities at a given location in the turbulent flow field. This function can then give unambiguously and to a given probable accuracy the mean velocity, rms fluctuation level and energy density function.

The practical advantages of the individual realization scatter-scatter system used in this study over the continuous wave systems used by other investigators may be summaries as follows: 1) The signal-to-noise ratio is greatly increased due to the large amount of scattered light that may be collected and also due to the fact that no direct laser light (which contributes a large amount of noise) is received by the photomultiplier tube; 2) The signal received is a single frequency and is not broadened by multiple scatter centers in the scattering volume or by the finite viewing angle; 3) Residual impurities in the flow are sufficient as scattering centers and neither seeding nor a high level of cleanliness is required; 4) By accurately and unambiguously measuring individual particle velocities, there are none of the averaging ambiguities that are associated with all of the other common turbulence measuring techniques; 5) This system is not affected by signal drop out and random pahse fluctuation ambiguities associated with continuous wave laser anemometers.

Laser Data Recording and Processing Equipment

With the scatter-scatter individual realization laser velocimeter system, one can observe individual particles passing through the crossed laser beams. The photodetector receives three different types of signals depending on whether the particle 1) passes through only one of the laser beams, but totally outside of the beam intersection volume, 2) passes partially through the beam intersection volume, or 3) passes through the center of the beam intersection volume. These signals will appear at the output of the photodetector as 1) a dc excursion without any "Doppler" frequency superimposed, 2) a "Doppler"

frequency burst with only a few Doppler cycles and/or a skewed intensity envelope, or 3) a "Doppler" frequency burst with a Gaussian intensity envelope and approximately 40 cycles (see Figure 9). The latter signal contains a sufficient number of cycles to provide an accurate measurement of the "Doppler" frequency. The "Doppler" frequency is obtained by measuring the time required for a given number of "Doppler" cycles. In order to do this, the signals seen by the photodetector must be selected and conditioned so that the "Doppler" frequency is the only frequency left to be measured. Essentially this means the signals must be filtered to remove the dc excursions and the bursts with an insufficient number of "Doppler" cycles must be rejected.

The data processing system for measuring the "Doppler" frequency is shown in Figure 10. Since the photomultiplier is a current source, the PMT output voltage must be observed across a load resistor. Normally, one would use a large R_L to get a large output voltage. Care must be taken in selecting an R_L, however, because the load resistor acts in conjunction with the photomultiplier tube and the co-axial cable capacitance to form a low pass filter. For most of this work, a load resistor of 61.9 k ohms was used. The voltage across R_L is then fed to a Hewlett-Packard Model 450A instrumentation amplifier to provide an additional 40 db of gain and impedance isolation. The amplified signal is then sent through a first-order high-pass filter to remove the dc bias of the burst (pedestal voltage) so that the signal may be recorded. The break point on this filter is set as low as possible so that no signal information is lost; however, the voltage excursions must not saturate the recorder. In turbulent flows, especially near a wall where the rms fluctuation level may be 40% of the

local mean velocity, the high pass filter break point f_{1L} is set approximately one order of magnitude below the estimated average velocity frequency.

The high pass filtered signal is then recorded on a Sanborn/Ampex Model 2000 recorder. A recording speed of 60 ips is required to record the relatively high "Doppler" frequencies (up to 150 khz). The tape is played back at 7½ ips in order to allow the use of audio frequency electronics. The signal must now be filtered again since the initial filtering was minimal. Selection of the proper band-pass filter cut off frequencies is critical to the proper evaluation of the data. A Krohn-Hite Model 330M audio frequency active (fourth order) band-pass filter is used. The low pass break point (f_{2H}) is conveniently set at some arbitrary frequency well above the expected average frequency. This is done in order to help reduce any high frequency electronic noise and/or tape recorder induced noise (e.g., residual 240 khz recording oscillator frequency). The high pass break point (f_{2L}) is used to eliminate all of the pedestal voltage of the frequency bursts and the false signals of particles passing through the laser beams but outside of the scattering volume. Initially, f_{2L} is set at the same value of f_{1L} and then adjusted upward until the signal is "clean" enough for additional data processing. In any case, f_{2L} should not be so high that it would significantly affect the statistical determination of the velocity fluctuations. A rule of thumb has been to keep f_{2L} below the estimated standard deviation from the estimated mean. If f_{2L} is found to have been set too high, the data should be reduced again using the new estimates of the mean (μ) and the standard deviation (σ) to establish a new f_{2L}. For measuring higher moments

than the mean, f_{2L} must be set even lower and extensive precautions must be taken in the data reduction scheme.

The frequency burst now appears as shown in Figure 11. In order to accurately measure this Doppler frequency, the signal is sent through a General Radio Type 1396-A tone burst generator where typically eight cycles of the frequency burst are selected. The period for these eight cycles to pass is represented as a positive gate voltage. In some instances the gate remains open for long periods due to an insufficient number of high SNR cycles in the frequency burst. These readings are rejected by continuous oscilloscope monitoring of the gated frequency bursts. The gate time data is only recorded when visual monitoring of the signal confirms that the gated signal contained eight cycles from within a given frequency burst. The time duration of this positive gate voltage is measured in microseconds by a Beckman/Berkeley Universal Counter, Model 7360. This data appears as a four-digit number and is recorded on computer cards. The computer is then used to calculate the value of the randomly selected, instantaneous velocity realizations by knowing the time required for a given number of cycles to pass.

This system presents a single frequency to be measured and has none of the frequency broadening effects of the previous continuous wave systems. Actually, when measured, it is the average frequency over the time the particle is in the scattering volume. Thus, fluctuations of the particle while it is in the probe volume will be averaged out. This becomes an important consideration only when the probe volume is large relative to the size of the turbulence microscale. For this work the microscale is estimated to be approximately

0.1 inches from the data of Uzkan. The probe volume size is calculated in Appendix A to be approximately 0.004 inches in diameter by 0.02 inches long. Hence the major source of uncertainty is reduced to whether or not the scattering particle accurately follows the fluid velocity. The inaccuracies imposed by the ability of a particle to follow all of the turbulent fluctuations is discussed in Appendix B.

Sample Size Estimates

How many individual realizations are needed to give an accurate estimate of the mean velocity? To answer this question, one can use a unique property of the measurement system (i.e., the noncontinuous manner in which the data is obtained). Measurements of velocity are obtained only when a particle passes through the scattering volume. These velocity realizations occur at approximately one second intervals under these particular experimental conditions. They occur randomly in time. Here we have a good random sampling of velocities at a point in space and can use well established statistical techniques to estimate the amount of sampling required to provide a given accuracy. Even though turbulent fluctuations are not Gaussian, one can still estimate the sample size necessary to produce an estimate of the mean with a given accuracy by assuming that the fluctuations are normally distributed. For example, assume

$$\sigma \sim u' .$$

Then a 95% confidence interval on the mean is given by

$$\bar{U} - 1.96\, u'/\sqrt{N} \leq \mu \leq \bar{U} + 1.96\, u'/\sqrt{N}$$

where μ is the true mean velocity and $\bar{U}$ is the measured estimate of the mean velocity. Rearranging:

$$|(\mu - \overline{U})/\overline{U}| \leq 1.96 \left(\frac{u'}{\overline{U}}\right)/\sqrt{N}$$

Simplifying

$$N \sim 4(u'/\overline{U})^2/(\Delta\overline{U}/\overline{U})^2$$

where N equals the number of statistically independent samples from a normal distribution. Table I shows some estimates of the sample size required to obtain accuracies of 10, 5, and 2 per cent at various locations in a turbulent pipe flow. Similar calculations may be performed for any statistical moment desired.

TABLE I

NUMBER OF REALIZATIONS NEEDED
FOR DESIRED ACCURACY

$\pm \Delta\overline{U}/\overline{U}$ (accuracy desired)		10%	5%	2%
Location	Fluctuation Intensity ($u'/\overline{U}$)*			
Center Line	0.03	1	2	9
log region $Y^+ = 30 - 100$	0.15	9	36	225
Sublayer $Y^+ = 10$	0.30	36	144	900

* Ref - Laufer (32)

CHAPTER III

EXPERIMENTAL DATA

This chapter presents the experimental data obtained from both water and dilute-polymer solution flows in the channel. Briefly, the experiments can be classified in the following way. Mean velocity profiles were measured with the LAMIR in order to demonstrate that the water channel yielded standard two-dimensional fully developed turbulent channel flow. Use of the LAMIR in drag-reducing dilute polymer solutions was limited to determination of the wall shear at one Reynolds number. This measurement of friction reduction in the channel was combined with pressure drop measurements in 0.835 inch and 0.425 inch diameter pipes to establish a correlation for friction reduction which is independent of hydraulic diameter. This correlation was then used along with simultaneous pressure drop measurements in the 0.835 inch pipe to infer the amount of friction reduction occurring during the flow visualization studies.

Flow visualization studies were made in water at three Reynolds numbers and in dilute-polymer solutions at flow rates equal to the water tests. Table II is a summary of the test conditions and the data acquired during the study. It should be noted that bursting rate measurements were conducted with a bell-mouth entrance for which the water flow was a standard 2-D channel flow and with a square-edged entrance for which the velocity profile was skewed.

TABLE II

TEST CONDITIONS COVERED IN THIS STUDY

Description	Mass Averaged Velocity (ft/sec)	LAMIR[d] Velocity Profile	LAMIR[d] Wall Slope	Visual Burst Rate (F)	Visual Streak Spacing (λ)	Polymer Concentration C (wppm)
-D, bellmouth ntrance, water	0.23	4[a]	5	7	7	
	0.43		5	7	7	0
	0.69	4	5	7	7	
-D, bellmouth ntrance, polymer un #1[b]	0.23			8	8	
	0.43			8	8	
	0.69		6	8	8	139
-D bellmouth ntrance, polymer un #2[b]	0.23			9		
	0.43			9		139
	0.69		6	9		
quare entrance, ater[c]	0.43			1		
	0.69	3		1		0
	0.87			1		
quare entrance, olymer[c], un #2[b]	0.43			2		
	0.69			2		100
	0.87			2		

xperiment Number	Date	Temperature T ± 0.5 °C	Kinematic Viscosity $\nu \times 10^5$ (ft^2/sec)	Type of Data
1	11/18/70	18.5	11.8	Visual
2	11/18/70	18.5	15.2	Visual
3	06/10/71	24.0	10.4	LAMIR
4	06/29/71	27.5	9.2	LAMIR
5	07/23/71	27.0	9.3	LAMIR
6	09/24/71	22.0	14.6	LAMIR
7	10/01/71	25.5	9.6	Visual
8	10/01/71	25.5	13.5	Visual
9	10/01/71	25.5	13.5	Visual

= Numbers represent the experiment number.
= 1, 2, . . . indicates first, second, . . . run through the channel after a fresh polymer mixture was prepared.
= LAMIR data indicated a skewed velocity profile.
= LAMIR velocity profile data is presented in Table V.

Qualifying Data

Mean velocity profiles were measured with the laser velocimeter at the high and low Reynolds numbers of this study (18,000 and 6,000 respectively). The Reynolds number is based upon the channel hydraulic diameter (2.93 inches) and the mass averaged velocity. The scattering centers were predominantly 25 micron sand particles that satisfactorily respond to essentially all of the turbulent velocity fluctuations (see Appendix B).

The velocity profiles were measured 47 channel widths from the entrance and are shown in Figure 12 normalized with their centerline velocities. Figure 13 shows the same mean velocity distributions in "law of the wall" coordinates and Figure 14 shows the data plotted in the velocity defect form.

In addition to mean velocity profiles, the data allow us to make estimates of the higher statistical moments at each point in the flow field. Figure 15 shows a typical velocity distribution histogram that is obtained by the laser velocimeter. Estimates of the mean velocity, fluctuation intensity (see Figure 16) and the energy density distribution may be made from this data. However, a more refined laser system is needed to obtain a sufficient number of samples to thoroughly survey the statistical properties throughout the flow field.

The channel velocity and turbulent intensity profiles are shown compared to the findings of Laufer (31), Comte-Bellot (4), and Clark (3), who have measured the properties of fully developed turbulent channel flows. Considering the limited sample sizes (see Table V) the data is in good agreement with their results. It should be emphasized

that the accuracy of these velocity measurements can be improved as illustrated in Table I by simply increasing the number of realizations.

The wall shear velocities used throughout this study (except Figure 13) were computed from the velocity gradients measured in the $U^+ = Y^+$ region next to the wall (see Figure 17a). When the data was "forced" to fit $U^+ = 5.6 \log Y^+ + 4.9$, in Figure 13 a different wall shear velocity was found and deviation from $U^+ = Y^+$ in the sublayer was observed. This deviation is in general agreement with the findings of Schraub for pressure gradient turbulent wall flows. In particular, he suggested that the wall shear velocity computed from the wall slope should be the proper scaling factor except when "fitting" the data to the "law of the wall". The wall shear velocities computed from the wall slopes in Figure 17a were normalized with their mass average velocities and plotted as a function of their respective Reynolds numbers in Figure 17c. This function now enables one to find the wall slope wall shear velocity in this channel knowing the channel Reynolds number.

It should be pointed out that it is more proper to use a wall shear velocity computed from the velocity gradient in the sublayer for characterizing turbulent wall structure than a wall shear velocity found from a "law of the wall" fit (as demonstrated by Schraub) or a friction factor correlation (which averages channel corner effects into the computed local wall shear). Thus, the correlation shown in Figure 17c was used throughout the study to determine the wall shear velocities corresponding to the solvent (water) visual data. Figure 17c was also used in determining the amount of friction reduction for

the dilute polymer channel flows. Its use in this capacity is described later in this chapter.

Motion pictures were taken at the flow rates indicated in Table II. Figure 18 shows the dye injection for laminar flow. Notice that the dye sheet is smooth and that there are no streaks or flow perturbations induced by the dye slots. This figure shows dark dye on a light background. The rest of the dye photographs are negative prints and show the dye as white on a dark background. Figures 19 through 21 show these photographs made from the 16mm movie films of the water viscous sublayer. The resultant bursting rates are shown in Figure 22. The brackets on all data are estimates of the 95% confidence intervals (see Appendix C for the error analysis).

The bursting rates in the channel are slightly below the zero pressure graident curve established by the Stanford boundary layer experiments. This is to be expected because the channel is a negative pressure gradient flow and Schraub (28) has shown that the effect of a negative pressure gradient is to reduce the bursting rate. The bursting rates measured in this channel are shown normalized by the zero pressure gradient values and plotted versus the pressure gradient parameter K in Figure 23, where for a channel flow (see Halleen (19))

$$K = \frac{4\nu}{\rho D_H} \frac{\tau_w}{U^3_{max}}$$

The solid line is the best fit curve for bursting rates in pressure gradients measured by Schraub and this data is in good agreement with his results.

The streak spacings for the three flow rates are shown in Figure 24. The average streak spacing of $\lambda^+ = 96$ compares very well with a

$\lambda^+ = 98 \pm 15$ measured by Halleen. The wall shear velocity values used in Figures 22, 23, and 24 where computed from Figure 17c.

A summary of the qualifying data can be found in Table III. The laser velocimeter and flow visualization data have shown that we have a two-dimensional fully developed turbulent channel flow with low speed bursting rates and streak spacings comparable, within the limits of the experimental uncertainties, to the data of previous investigators.

Friction-Reduction Measurements

It was difficult to measure the velocity gradient at the wall and hence the wall shear in the polymer solution because the data acquisition system used with the laser velocimeter was slow and because the polymer degraded with use. This degradation is believed to be caused by entrained air in the weir cascade oxidizing the polymer and breaking the long chain structure. Due to the low wall shear velocities used in these flow visualization studies, the polymers must be used in their undegraded form which limits the data collection time to one or two runs of the channel for a given polymer solution. Consequently one wall shear measurement in the channel was used to verify a correlation from which other channel wall shears could be deduced. To establish and then to deduce the amount of friction reduction that was achieved with the dilute polymer solution, it was necessary to provide two flow paths in parallel with the channel (the pressure drop in the 2.92 inch hydraulic diameter channel is too small to be measured accurately). Two stainless steel tubes (0.425 diameter and 0.835 inch diameter), each approximately nine feet long, were used to measure the pressure

SUMMARY OF RESULTS

Description	Mass Avr. Velocity (ft/sec)	LAMIR U_τ (ft/sec) Wall Slope	LAMIR U_τ (ft/sec) Cross-Plot	Visual $F(\frac{\text{burst}}{\text{in/sec}})$	Visual λ (in)	Visual $\overline{T}_B = \frac{1}{F\lambda}(\frac{\text{sec}}{\text{burst}})$
2-D bellmouth entrance, water	0.23	0.014 ± 8%	0.019	0.19 ± 16%	0.77 ± 20%	6.8 ± 25%
	0.43	0.024 ± 8%		0.71 ± 10%	0.50 ± 8%	3.2 ± 13%
	0.69	0.034 ± 8%	0.043	2.72 ± 7%	0.30 ± 7%	1.2 ± 10%
2-D bellmouth entrance, polymer Run #1, C=139 wppm	0.23	a		relaminarizing		
	0.43	0.021		0.36 ± 16%	0.91 ± 23%	3.0 ± 28%
	0.69	0.030 ± 14%		0.33 ± 12%	0.67 ± 11%	4.5 ± 16%
2-D bellmouth entrance, polymer Run #2, C=139 wppm	0.23	a		relaminarizing		b
	0.43	0.021		0.44 ± 9%		2.5 ± 23%
	0.69	0.030		0.86 ± 12%		1.7 ± 16%
Square entrance, water	0.43	0.024	c	1.31		
	0.69	0.034		4.15		
	0.87	0.042		9.46		
Square entrance, polymer Run #2, C=100 wppm	0.43			0.96		
	0.69			1.51		
	0.87			1.69		

a = Values of wall shear velocity are extrapolated from Figure 17c and $\%_{FR}$ vs. U_{τ_S}.

b = Values of λ are assumed to be the same as in Experiment 8.

c = Values of wall shear velocity are extrapolated from Figure 17c.

drop of both water and dilute polymer solutions flowing at various flow rates. Two tubes are used in order to determine the effect of tube diameter upon the amount of drag reduction. The pressure drop was measured with an inverted U-tube manometer and the flow rate was measured with an F & P precision bore rotameter.

The per cent friction-reduction in the tubes is calculated by measuring the pressure drop at a given flow rate both with and without the drag-reducing polymers in solution.

$$\%_{FR} = \frac{\Delta P_S - \Delta P_{DPS}}{\Delta P_S}$$

Whitsitt, et al. (53) have found that per cent drag-reduction is a unique function of the solvent wall shear velocity. This unique relationship was found to hold over flow-section diameters ranging from 0.18 inches to 6.0 inches. Our results shown in Figure 25 for the two tubes also demonstrate that the per cent friction-reduction is a unique function of the solvent wall shear velocity. The per cent friction reduction measured with the laser velocimeter in the channel at the highest visualized wall shear velocity is also plotted in Figure 25. The per cent friction reduction in the channel was calculated from the change in the wall shear based on the velocity gradient at the wall. This calculation was based upon the assumption that the dilute polymer solution is effectively Newtonian (see Appendix D) and upon a measurement of the viscosity of the dilute polymer solution.

$$\%_{FR} = \frac{\Delta P_S - \Delta P_{DPS}}{\Delta P_S} = \frac{\tau_{\omega_S} - \tau_{\omega_{DPS}}}{\tau_{\omega_S}} \quad .$$

The per cent friction reduction measured in the channel correlated well with the value predicted from the pipe data.

The wall shear in the dilute polymer channel flow and the amount of friction reduction in the channel was then calculated in the following manner. First the mass flow rate (i.e., U_{avg}) and the solution temperature were measured. Then using the solvent viscosity the Reynolds number was calculated and the solvent wall-shear velocity (and hence wall shear) was obtained from Figure 17c. Finally the per cent friction reduction and the wall-shear velocity in the dilute polymer solution was determined from the friction-reduction correlation established for the solution being used.

A friction-reduction correlation was established for each solution. Pressure-drop data was taken in the pipes before the first run and after the second run during which the primary visual data was acquired (see Figure 31). This check for degradation was performed for all data taken in drag-reducing solutions.

Bursting Rates and Streak Spacings in a Drag-Reducing Solution

Bursting and streak spacing films were taken at the same flow conditions as the channel qualifying data but with the addition of 139 wppm of polyethylene oxide. Still photographs of the 16mm films are shown in Figures 26 and 27. Since bursting rates are a time domain phenomena, still photographs are unable to show the drastic changes that are taking place in the bursting process. A 16mm color film is being prepared and will be submitted to the Engineering Societies Library, 345 East 47th Street, New York, New York 10017.

The non-dimensional streak spacing in the polymer solution is increased from $\lambda^+ = 96$ to $\lambda^+ = 170$ (see Figure 28). This trend is

in accord with the recent observations of Hanratty (20). Figure 29 shows the bursting rates in the polymer solution compared with the water data. All polymer solution data is plotted using reduced wall-shear velocities predicted from Figures 17c and 31.

A comparison of bursting frequencies per second per inch of dye slot is not totally revealing because λ^+ changes. Hence the data was replotted as the average time between bursts $\overline{T}_B$. $\overline{T}_B$ is related to F (bursts/sec-in.) and λ (in) by $\overline{T}_B = 1/F\lambda$ and is shown plotted versus the wall-shear velocity in Figure 30. In general, the time between bursts seems to be adjusting to the production levels associated with the reduced wall shear values (and therefore reduced dissipation rates).

There is one data point which obviously does not adjust to the reduced production level. This point needs to be discussed further. Films were made at the same flow rates for two consecutive passes of the polymer solution through the channel. The bursting rate at the highest wall shear velocity during the first pass is the point which stands out from the rest of the data. The 95% confidence interval for this one data point may not be sufficiently large in the time scale. Due to an abnormally long quiescent period observed in the motion pictures of this flow condition, the observation time period may not have been sufficient to provide an adequate statistical sample of the bursting rate. However, other drag reduction studies have noted abnormally high drag reduction values in freshly prepared solutions. Ellis (7) has suggested that a fresh solution may actually have "super" molecules caused by molecular entanglements. This effect could be responsible for the abnormally long $\overline{T}_B$ data point even though the

pressure drop measurements did not indicate any superior drag reduction. The higher shear levels present in the pipes may not have allowed these entanglements to persist into the measurement sections which are appreciably downstream of the pipe's entrances.

All of the results that have been described so far were obtained in the channel with a two dimensional bellmouth entrance. Some previous visual data was obtained in the channel with a sharp edged, square entrance. Subsequently, LAMIR data indicated that the velocity profile was skewed and the entrance conditions were modified to the bellmouth configuration.

The per cent bursting reduction, $\%_{BR} = (F_S - F_{DPS})/F_S$, at a fixed mass flow rate for both the primary visual data (bellmouth entrance) and the previous visual data are shown plotted in Figure 31. There is a reasonable agreement between the bursting rate experiments. This again points out the fact that friction reduction is a wall phenomena and large changes in the outer flow have little effect on what is happening at the wall. Notice also that both $\%_{FR}$ and $\%_{BR}$ extrapolate to zero at about the same value of critical wall shear velocity.

No pictures, bursting rates or streak spacings are shown for the lowest flow rate of polymer solution because the motion picture films indicate that the flow is in the later stages of transition. This test was unique in this respect because in all other cases the flow was definitely turbulent. The motion pictures of the dilute polymer solution at Re = 6000, however, showed the random appearance of turbulent spots spreading spanwise across regions of laminar flow marked by the dye slot. These were not turbulent slugs that filled the

channel as occurs in pipe flow transition. These spots were similar to the turbulent spots observed by Meyer and Kline (39) occurring in the later stages of boundary layer transition. An increased entry length for the transition to turbulent flow has also been noted for drag-reducing solutions in pipe flow by Giles and Petit (12), and this appears to be what is observed here.

The results of the visual studies both with and without polymer are shown in Table III.

CHAPTER IV

DISCUSSION

As pointed out in Chapter I, there has been considerable effort devoted to finding the proper nondimensional grouping that can characterize the drag-reduction phenomena. Also, there has been considerable speculation as to the molecule-fluid interactions or mechanisms of achieving drag reduction. In this chapter some of these more noteworthy theories as well as previous experimental evidence are discussed within the new perspective of this investigation. Also, a discussion of the technique for using the LAMIR data to provide estimates of the statistical moments and the energy density function of a highly fluctuating turbulent flow field is given.

Nondimensional Groupings Used to Characterize Drag Reduction

Several nondimensional groups have been postulated to characterize drag reduction. The most notable ones are the time-scale group (Deborah number), the length-scale group (proposed by Virk), and the energy-scale group (proposed by Walsh). The degree to which these groups successfully predict the onset of drag reduction is usually considered the test of their ability to characterize the phenomena.

Both the bursting-reduction and drag-reduction data of this study indicated that onset occurred at a wall shear velocity of U_τ = 0.015 ft/sec. This onset wall-shear velocity can be coupled with the molecular properties of the PEO solution (see Appendix D) to yield experimental values for the nondimensional groups at onset which can then be compared to their hypothesized onset values. The various hypothesized and calculated onset ratios are shown in Table IV.

TABLE IV

COMPARISON OF DRAG REDUCTION ONSET PARAMETERS

Reference	Nondimensional Grouping	Hypothesized Values	Experimental Value
Virk (45)	$2 \cdot z \cdot U_\tau / \nu$	0.015	0.003
Deborah # (21), (49)	$0.42 \cdot \frac{M[\eta]\eta_s}{RT} \cdot U_\tau^2 / \nu$	$\approx$ 1.0	0.134
Walsh (56)	$8 \cdot C[\eta] \cdot \frac{M[\eta]\eta_s}{RT} \cdot U_\tau^2 / \nu$	0.01	0.05

As can be seen, there is a poor correlation between the measured and the hypothesized onset values of the groups. It should be noted, however, that in this study the Deborah number was approaching 1.0 as the per cent friction reduction was approaching its maximum value (i.e., the time scale of the molecule is of the same order as the

strain rate in the sublayer). Thus, of the groups considered in Table IV, the Deborah number seems to be the best predictor for the presence of friction reduction.

Black (1) has proposed yet another nondimensional group which he relates to a mechanism for friction reduction. He proposed that the polymers act to stabilize the sublayer breakdown process (i.e., stabilize the bursting process) such that the nondimensional time between bursts should be increased from $U_\tau^2 \overline{T}_B/\nu = 116$ for a normal Newtonian flow to $U_\tau^2 \overline{T}_B/\nu \approx 1400$ for a maximum-drag-reducing flow. On this point, our data is inconclusive. Most of the data indicates that the nondimension time between bursts is essentially constant ($97 \leq U_\tau^2 \overline{T}_B/\nu \leq 137$). However, for the one data point $U_\tau^2 \overline{T}_B/\nu = 350$. Moreover, since our visual data was taken at friction reductions well below the maximum-friction-reduction asymptote our data does not provide a critical test of Black's hypothesis. Future studies at higher wall shear velocity should be done to critically test Black's hypothesis.

Black's analysis does indicate that any stabilization of the Einstein and Li (6) model of the viscous sublayer would lead to an overall thickening of the sublayer and a decrease in the average wall shear. Einstein and Li modeled the sublayer as a temporally growing, viscously dominated region near the wall that periodically becomes unstable, breaks down and begins growing again. Their model, and consequently Black's analysis, does not consider the three dimensionality of the sublayer (i.e., the spanwise velocity variations illustrated by the streaky structure). Since the visual data show that variations in the spanwise velocity distribution are an important characteristic

of drag reduction it must be considered in any proposed explanation of drag reduction. Consequently an Einstein and Li model cannot represent all of the features of drag reduction.

Discussion of Drag-Reduction Mechanisms

This investigation along with others is beginning to throw light on what the polymers are doing to the viscous sublayer. How the polymers are altering the wall layer is still open to speculation. First let us see what the polymers are doing to the sublayer.

The bursting reduction observed in this study is different from the previous studies of bursting suppression by body forces. Coriolis forces and accelerations eventually lead to relaminarization. Pruit and Crawford (59) have pointed out that drag-reducing solutions never appear to relaminarize. Many investigators have found that the maximum decrease in the turbulent drag is approximately 80 per cent.

Figure 32 shows per cent bursting reduction at a given mass flow rate plotted versus per cent turbulent drag reduction.

$$\%_{TR} = \frac{f_T - f_{DPS}}{f_T - f_L}$$

One hundred per cent $\%_{TR}$ occurs when there is no bursting and represents relaminarization. Even though there is considerable scatter of the data, it appears that 100 per cent bursting reduction will occur at approximately 40 to 50 per cent turbulent drag reduction. Since the flow is not relaminarizing it is very unlikely that this extrapolation is accurate. It is more likely that the curve bends and asymptotically approaches a value of $\%_{TR}$ less than 100%. Future studies should measure λ and $\overline{T}_B$ for wall shear velocities up to the maximum-drag-

reduction values (e.g., 0.1 ft/sec) to determine the nature of the structure as one approaches maximum drag reduction.

All of the body force stabilization studies have observed that the nondimensional streak spacing λ^+ has essentially remained constant. As they applied stronger and stronger stabilizing body forces they in effect observed $\overline{T}_B$ go to infinity (relaminarization).

In this study, even though $\overline{T}_B$ may be increased, λ^+ is increased from $\lambda^+ \approx 100$ to $\lambda^+ \approx 170$. This trend has also been noted by Hanratty (20). He found λ^+ increasing as a function of the per cent friction reduction. It should be noted that even if $\overline{T}_B$ were to remain constant, the effect of increasing the streak spacing would decrease the spatially averaged bursting rate which would lead to lower production levels and lower wall shears.

The laser velocimeter data of Rudd (48) has shown that a drag-reducing solution maintains the linear velocity profile (i.e., $U^+ = Y^+$) in the sublayer and extends it further away from the wall (e.g., to about $Y^+ = 20$). His data also shows that the normalized streamwise turbulent intensity (u'/U_τ) maintains its characteristic linear profile throughout the thickened sublayer. The one mean velocity and turbulent intensity point measured with the LAMIR in the dilute polymer solution in this study supports the observations of Rudd. These results are interesting but they do not tell much about the mechanisms of drag reduction. The mean velocity result could have been deduced from gross flow considerations. For example, for a given constant flow rate in a pipe or a channel, a drag-reducing solution decreases the velocity gradient at the wall leaving the main portion of the turbulent velocity profile unchanged (e.g., as observed by (47), (54), and (57)). Since

the largest velocity gradient in a turbulent channel or pipe flow is at the wall (approximately half of the maximum centerline velocity is reached at the edge of the sublayer) the decreased velocity gradient demands that the linear type (steepest gradient) behavior of the sublayer be extended further away from the wall in order to maintain the same nondrag reduced mean flow condition.

Rudd's observation that w'/U_T is decreased in the near wall region is more interesting and confirms the visual observations of this study. Namely, our motion picture data qualitatively indicate that the spanwise velocity gradients and the spanwise fluctuation intensities are much less in the drag-reducing solution than they are in a equivalent wall shear Newtonian flow. This observation is based on the fact that the dye appears to be much more uniformly distributed in the spanwise direction (i.e., the dye shows much less tendency to collect into streaks) and the streaks that do form have much less tendency to oscillate in the spanwise direction.

Having discussed what the polymers are doing to the sublayer, let us talk about how the polymers may be affecting it. Virk (52) has proposed a phenomenological explanation for drag reduction based on an "elastic sublayer" model. This explanation and many others that are based on interpreting changes in the "law of the wall" do not seem to hold promise in giving much further insight into the drag-reduction phenomena. This conclusion is based upon several facts. First the "law of the wall" does not contain any information about the physical structure of the sublayer. In fact, based upon the $U^+ = Y^+$ velocity profile, early investigators reasoned that the sublayer was laminar. This is clearly incorrect and demonstrates the danger of inferring

"details" from an average. Since drag reduction occurs with and apparently because of changes in the structure of the sublayer, it seems almost certain that a thoroughly adequate explanation of the drag-reduction phenomena must be based upon an understanding of these changes in the sublayer structure.

Mollo-Christensen (41) and Kline, et al. (28), have summarized much of the current information about the physical structure of turbulent wall flows and discuss some of the possible mechanisms of the wall-layer streak breakup as it occurs in non-friction-reducing flows. They suggest that spanwise vortex stretching may lead to intermittent and random formation of intense local shear layers. The stretching and compressing of spanwise vortex elements in the region very near the wall would lead to locally high and low speed zones in the spanwise direction. It is in these low speed zones that the dye collects and intense local shear layers form. The intense shear layers give rise to inflectional profiles that become unstable and burst away from the wall (e.g., as visualized by Kim (25)). These bursts then generate large Reynolds stresses and produce more turbulence energy. The cycle is completed by continuity considerations that provide large scale downwashes that stretch the vortices and so on.

The visual data obtained in this study show that while all of the experimentally observed features of the structure are present the spanwise velocity gradients are greatly decreased in the dilute polymer solution. Drag-reducing polymers exhibit much larger resistance to axisymmetric strains than they do to rotational strains (Peterlin (49)) and consequently it is reasonable to assume that they may be resisting spanwise vortex stretching in the wall region. When low speed

instability regions do form at much larger λ^+ values, the polymer's filament forming tendencies (Gordon (17)) may resist breaking and therefore further suppress bursting. In any case the observed decreased bursting rates lead to a decreased production level that produces a decreased average wall shear.

Not only would the resistance of the polymer to spanwise stretching and filament breaking reduce the average spatial bursting rate (F) but it decreases the spanwise shear ($\partial\bar{U}/\partial Z$). The films made in this study qualitatively indicate that the spanwise velocity gradient and also the spanwise and normal turbulent intensities (w' and v') in the wall region are greatly reduced. The high frequency suppression at the wall noted by Fortuna (9) (measuring concentration fluctuations) and Kadykov (24) (measuring pressure fluctuations) may be linked to a suppression of v'/U_τ. Actual v' data has not been reported to date; however, Rudd's data confirms that w' is reduced.

Laser Velocimetry

Signal "drop out" problems and low signal to noise ratios present in "continuous wave" laser anemometer systems led to the development of a system that will measure the statistical turbulent properties in fluid flows by utilizing the "Doppler" frequency of single particles passing through the crossed beam probe volume of a scatter-scatter laser velocimeter. The unusual character of this data warrents some discussion as to how it might be utilized in studying the statistical properties of a turbulent flow field.

The system outlined utilizes a simple technique to accurately measure the frequency of a single burst (thereby obtaining an accurate

individual realization of velocity at a point in space). By repeated sampling, the probability density function of the velocity fluctuations is constructed. This function then gives unambiguously and to a given probable accuracy the mean velocity, rms fluctuation level and energy density function at a point in space. The system does not require expensive A-D conversion devices and is not troubled by sampling rate (and quantization) associated with these devices.

Uzkan and Reynolds (51) have pointed out the advantages of using the probability density function in the study of turbulent flow fields. They point out that spectra and space correlations provide primarily information about eddy size, and a rough idea about the relative energy of different sized eddies. The probability density function p(u), however, contains primarily information about the magnitude of the velocity fluctuations.

Figure 15 shows a typical velocity distribution about a local mean velocity. The probability of finding a velocity fluctuation between u and u + du (where u is defined as the instantaneous velocity fluctuation in the X_1 direction, $u = U - \overline{U}$) is defined as the probability density function p(u)du. It may be estimated directly from the individual velocity realizations available with our laser velocimeter by computing the occurrence frequency of velocities in particular finite velocity bands. All of the statistical information about the turbulence at a point is contained in the probability distribution function. The turbulent intensity, u', can be calculated from the probability density function by

$$\overline{u^2} = \int_{-\infty}^{\infty} u^2 p(u)\, du \ .$$

Similarly, the skewness and the flatness factors may be calculated from

$$\overline{u^3} = \int_{-\infty}^{\infty} u^3 p(u)du$$

and

$$\overline{u^4} = \int_{-\infty}^{\infty} u^4 p(u)du \ .$$

The energy density function is defined as

$$\mathcal{E}(u) = u^2 p(u)$$

and represents the contribution of each velocity fluctuation to the energy of the turbulence. Figure 33 shows a typical plot of the energy density function superimposed on the probability density function. The absolute value of the peaks in this function are analogous to the size of the energy containing eddies used in the more familiar energy spectra representation. The energy density function peaks represent the magnitude of the instantaneous velocity fluctuation which contributes the most turbulence energy. Uzkan has made some preliminary measurements of this function in both a decaying grid generated turbulence field and in a turbulent boundary layer. Uzkan's data indicate that changes in the turbulent energy distribution does not affect the energy density function below the maximum energy containing peaks but changes the location of the peaks. This indicates that the dominanet change in the energy contribution occurs for large amplitude fluctuations. Unfortunately, due to a lack of the proper electronic equipment, sufficient data is not available in this present study to accurately describe the energy density function in our flow situation. Work is currently underway, however, that will provide this information.

CHAPTER V

SUMMARY AND CONCLUSIONS

Summary

The objectives of this study were to determine if the addition of drag-reducing macromolecules 1) modifies the production of turbulent kinetic energy and 2) alters the structure of the viscous sublayer. This was accomplished by visualizing the near wall region of a fully developed two-dimensional channel flow.

Considerable data was taken with a laser anemometer to ensure that the mean velocity profile and the streamwise intensity profile of the water flow compared favorably with the two-dimensional channel profiles measured by previous investigators. It was also carefully established through the use of a friction-reduction correlation and laser velocimeter wall-shear measurements that the 139 wppm solution of polyethylene oxide gave drag reduction in the channel.

Motion pictures showed that the presence of the macromolecules in the near wall region significantly altered the structure of the sublayer. Comparisons between the sublayer structure of drag-reducing solutions and non-drag-reducing solutions are summarized below.

Constant Flow Rate Comparison

A visual comparison of the viscous sublayers at an equal mass flow rate of water and a 26 per cent drag-reducing solution has shown

a considerable alteration in the sublayer's three-dimensional structure. The spacing of the longitudinal low speed streaks is approximately twice as large as the equivalent spacing in water. There is also a significant (50% to 80%) decrease in the ejection rate of the streak's low momentum fluid away from the wall (also the intensity of the ejection is decreased). At the lowest flow rate studied (corresponding to a solvent Re = 6000) the normally fully developed turbulent flow was stabilized such that 44 channel widths downstream of the entrance the wall layers were in the later stages of laminar to turbulent transition.

Constant Wall Shear Comparison

By having an estimate of the reduced wall shear velocities, one can make comparisons between the drag-reducing solution's structure and the established structure of water at the reduced wall-shear velocity. On this basis the average time between bursts of an individual streak does not seem to be altered by the drag-reducing solution. However, for the high Reynolds number experiment and for a very freshly mixed dilute polymer solution the time between the bursts of an individual streak was seen to increase. Due to a relatively large uncertainty in the visual data and the wall shear estimate for this data point, the result is not conclusive. Further measurements must be made using longer spatial and temporal averaging periods coupled with insitu measurements of wall shear in order to clarify the bursting rate trends.

The spacing of the low speed streaks is still about 70 per cent greater than in a non-drag-reducing fluid. Also, from the motion pictures it appears that the spanwise velocity gradient $\partial \overline{U}/\partial Z$ and

the turbulent intensities (v' and w') are decreased in the drag-reducing solution. (This observation is based on a reduced wall shear comparison and is even more noticeable in a constant mass flow rate comparison.) The increased streak spacing leads to a decreased spatially averaged bursting rate even if the time between bursts is unchanged.

Conclusions

The conclusions of this study may be stated as follows:

1. The reduced spatially averaged ejection rate of low momentum fluid away from the wall implies a reduced production of turbulent kinetic energy which demands a reduction in the dissipation of turbulent kinetic energy. This is manifested as a decrease in the wall shear.
2. Since the drag reduction occurs with and apparently because of changes in the structure of the sublayer, future studies of the drag-reduction mechanisms should be concentrated on gaining further insights into the structural changes occurring in the viscous sublayer. As pointed out in the last chapter, it is dangerous to infer details of turbulent structure from "mean" measurements.
3. Further studies of the structural changes produced by a drag-reducing macromolecule in the sublayer should be made at or near the maximum-drag-reduction asymptote to provide a critical test of Black's hypothesis and to observe the maximum affect.
4. Of the hypothesized nondimensional groups considered in this study, the Deborah number appears to best indicate the

presence of drag reduction.

5. It is now evident that the most meaningful comparisons of sublayer structure change should be based on wall-shear velocity. This study used an experimental design that provided a direct visual comparison of flows with equal mass flow rates. Future studies should concentrate on direct visual comparisons based upon equal values of the wall-shear velocity. It would also be of great interest to simultaneously measure the instantaneous wall shear stress directly while the visual data is recorded for both the water and the dilute polymer solutions.

6. The laser anemometer measuring individual realizations is able to accurately and unambiguously measure the statistical properties of highly fluctuating turbulent flow fields and it circumvents the problems of random phase fluctuation and signal "drop out" present in continuous wave laser anemometer systems.

BIBLIOGRAPHY

(1) Black, T. J. "Viscous Drag Reduction Examined in the Light of a New Model of Wall Turbulence." Viscous Drag Reduction, Wells, ed. New York: Plenum Press, 1969.

(2) Brayton, D. B., and W. H. Goethert. "A New Dual-Scatter Laser Doppler Shift Velocity Measuring Technique." ISA Transactions, Vol. 10, n1, p. 40, 1971.

(3) Clark, J. A. "A Study of Incompressible Turbulent Boundary Layers in Channel Flow." Trans. ASME, J. Basic Eng., December 1968, pp. 455-468.

(4) Comte-Bellot, Genevieve. "Coefficients de dissymétric et d'aplatissement, spectres et corrélations en turbulence de conduite." Journal de Mecanique, Vol. 11, n2, 1963.

(5) Corino, E. R., and R. S. Brodkey. "A Visual Investigation of the Wall Region in Turbulent Flow." J. of Fluid Mechanics, Vol. 37, 1969.

(6) Einstein, H. A., and H. Li. "The Viscous Sublayer Along a Smooth Boundary." A.S.C.E.J. of Engineering Mechanics, 1956, p. 945.

(7) Ellis, H. D. "Effects of Shear Treatment on Drag-Reducing Polymer Solutions and Fibre Suspensions." Nature, Vol. 226, April 1970, p. 352.

(8) Fabula, A. G. "An Experimental Study of Grid Turbulence in Dilute High Polymer Solutions." (Unpub. Ph.D. Thesis, Pennsylvania State University, 1966).

(9) Fortuna, G., and T. J. Hanratty. "Use of Electrochemical Techniques to Study the Effect of Drag-Reducing Polymers on Flow in the Viscous Sublayer." Symposium Series, Drag Reduction, Vol. 67, n111, 1971.

(10) Friehe, Carl Alan. "Velocity Measurements in Dilute Polymer Solutions." (Unpub. Ph.D. Thesis, Stanford University, 1968).

(11) Gadd, G. E. "Turbulence Damping and Drag Reduction Produced by Certain Additives in Water." Nature, 206, 1965, p. 463.

(12) Giles, W. B., and W. T. Pettit. "Stability of Dilute Viscoelastic Flows." Nature, 216, 1967, p. 470.

(13) Goethert, W. H. "Frequency Broadening in Reference Beam Laser Doppler Velocimeter Data." AEDC-TR-71-163, September 1971.

(14) Goldstein, R. J., R. J. Adrian, and D. K. Kreid. "Turbulent and Transition Pipe Flow of Dilute Aqueous Polymer Solutions." I & EC Fundamentals, Vol. 8, n. 3, 1969, p. 498.

(15) Goldstein, R. J., and W. F. Hagen. "Turbulent Flow Measurements Using a Laser-Doppler Velocimeter." Physics of Fluids, 10, 1967, 1349-1352.

(16) Goldstein, R. J., and D. K. Kreid. "Measurement of Laminar Flow Development in a Square Duct Using a Laser-Doppler Flowmeter." J. of Applied Mechanics, 1967, p. 813.

(17) Gordon, R. J. "Mechanism for Turbulent Drag Reduction in Dilute Polymer Solutions." Nature, Vol. 227, August 1970, p. 599.

(18) Greated, C. "Statistical Ambiguity in Laser Anemometry." Disa Information Bulletin, No. 12, November 1971.

(19) Halleen, R. M., and J. P. Johnston. "The Influence of Rotation on Flow in a Long Rectangular Channel - An Experimental Study." Report MD-18, Thermosciences Div., Dept. of Mech. Engr., Stanford University, 1967.

(20) Hanratty, T. J. "Use of Electromechanical Techniques to Study the Influence of Drag Reducing Polymers on Turbulence Close to a Wall." Presented at Symposium on Turbulence in Liquids, University of Missouri at Rolla, 1971.

(21) Hershey, H. C., and J. L. Zakin. "A Molecular Approach to Predicting the Onset of Drag Reduction in the Turbulent Flow of Dilute Polymer Solution." Chemical Engineering Science, 22, p. 1847, 1967.

(22) Hjelmfelt, A. T., Jr., and L. F. Mockros. "Motion of Discrete Particles in a Turbulent Fluid." Appl. Sci. Res., v 16, pp. 149-161, 1965.

(23) Hoyt, J. W. "The Effects of Additives on Fluid Friction." Freeman Review, presented at the ASME Winter Annual Meeting, Washington, D.C., 1971.

(24) Kadykov, I. F., and L. M. Lyamshev. "Influence of Polymer Additives on the Pressure Fluctuations in a Boundary Layer." Soviet Physics-Acoustics, v. 16, n. 1, p. 59, 1970.

(25) Kim, H. T., S. J. Kline, and W. C. Reynolds. "An Experimental Study of Turbulence Production Near a Smooth Wall in the Turbulent Boundary Layer with Zero Pressure Gradient." MD-20, Thermosciences Div., Dept. of Mech. Engr., Stanford University, 1968.

(26) Klebanoff, P. S. "Characteristics of Turbulence in a Boundary Layer with Zero Pressure Gradient." NACA-TN-3178, 1954, also TN-1247, 1956.

(27) Kline, S. J., and F. A. McClintock. "Uncertainties in Single-Sample Experiments." Mechanical Engineering, January 1953.

(28) Kline, S. J., W. C. Reynolds, F. A. Schraub, and P. W. Runstadler. "The Structure of Turbulent Boundary Layers." J. of Fluid Mechanics, v. 30, p. 741, 1967.

(29) Kline, S. J., P. W. Runstadler, and W. C. Reynolds. "An Experimental Investigation of the Flow Structure of the Turbulent Boundary Layer." Report MD-8, Thermosciences Div., Dept. of Mech. Engineering, Stanford University, 1963.

(30) Kline, S. J., and F. A. Schraub. "A Study of the Turbulent Boundary Layer With and Without Longitudinal Pressure Gradients." Report MD-12, Thermosciences Div., Dept. of Mech. Engr., Stanford University, 1965.

(31) Laufer, J. "Investigation of Turbulent Flow in a Two-Dimensional Channel." NACA Report No. 1053, 1951.

(32) Laufer, J. "The Structure of Fully Developed Pipe Flow." NACA Report 1174 or TN 2945, 1953.

(33) Lennert, A. E., D. B. Brayton, et al. "Summary Report of the Development of a Laser Velocimeter to be Used in AEDC Wind Tunnels." AEDC-TR-70-101, July 1970.

(34) Lezius, D. K., and J. P. Johnston. "The Structure and Stability of Turbulent Wall Layers in Rotating Channel Flow." Report MD-29, Thermosciences Div., Dept. of Mech. Engr., Stanford University, August, 1971.

(35) Lumley, J. L. "Drag Reduction by Additives." Annual Review of Fluid Mechanics, v. 1, 1969.

(36) Lumley, J. L., W. K. George, and Y. Kobashi. "The Influence of Ambiguity and Noise on the Measurement of Turbulent Spectra by Doppler Scattering." Turbulence Measurements in Liquids, University of Missouri at Rolla, 1969.

(37) Maxumder, M. K., and D. L. Wankum. "SNR and Spectral Broadening in Turbulence Structure Measurements Using a CW Laser." Applied Optics, Vol. 9, n. 3, March 1970.

(38) Merrill, E. W., K. A. Smith, H. Shin, and H. S. Mickley. "Study of Turbulent Flows of Dilute Polymer Solutions in a Couette Viscometer." Trans. of the Soc. of Rheology, v. 10, n. 1, p. 335, 1966.

(39) Meyer, K. A., and S. J. Kline. "A Visual Study of the Flow Model in the Later Stages of Laminar-Turbulent Transition on a Flat Plate." Report MD-7, Thermosciences Div., Mech. Engr. Dept., Stanford University, 1961.

(40) Middleman, S. The Flow of High Polymers. John Wiley & Sons, 1968.

(41) Mollo-Christensen, E. "Physics of Turbulent Flow." AIAA Journal, v. 9, n. 7, p. 1217, 1971.

(42) Moretti, P. M., and W. M. Kays. "Heat Transfer Through an Incompressible Turbulent Boundary Layer with Varying Free-Stream Velocity and Varying Surface Temperature." Stanford University, Report No. PG-1, 1964.

(43) Narahari Rao, K., R. Narasimha, and M. A. Badri Narayana. "The 'Bursting' Phenomenon in a Turbulent Boundary Layer." J. of Fluid Mechanics, v. 48, p. 339, 1971.

(44) Peterlin, A. "Molecular Model of Drag Reduction by Polymer Solutes." Nature, v. 227, p. 598, August, 1970.

(45) Rouse, P. E., Jr. "A Theory of the Linear Viscoelastic Properties of Dilute Solutions of Coiling Polymers." Journal of Chem. Phys., 21, p. 1272, 1953.

(46) Rudd, J. M. "A New Theoretical Model for the Laser Doppler Meter." J. of Scientific Inst. (J. of Physics E), Series 2, 2, 55-58, 1969.

(47) Rudd, M. J. "Measurements Made on a Drag Reducing Solution with a Laser Velocimeter." Nature, v. 224, p. 587, November, 1969.

(48) Rudd, M. J. "Laser Dopplermeter and Polymer Drag Reduction." Drag Reduction, Chem. Eng. Progress Symposium Series, Vol. 67, 1971.

(49) Seyer, F. A., and A. B. Metzner. "Turbulent Flow Properties of Viscoelastic Fluids." The Canadian Journal of Chemical Engineering, 45, p. 121, 1967.

(50) Toms, B. A. "Some Observations on the Flow of Linear Polymer Solutions Through Straight Tubes at Large Reynolds Numbers." Proc. 1st Int. Congress Rheol., Holland II, p. 131, 1948.

(51) Uzkan, T., and W. C. Reynolds. "A Turbulent Boundary Layer on a Wall Moving at the Free-Stream Velocity." Thermosciences Div., Dept. of Mech. Engr., Stanford University, Report No. MD-14, August 15, 1965.

(52) Virk, P. S. "An Elastic Sublayer Model for Drag Reduction by Dilute Solutions of Linear Macromolecules." J. of Fluid Mechanics, v. 45, part 3, pp. 417-440, 1971.

(53) Virk, P. S., and E. W. Merrill. "The Onset of Dilute Polymer Solution Phenomena." Viscous Drag Reduction, ed., Wells, New York: Plenum Press, 1969.

(54) Virk, P. S., E. W. Merrill, H. S. Mickley, K. A. Smith, and E. L. Mollo-Christensen. "The Toms Phenomena: Turbulent Pipe Flow of Dilute Polymer Solutions." J. of Fluid Mechanics, 30, p. 205, 1967.

(55) Wallace, J. M., H. Eckelmann, and R. S. Brodkey. "The Wall Region in Turbulent Shear Flow." Submitted for publication in the J. of Fluid Mechanics, July, 1971.

(56) Walsh, M. "On the Turbulent Flow of Dilute Polymer Solutions." (Unpub. Ph.D. Thesis, California Institute of Technology, 1967).

(57) Wells, C. S., J. Harkness, and W. A. Meyer. "Turbulence Measurements in Pipe Flow of a Drag-Reducing Non-Newtonian Fluid." AIAA Journal, v. 6, n. 2, p. 250, February, 1968.

(58) Wells, C. S., and J. G. Spangler. "Injection of a Drag-Reducing Fluid into Turbulent Pipe Flow of a Newtonian Fluid." The Physics of Fluids, 10, n. 9, p. 1890, 1967.

(59) Whitsitt, N. F., L. J. Harrington, and H. R. Crawford. "Effect of Wall Shear Stress on Drag Reduction of Viscoelastic Solutions." Viscous Drag Reduction, ed., Wells. New York: Plenum Press, 1969.

(60) Yeh, Y., and H. Z. Cummins. "Localized Fluid Flow Measurements with a He-Ne Laser Spectrometer." Apply. Phys. Letters, 4, 176-178, 1964.

(61) Zimm, B. H. "Dynamics of Polymer Molecules in Dilute Solution: Viscoelasticity, Flow Birefringence and Dielectric Loss." Journal of Chem. Phys., 24, p. 269, 1956.

APPENDIX A

LASER PROBE VOLUME GEOMETRY

Brayton and Goethert (2) have made extensive calculations and measurements to determine the probe volume size as a function of the optical geometry (see Fig. 34). This figure shows two Gaussian light beams focused to diffraction limited spots at the same point in space. From this figure, one can derive what the particle velocity frequency should be from calculating the fringe spacing and also the major dimensions of the elipsoidal scattering volume. The intensity distribution of the Doppler signal across the elipsoidal scattering volume is Gaussian.

With a knowledge of the particle size distribution, one could decrease the effective scattering volume by approximately 50% if only the highest intensity signals were measured. This would be most desirable since in many instances the major diameter is aligned normal to the wall which is the direction one would like the probe dimension to be the smallest. The $1/e^2$ intensity contour of the scattering volume in our system is approximately 0.020 in. x 0.004 in.

Figure 35 shows the effect of the two laser beams crossing in water. Due to the changes in the index of refraction the beam intersection angle is less in the water (n = 1.33) than in the air (n = 1.00). The angle Φ is measured in air to be $\Phi = 8.89^{\circ}$. By using Snell's law across both the air-plexiglas and plexiglas-water interface

gives an intersection angle in water to be $\theta = 6.65^{\circ}$. This angular difference leads to a probe volume traversing scale factor. That is if the laser optics are traversed distance A in air, the probe volume moves distance B in the water. Figure 36 shows the geometrical scaling. The traversing scale factor is calculated to be

$$B = 1.34\ A.$$

A check of this scale factor provides a check on the value of the scattering angle and water index of refraction used in calculating the Doppler frequency-velocity proportionality constant.

An experiment was performed to measure this traversing scale factor and therefore determine the positioning accuracy and the velocity-Doppler frequency proportionality constant accuracy. Two plexiglas walls were positioned 1.250 ± 0.001 inches from each other. The area between the walls was filled with water. The laser crossed beam intersection point was considered to be at the surface of the plexiglas wall when only a single dot of light could be seen reflecting from the water-plexiglas interface. Then the beam intersection point was traversed through the water across to the other wall. The number of turns of the 16 threads to the inch traversing thread was measured. The predicted value of A was within 0.007 inch of the measured value of A indicating that the beam intersection angle in water calculated from Snell's law is essentially correct. Based on this angle the Doppler frequency for a velocity of one foot per second is

$$\nu_D = 2(1.33)\ \sin(6.65^{\circ})\ U/6328\ \text{Å}$$
$$= 149\ \text{khz/(ft/sec)}.$$

APPENDIX B

SCATTERING PARTICLE FREQUENCY RESPONSE

The size of the scattering particles is critical to the accuracy of the velocity measurement. All make-up water for the flow system is filtered through a 1.0 micron filter. However, a 100 ml sample was withdrawn from a location near the scattering volume while the channel was running to determine the size of the scattering particles. This 100 ml of water was then filtered through a 0.8 micron Millipore filter and the trapped particles were observed with a 10X Nikon microscope equipped with a Vickers image splitting eyepiece. The particles are predominantly small grains of sand. A random sampling of their diameters can be seen in the histogram of particle size, (Fig. 37). The sample is biased since large particles were examined in preference to many of the smaller particles. One can see that the average particle scattering light is approximately 25 microns in diameter. Obviously, however, some of the particles that velocity signals are observed from are around 100 microns in diameter.

A natural question now arises. Are the particles truly moving with the fluid? Hjelmfelt and Mockros (22), as well as many others, have studied the deviation of the particle motion from the fluid motion. They present frequency response curves for both amplitude ratio and phase angle with the ratio of particle to fluid density as a parameter. Since we are not currently interested in correlations, we

will not consider phase lag which places a more severe restriction on particle size than the amplitude ratio does.

Their results for a sand-water solution (density ratio 2.65) and an amplitude ratio of $U_p/U = 0.95$ give a Stokes number

$$N_s = \sqrt{\nu/\omega d_p^2} = 0.8 .$$

Solving for the frequency which could be followed by a 25 micron particle

$$f = \omega/2\pi = \nu/2\pi d_p^2 N_s^2 = 0.01/(6.28)(2.5 \times 10^{-3})(0.8)^2$$

$$= 400 \text{ hz} .$$

Similarly, a 100 micron particle would follow fluctuations below 25 hz. In any case, the scattering centers are capable of following essentially all of the turbulent fluctuations in water, where most of the fluctuations containing significant energy are estimated to be below 45 hz (estimated from water data taken by Uzkan and Reynolds (51)).

APPENDIX C

UNCERTAINTY ESTIMATES

The uncertainty estimates used in this study are made following the method outlined by Kline and McClintock (27). The major sources of error in this study are in the measurements of:

1. Average Channel Velocity
2. Local Mean Velocities from LAMIR
3. Turbulent Intensity from LAMIR
4. Wall Shear from LAMIR
5. Streak Spacing
6. Bursting Rates

Average Channel Velocity

A weir height versus volume flow rate calibration curve is shown in Figure 38. The uncertainties are estimated at 20:1 odds to be

$$\text{Volume} \pm 1\%$$

$$\text{Time} \pm 1\%$$

$$\text{Weir height} \pm 3\%$$

Therefore the proportionality constant is estimated to be

$$Q = K H^{1.72}$$

$$K \pm 5\%$$

The average flow rate can then be estimated from the weir height H and the calibration curve to be

$$Q \pm 7\% \ .$$

The average channel velocity is then estimated from Q and the channel cross sectional area A_c

$$A_c \pm 2\%$$

$$V = \frac{Q}{A_c} \pm 8\%$$

Local Mean Velocities from LAMIR

The accuracy of each individual velocity realization is estimated to be ± 2% at 20:1 odds. This is essentially the uncertainty of measuring the time required for eight periods of the Doppler frequency. The accuracy of the mean velocity at a point is estimated from the measured turbulent intensity and the number of individual realizations (20:1 odds) as

$$\left|\frac{\mu - \overline{U}}{\overline{U}}\right| = L \leq 1.96 \frac{\left(\frac{u'}{\overline{U}}\right)}{\sqrt{N}}$$

In all cases L was estimated to be less than 10%.

Turbulent Intensity from LAMIR

The 95% confidence interval on u' is estimated from

$$\frac{(N-1)\ u'}{N-1\chi^2\ 0.025} \leq \sigma^2 \leq \frac{(N-1)\ u'}{N-1\chi^2\ 0.975}$$

the per cent error between the estimated value of the turbulent intensity and the actual value is estimated to be ± 14% for 100 realizations.

Wall Shear from LAMIR

The wall shear is computed from

$$\tau_w = \eta \left.\frac{\Delta \bar{U}}{\Delta Y}\right|_{Y=0}$$

$$\eta \pm 10\%$$

$$\Delta U \pm 10\%$$

$$\Delta Y \pm 10\%$$

$$\therefore \tau_w \pm 17\%$$

and

$$U_\tau = \sqrt{\frac{\tau_w}{\rho}} \pm 8\%$$

Streak Spacing

The streak spacing error was estimated for each flow condition by averaging the number of streaks in a four inch span for eight randomly selected motion picture frames at each flow condition using a students t distribution. The estimated errors ranged from ± 7% to ± 23%.

Bursting Rates

The bursting rate error was computed from the bursting rate averages for each flow condition and assuming a student's t distribution. The estimated errors ranged from 7% to 16%.

APPENDIX D

POLYMER CHARACTERIZATION

One of the principle distinctions between fluids and solids is in the different way they dispose of the work done on them in shearing deformations. All the work done on a purely viscous fluid in shear is immediately dissipated as heat, whereas the work done on a perfectly elastic substance in shear is stored and may be recovered by allowing the elastic body to relax. There are many materials that exist between these two idealized limits. They exhibit behavior that is partly fluid-like and partly solid-like. These materials are called viscoelastic substances. The principle phenomenon distinguishing them from purely viscous fluids is the occurrence of strain recovery, or recoil, upon the release of stress. They differ from perfectly elastic solids by exhibiting creep upon loading.

It seems that drag reduction may be linked to the viscoelastic nature of the long-chain polymer additives that are used to produce the phenomena. Therefore, we should give some consideration to the behavior of long-chain viscoelastic polymers in dilute solutions.

An analysis of the dynamic behavior of a polymer molecule in a shear field was carried out with some success by Bueche (40) and later extended by Zimm (61). Bueche started with the Debye picture of the free draining coil (i.e., a sequence of beads, each of which offers hydrodynamic resistance to the flow of the surrounding medium

connected to one another by a string which does not) rotating in a simple shear field. This molecule is supposed to rotate with a frequency of one-half the shear rate. With reference to Figure 39, it can be seen that the monomer units along the line AA' experience a drag force which tends to extend the chain. Along the line BB', however, the drag force tends to compress the chain. Hence, as a monomer unit rotates about the center of gravity of the molecule, it experiences a sinusoidally alternating tension and compression.

Bueche imagined the polymer molecule to be subdivided into a large number of "sub-molecules", each of which behaves mathematically like a small mass attached to a linear spring. The dynamics of the polymer molecule is thereby replaced by the dynamics of a set of masses connected in series by elastic springs. This latter problem, although complex, allows the development of a formal solution for the displacement of each sub-molecule relative to its equilibrium position.

Zimm extended Bueche's model to include the viscosity of the surrounding medium and Brownian motion. For this case Zimm obtains a spectrum of fluid relaxation times:

$$t_i = \frac{\eta_s(\eta - \eta_s)M}{(\eta_s C)\ 0.586\ \alpha_i RT}$$

where t_i is the relaxation time of the i-th mode of vibration, R the gas constant, T the absolute temperature, M the molecular weight, C the polymer concentration, η_s the solvent viscosity, η the solution viscosity, and α_i the eigenvalues:

$$\alpha_1 = 4.04;\quad \alpha_2 = 12.79;\quad \alpha_3 = 24.2;\quad \text{etc.}$$

The expression $(\eta - \eta_s)\eta_s C$ may be replaced by the intrinsic viscosity, $[\eta]$, at small polymer concentrations. $[\eta]$ can usually be related to

the molecular weight, M, by an expression of the form:

$$[\eta] = K M^a$$

where "K" and "a" are constants to be determined for each different polymer. The higher the molecular weight within a given series of linear polymer homologs, the greater the increase in viscosity produced by a given weight concentration of polymer. In other words, the intrinsic viscosity, $[\eta]$, which represents the capacity of a polymer to enhance the viscosity, increases with M; hence, viscosity measurements afford a measure of molecular weight. Intrinsic viscosity is defined as:

$$[\eta] = \lim_{C \to 0} \left\{ \eta_{sp}/C \right\} ,$$

where

$$\eta_{sp} = \frac{\eta}{\eta_s} - 1 \quad .$$

Polyethylene oxide, manufactured by Union Carbide, is the best water soluble drag reducing polymer that has been found so far. For this reason, it has been widely used and has been well characterized. Shin (38) has found that the intrinsic viscosity of PEO is related to its weight average molecular weight by

$$[\eta] = 1.03 \times 10^{-4} \bar{M}_{wt}^{0.78} \quad .$$

The intrinsic viscosity of the PEO homolog used in this study was calculated by measuring the viscosity of four different dilute concentrations of PEO-FRA in tap water with a Brookfield Synchro-electric viscometer, using the UL adapter and operating at 60 rpm. A small amount of isopropal, 0.83% by volume, was added to the solution as a chemical stabilizer to help slow down oxidation degradation in the tap

water. Figure 40 shows a plot of η_{sp}/C and $(\ell n\, \eta_r)/C$ versus concentration (gm/dl). Both of these functions approach $[\eta]$ as $C \to 0$.

The intrinsic viscosity of the PEO used in this study was found to be $[\eta] = 25 \pm 2$, corresponding to a weight average molecular weight of $\bar{M}_{wt} = 7.5 \pm 0.5 \times 10^6$. Shin also determined that the rms radius of gyration for this size PEO molecule should be $z = 3000$ Å. The first order Zimm relaxation time is calculated to be equal to 3.2 milliseconds.

A thermodynamically dilute concentration for a solution of this polymer (i.e., the polymers are separated from each other further than if they were just touching each other in a spherically packed configuration) exists at concentrations less than 240 wppm. Shin (38) has pointed out that a dilute polymer solution has an essentially Newtonian viscosity in simple shear. As a check, the viscosity of a 100 wppm solution of PEO-FRA was measured with the Brookfield Viscometer. The solution was found to be Newtonian (i.e., the viscosity was constant) over a range of shear rates from 3.1 $sec.^{-1}$ to 15.5 $sec.^{-1}$. Thus the wall shear was estimated from

$$\tau_w = \eta \left.\frac{\partial \bar{U}}{\partial Y}\right|_{Y=0}$$

The solution that is being used in this study is polyethylene oxide-FRA in water at a concentration of 139 wppm. The solution consists of 2,270 kilograms of tap water, 320 grams of PEO-FRA, 37 kilograms of isopropanol and 3 kilograms of formaldehyde (the latter two in order to slow down chemical and/or biological degradation).

The 139 wppm solution was prepared by slowly adding a PEO-isopropanol slurry (320 grams PEO-4 liters isopropanol, held in

suspension by continuous stirring) to the open-top tank containing the water-isopropanol-formaldehyde mixture. The solution in the open tank was slowly stirred with paddles during the slurry addition and the final solution was allowed to stand for two hours before it was used in a test. Pressure drop tests were run with the water-isopropanol mixture before the dilute polymer solution was prepared and then again at the beginning and end of each experiment using the polymer solution. The first pressure drop test was to ensure that the solution was not contaminated from previous experiments and the later tests were used to determine the amount of friction reduction (also the amount of polymer degradation) that was obtained with the dilute polymer solution.

APPENDIX E

DATA TABULATIONS

TABLE V

LAMIR VELOCITY PROFILE DATA

Mass Averaged Velocity (Experiment Number)	Y (in)	$\overline{U}$ (ft/sec)	u' (ft/sec)	N	U_f (ft/sec)
0.23 ft/sec (4,5)	0.026	0.055	0.024	69	0.022
	0.042	0.071	0.030	100	0.024
	0.057	0.101	0.038	112	0.020
	0.094	0.218	0.041	76	0.106
	0.177	0.248	0.036	27	0.106
	0.344	0.286	0.034	47	0.106
	0.512	0.288	0.031	38	0.106
	0.679	0.289	0.026	24	0.106
	0.842	0.293	0.020	40	0.106
0.69 ft/sec (4,5)	0.026	0.285	0.091	64	0.215
	0.094	0.653	0.077	111	0.518
	0.177	0.671	0.076	43	0.518
	0.344	0.727	0.087	50	0.518
	0.512	0.758	0.065	48	0.518
	0.679	0.806	0.075	46	0.518
	0.846	0.809	0.060	43	0.518
0.43 ft/sec (5)	0.026	0.139	0.054	72	0.055
	0.042	0.199	0.069	104	0.076
0.69 ft/sec (6)	0.015	0.072	0.027	44	0.053

TABLE VI

FRICTION-REDUCTION DATA

Tube Diameter & Length	Q ± 0.02 (gal/min)	Experiment Number 6 ΔP ± 0.05 inches of water			Experiment Number 8&9 ΔP ± 0.05 inches of water		
		Water	Before Run #1	After Run #2	Water	Before Run #1	After Run #2
D=0.835 in.	1.03	0.30	0.20	0.25	0.35	0.25	0.25
	1.37	0.50	0.30	0.40	0.55	0.35	0.35
L=9.46 ft.	1.71	0.75	0.35	0.69	0.80	0.45	0.45
	2.05	1.05	0.50	0.70	0.10	0.60	0.60
	2.40	1.45	0.60	0.90	1.45	0.70	0.75
	2.74	1.80	0.70	1.05	1.85	0.80	0.90
	3.08	2.30	0.80	1.20	2.25	0.90	1.05
	3.42	2.80	0.95	1.40	2.70	1.00	1.25
	3.77	3.25	1.15	1.55	3.20	1.20	1.45
	4.11	3.80	1.30	1.75	3.80	1.40	1.60
	4.45				4.40	1.50	1.80
D=0.425 in.	0.67				4.40		1.90
	1.03	8.90		3.50	8.90		3.30
L=9.21 ft.	1.37	13.10		4.90	13.10		4.90
	1.71	18.90		6.50	18.90		5.60
	2.05	25.90		8.30	25.90		8.30
	2.40	33.90		10.30	33.90		10.20
	2.74	42.60		12.50	42.60		17.10

APPENDIX F

FIGURES AND ILLUSTRATIONS

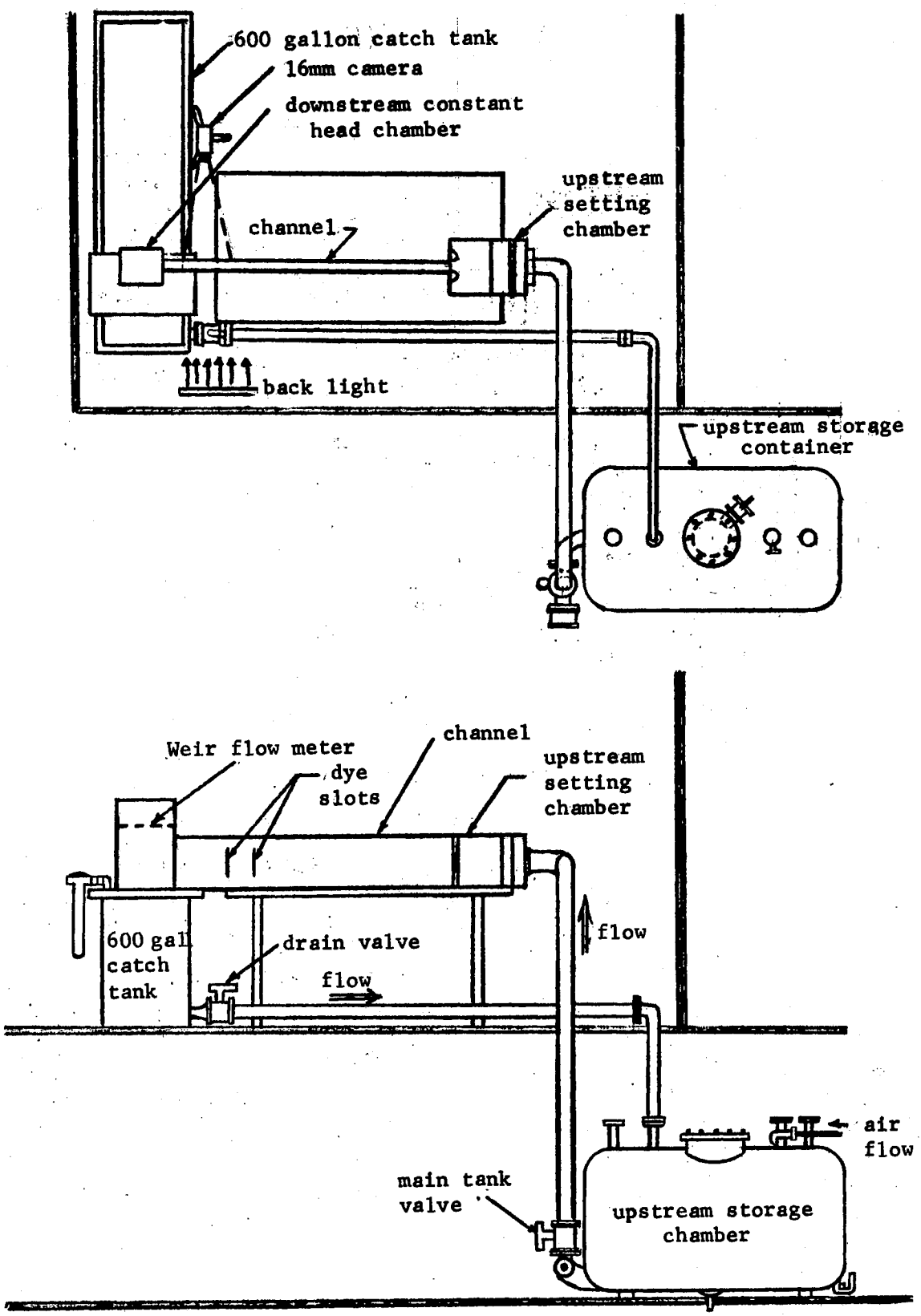

Figure 1. Water Channel and Circulation System

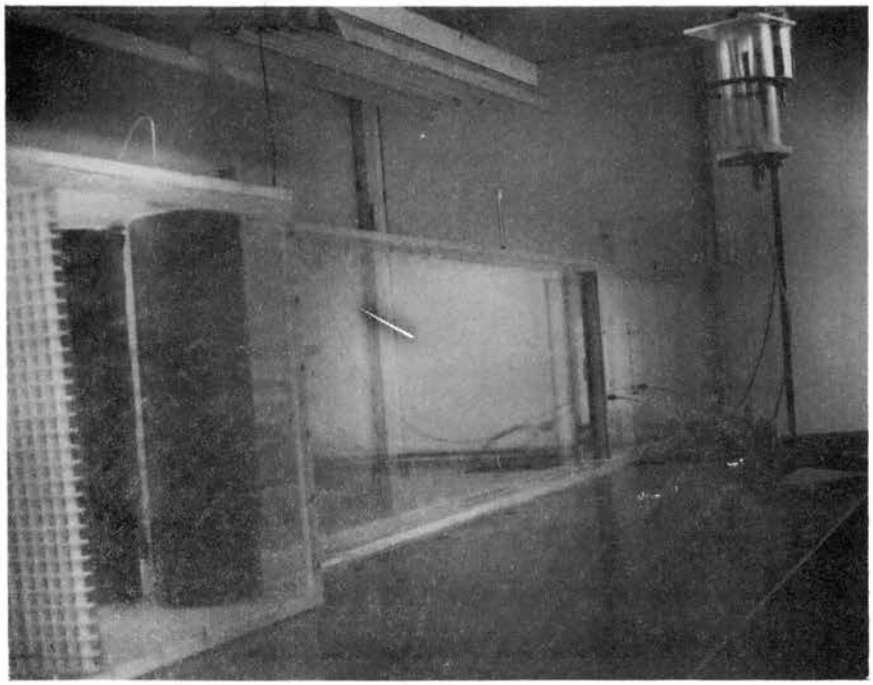

Figure 2. Photograph of Water Channel

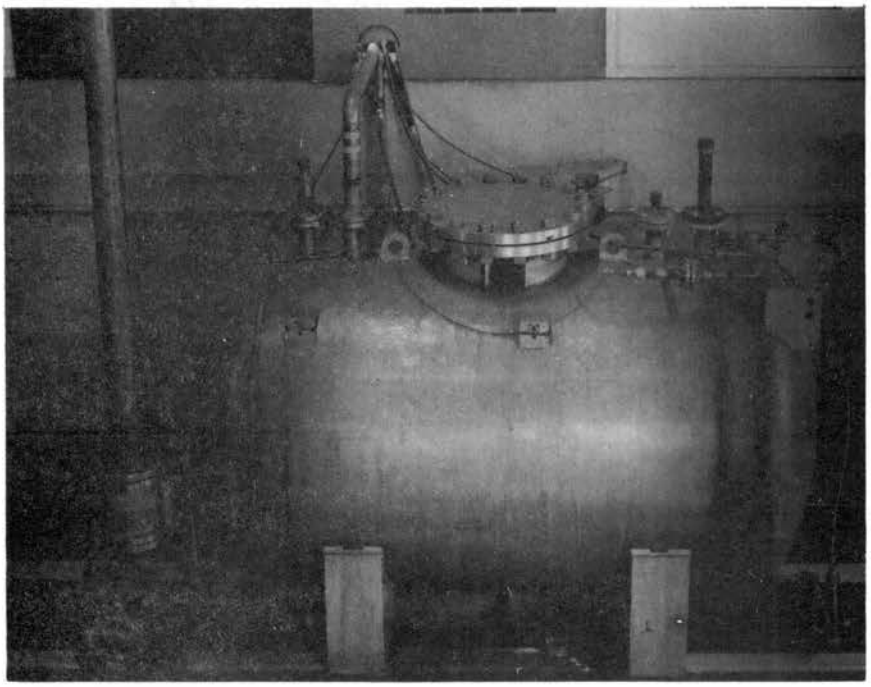

Figure 3. Photograph of 600 Gallon Pressurized Storage Container

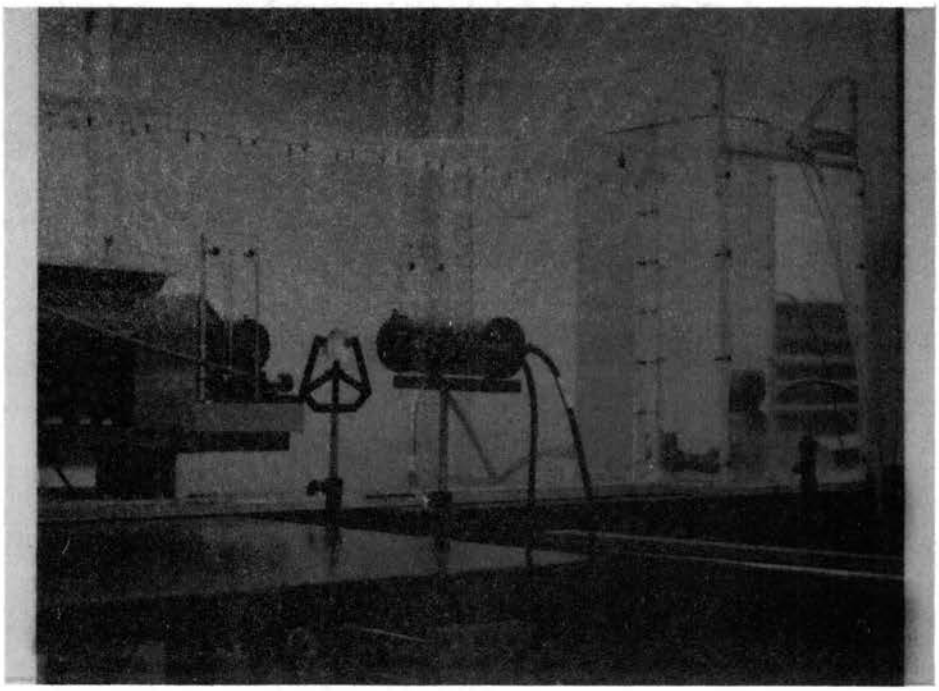

Figure 4. Photograph of Turbulent Channel Test Section, Dye Slots and Laser Optics

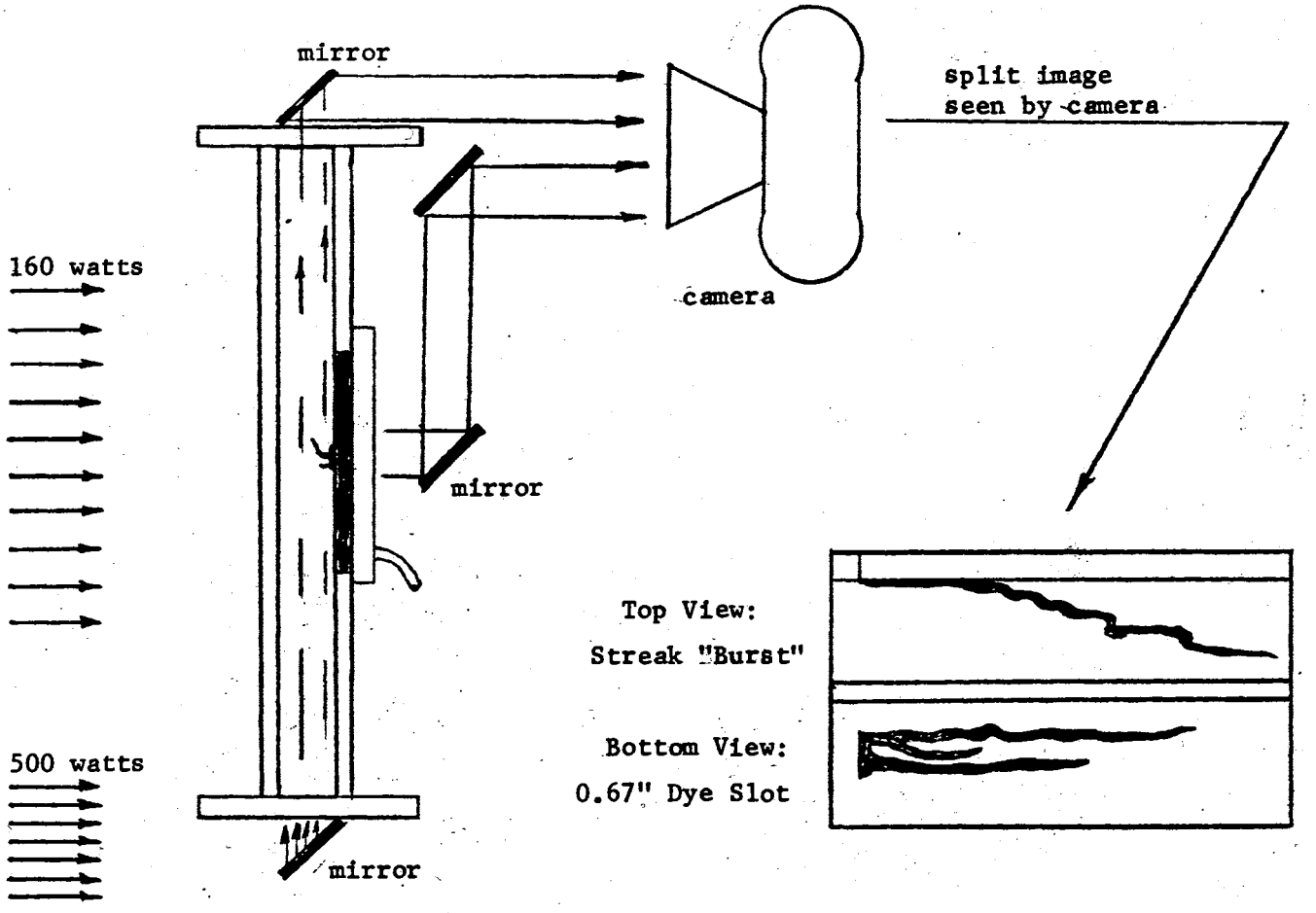

Figure 5. Channel Cross Section Showing the Split Image Optical Arrangement Used in Photographing the Low Speed Streak Bursting

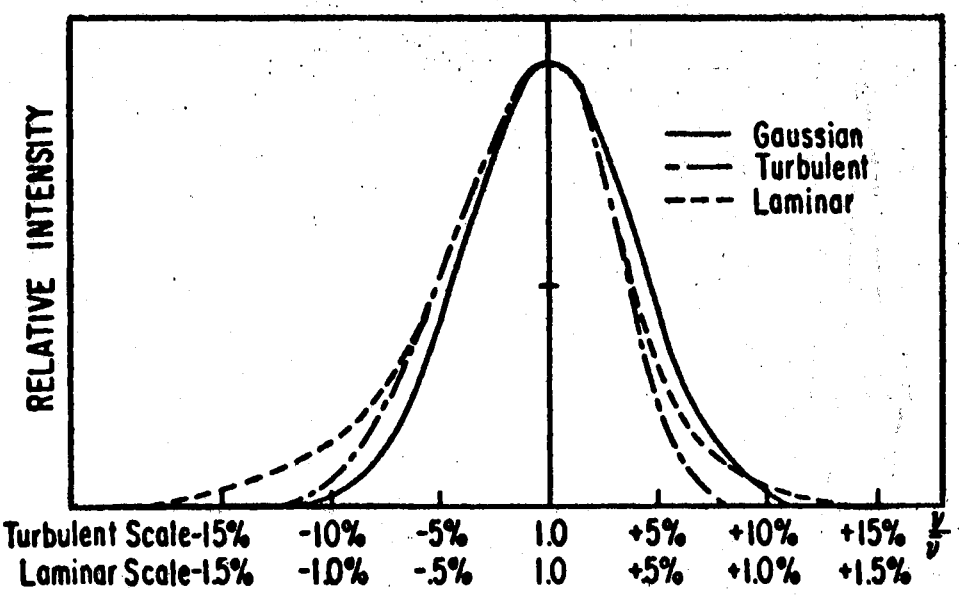

Figure 6. Turbulence Measurements by Spectral Broadening, Goldstein and Hagen (15)

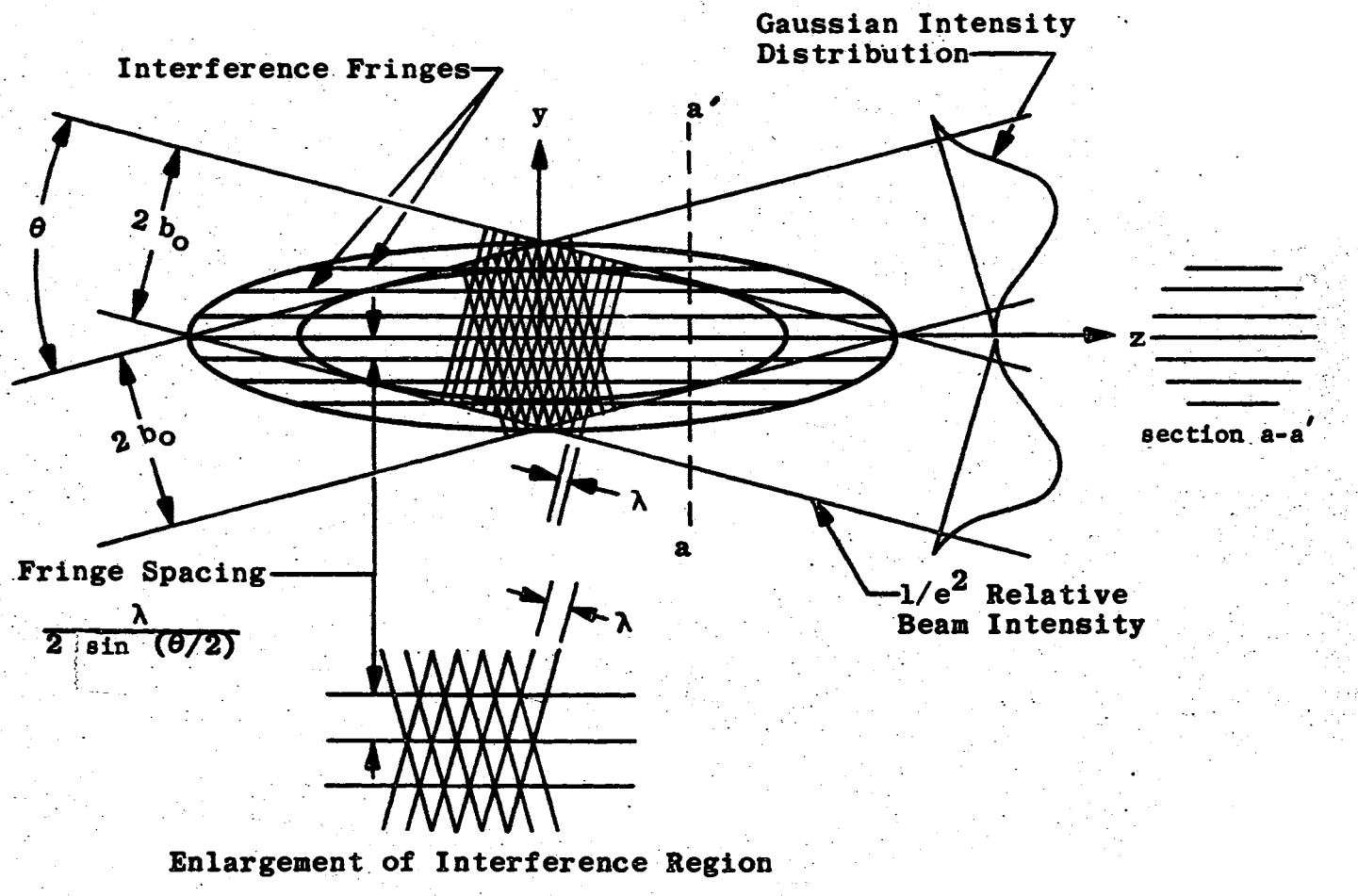

Figure 7. Beam Crossover Fringes, Brayton, et al. (2).

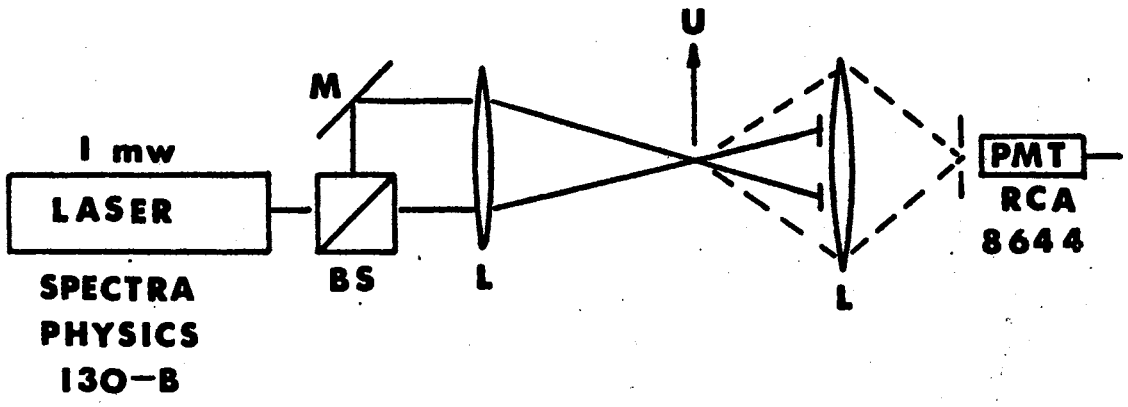

Figure 8. Scatter-Scatter Electro-Optical System

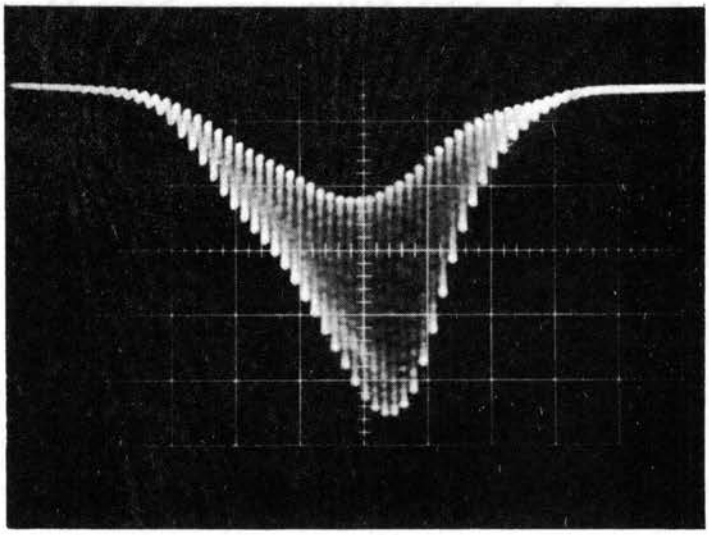

Figure 9. Unfiltered Doppler Frequency Burst

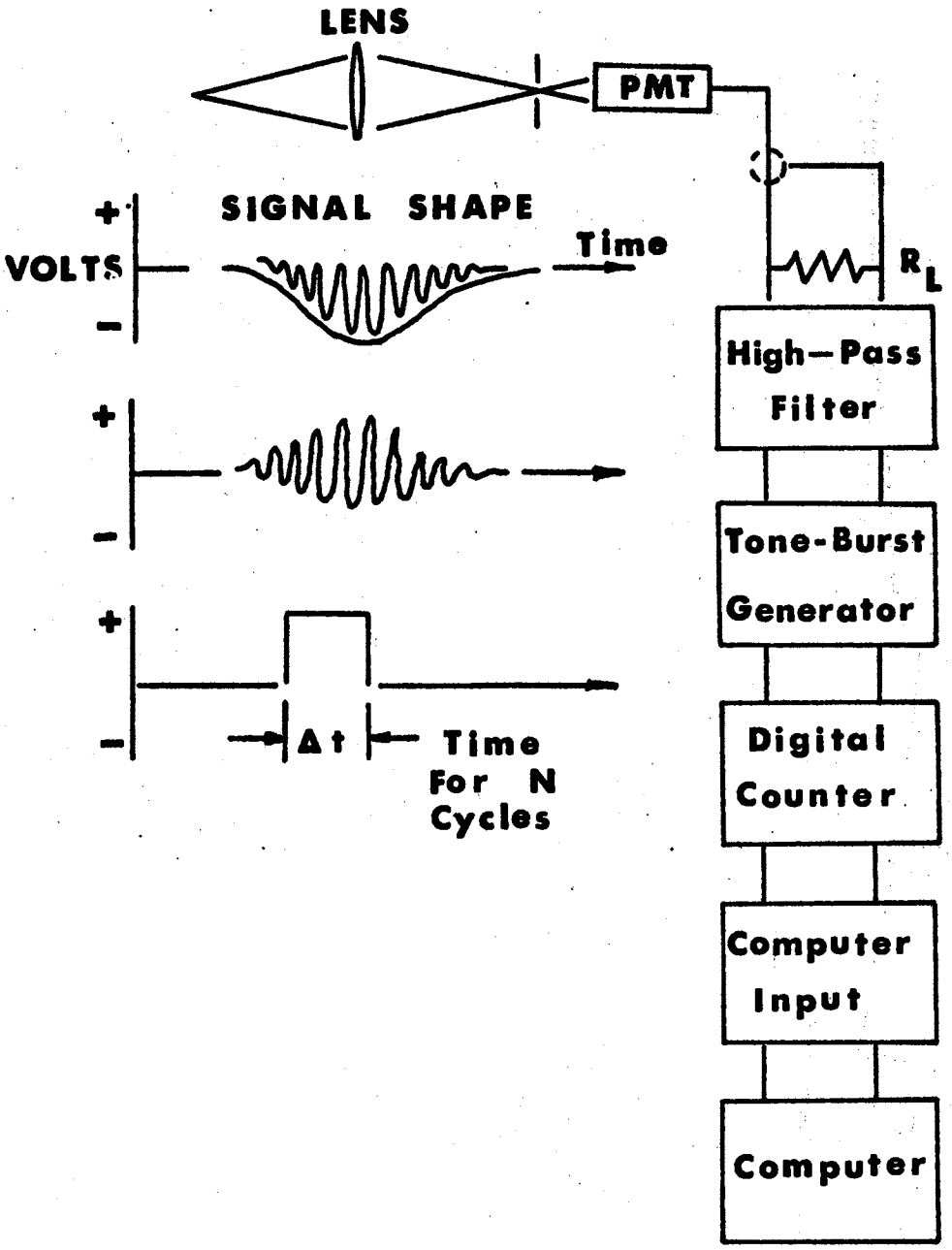

Figure 10. LAMIR Data Processing System.

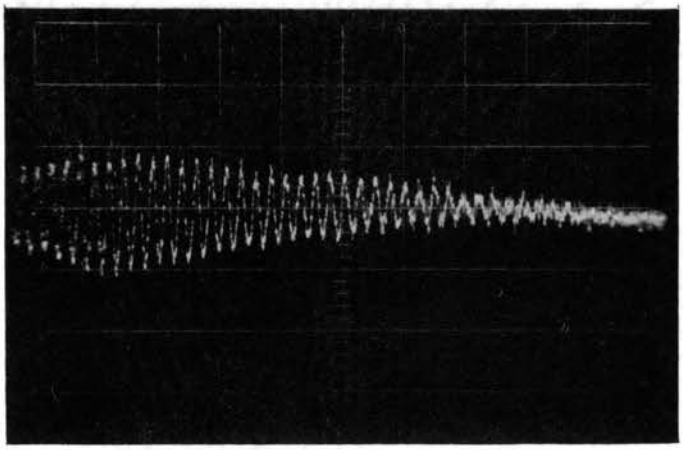

Figure 11. High Pass Filtered Doppler Frequency Burst

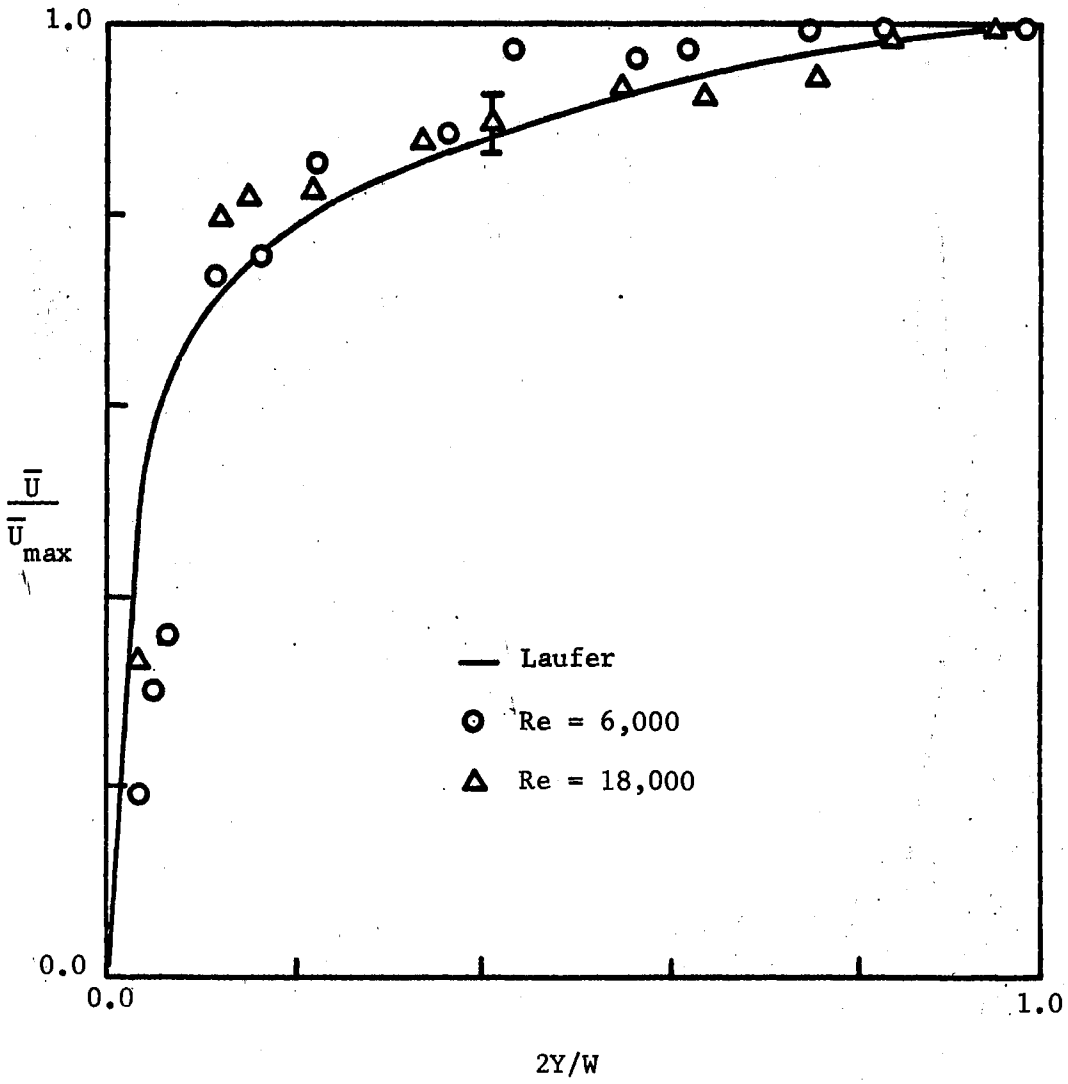

Figure 12. Normalized Channel Velocity Profiles

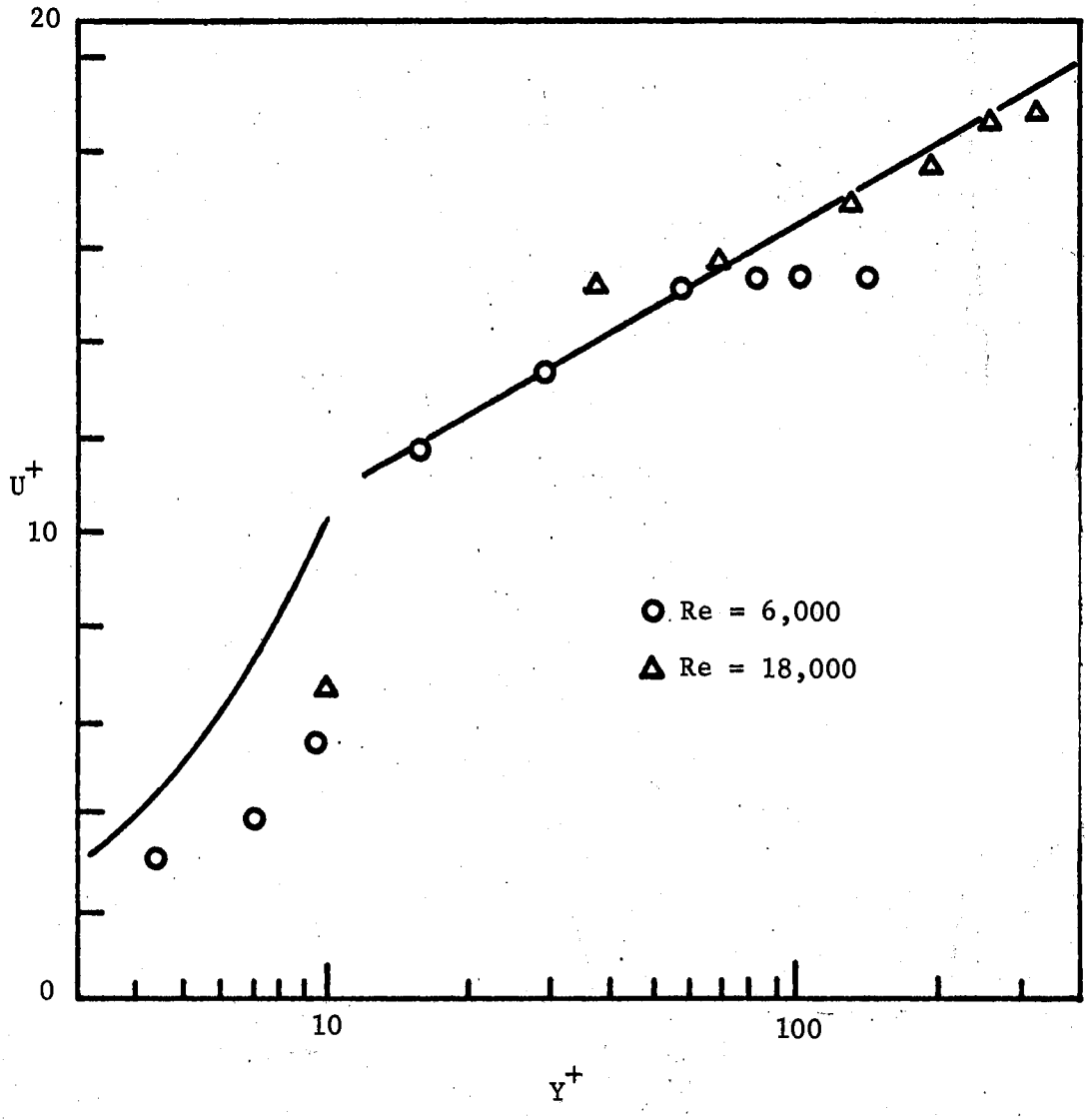

Figure 13. Turbulent Channel Velocity Profile--Law of the Wall Plot

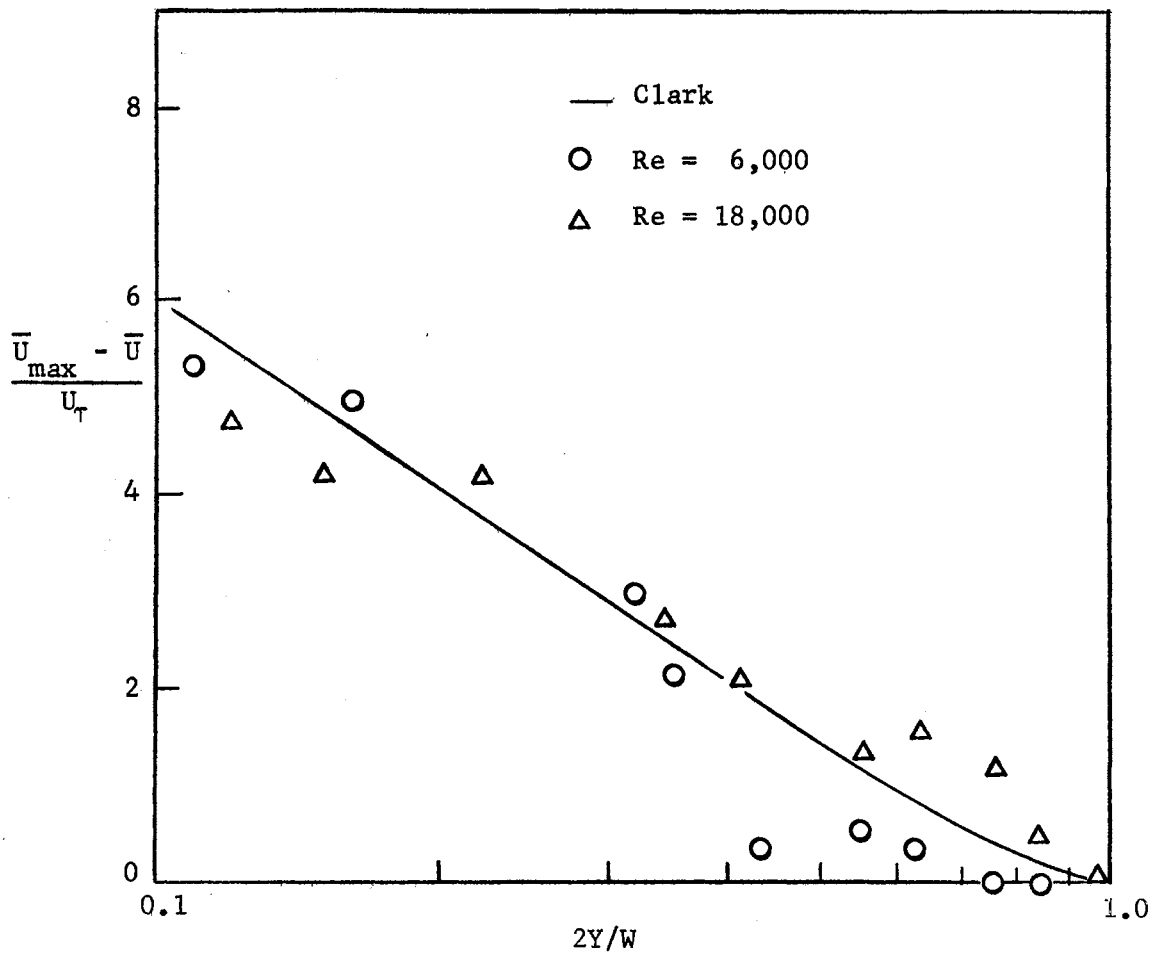

Figure 14. Turbulent Channel Velocity Profile--Velocity Defect Plot

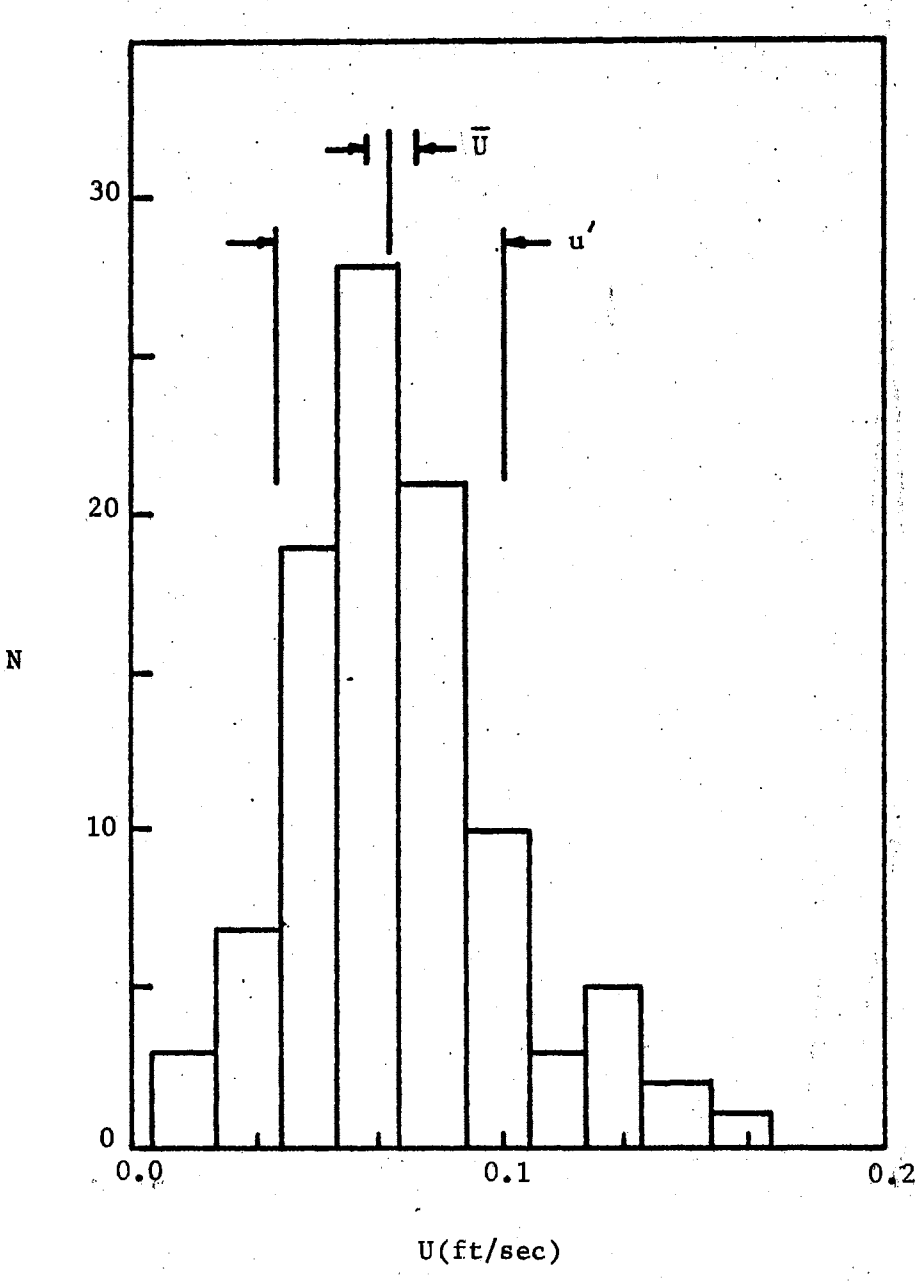

Figure 15. Typical Velocity Distribution Histogram; $R_e = 6000$, $y^+ = 7$

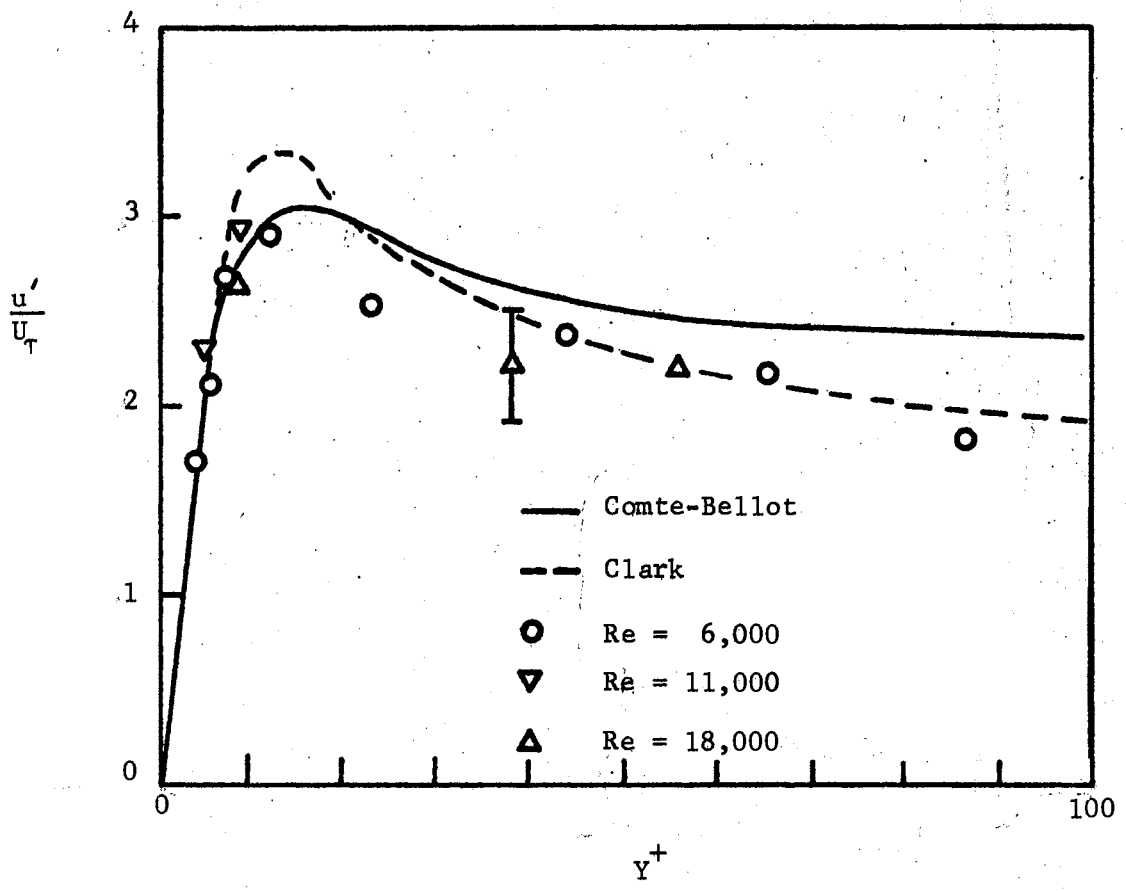

Figure 16. Axial Turbulent Intensity Profile.

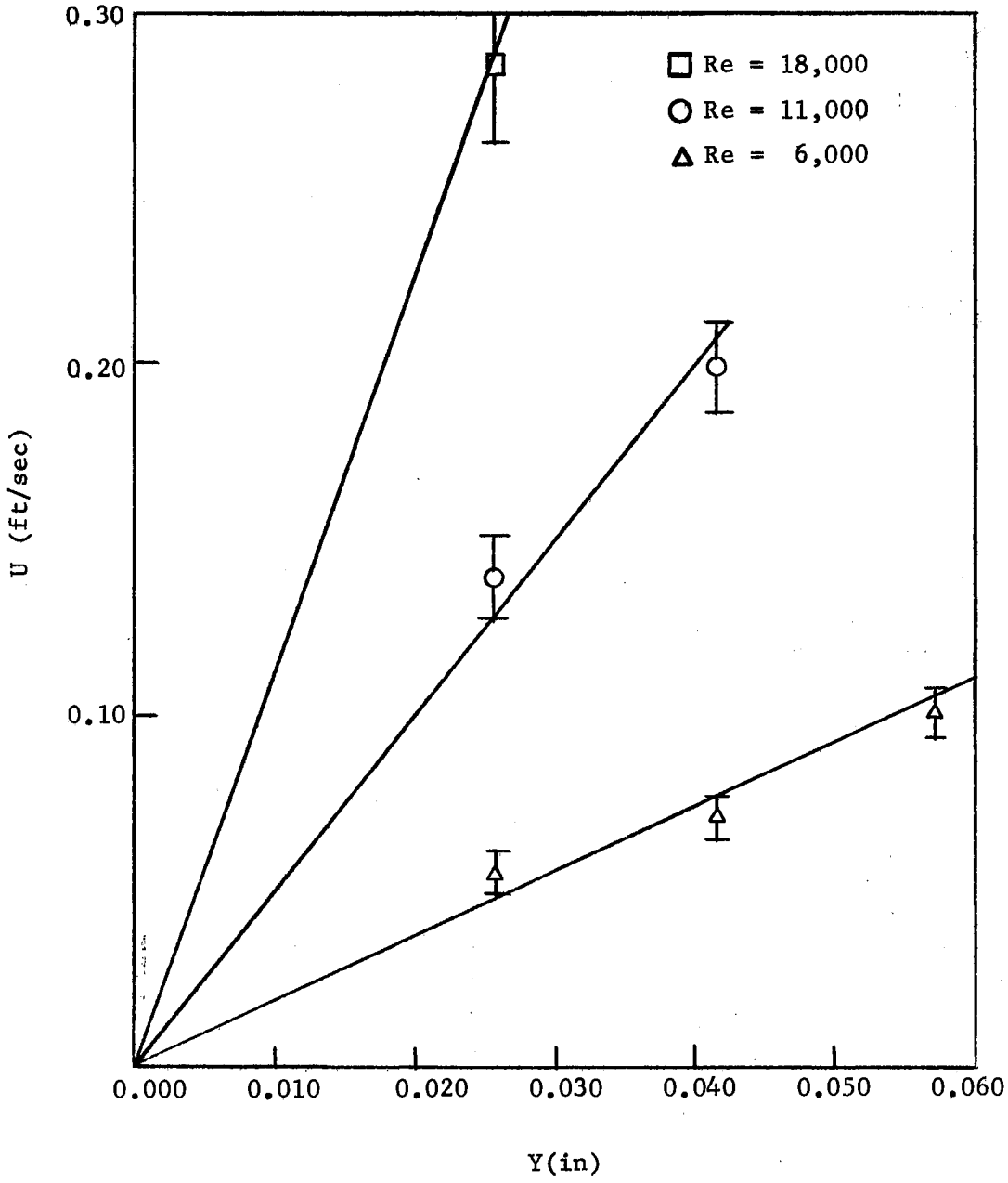

Figure 17a. Local Mean Velocity Profile in the Viscous Sublayer

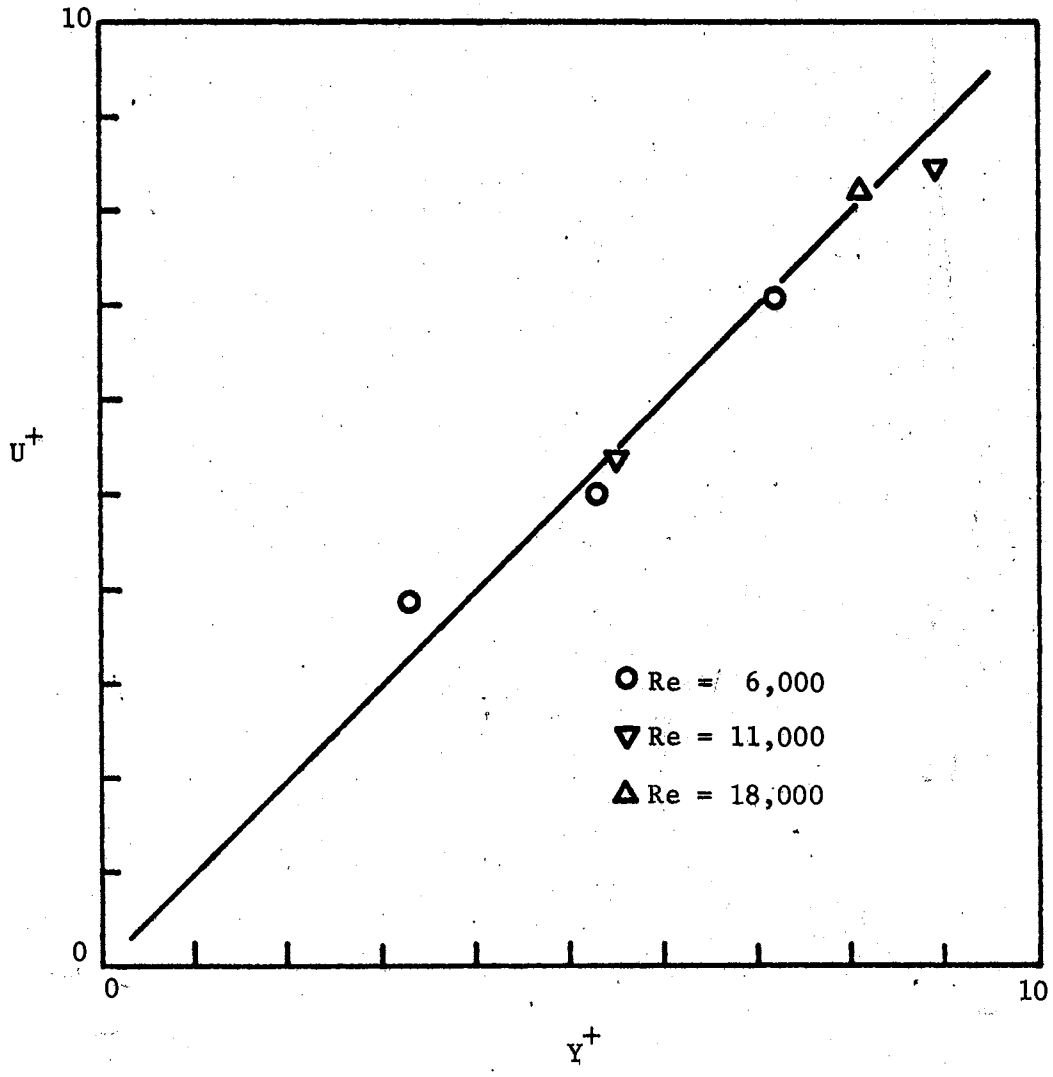

Figure 17b. Turbulent Channel Velocity Profile--Sublayer ($U^+ = Y^+$).

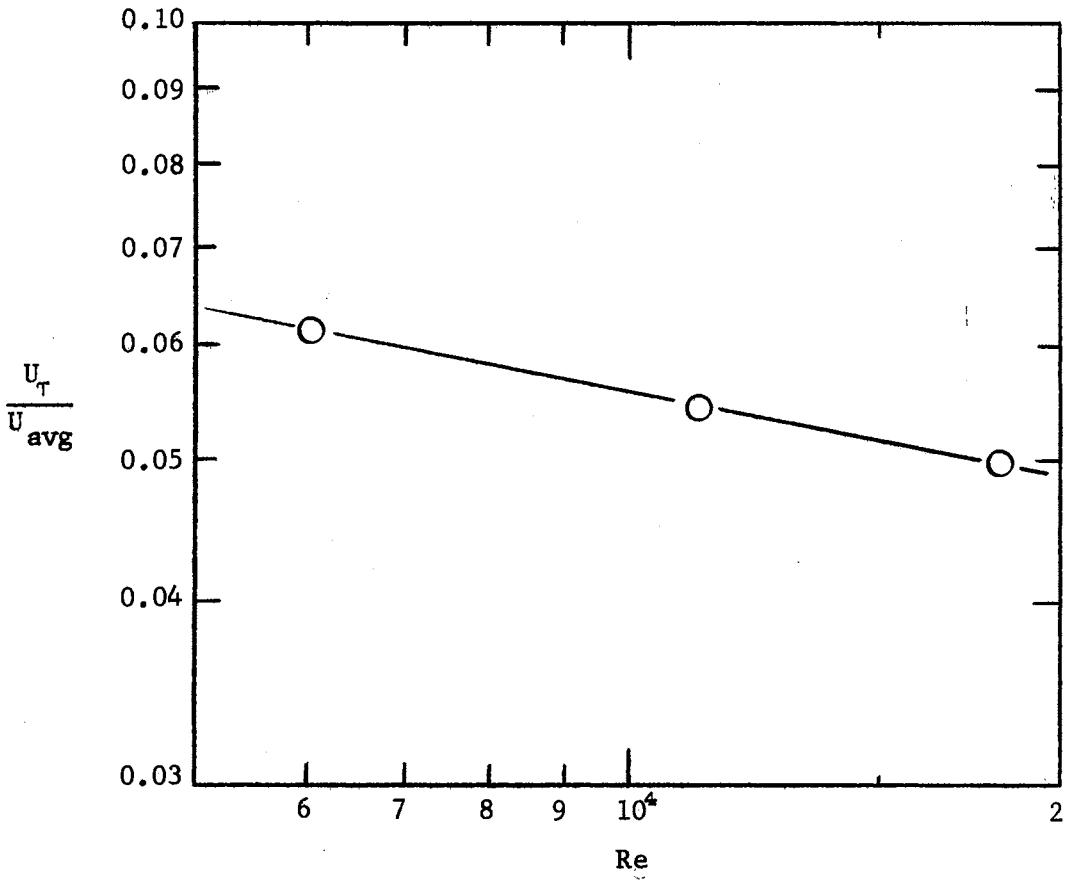

Figure 17c. Nondimensionalized Channel Wall Shear Velocity.

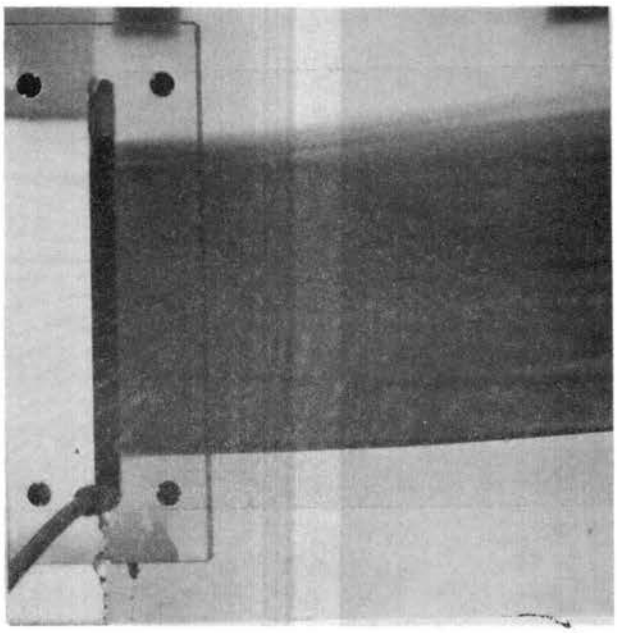

Figure 18. Photograph of Dye Injection Into Laminar Flow

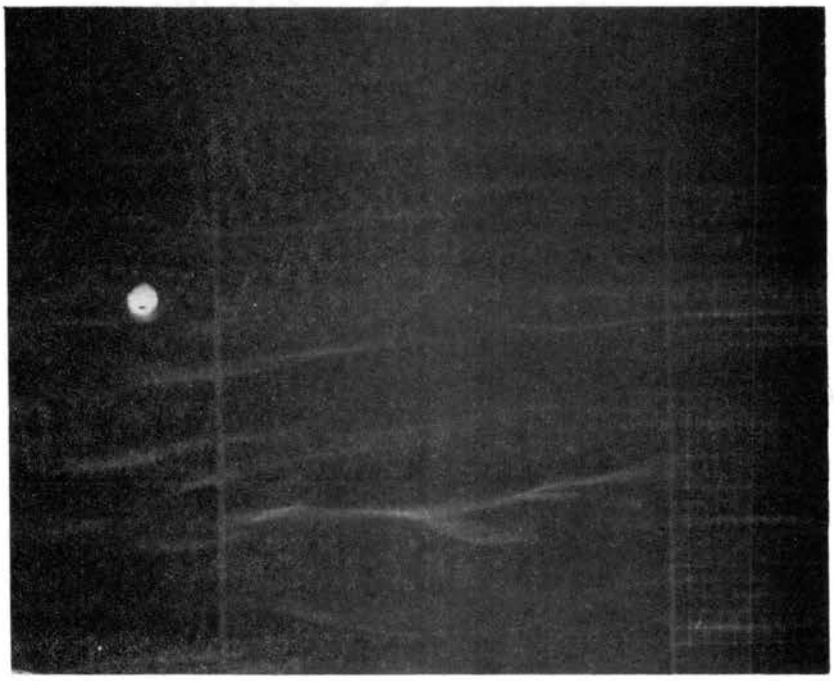

Figure 19. Photograph of Streak Spacing in Water ($\overline{U}_{avg} \approx$ 0.23 ft/sec)

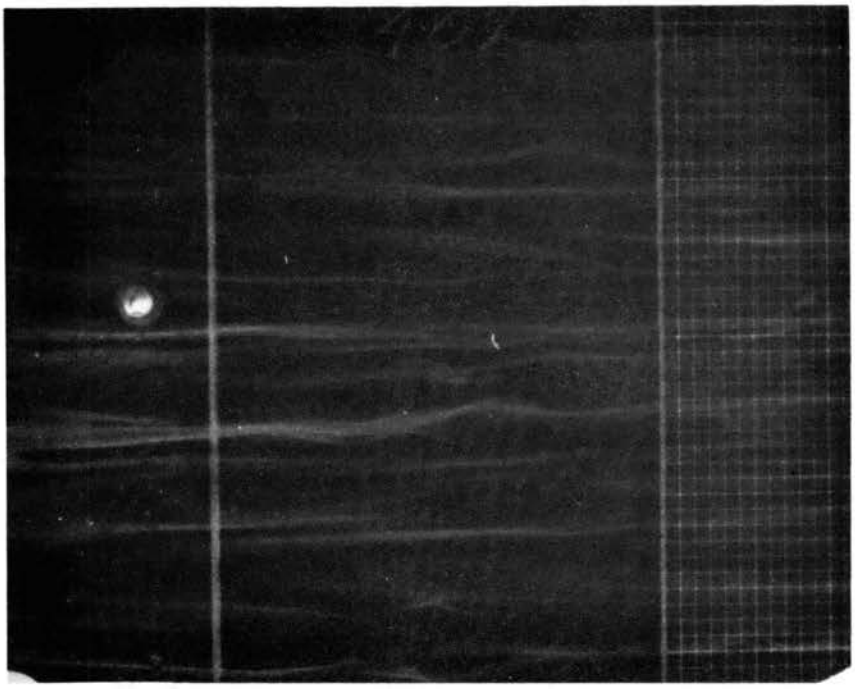

Figure 20. Photograph of Streak Spacing in Water ($\bar{U}_{avg}$ = 0.43 ft/sec)

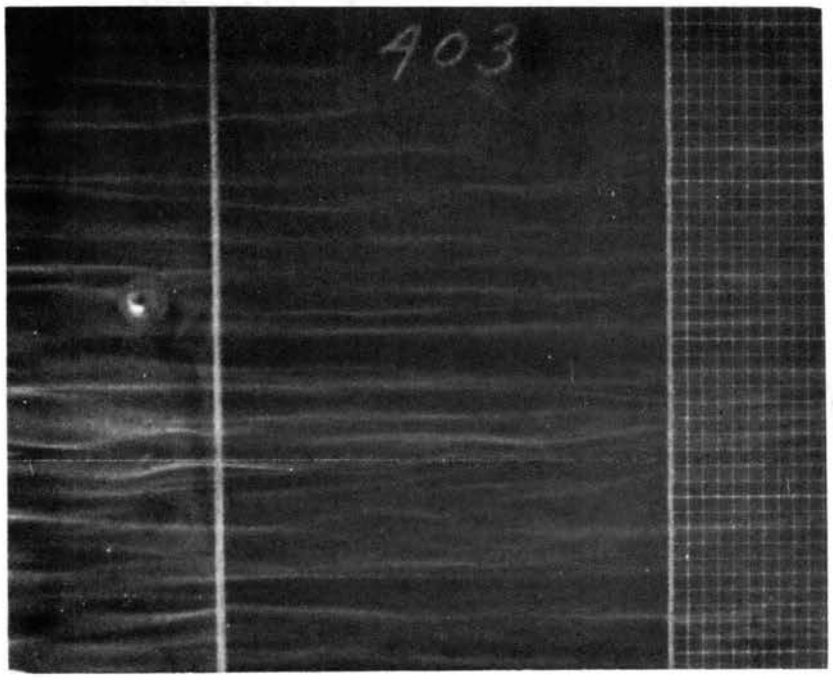

Figure 21. Photograph of Streak Spacing in Water ($\bar{U}_{avg}$ = 0.69 ft/sec)

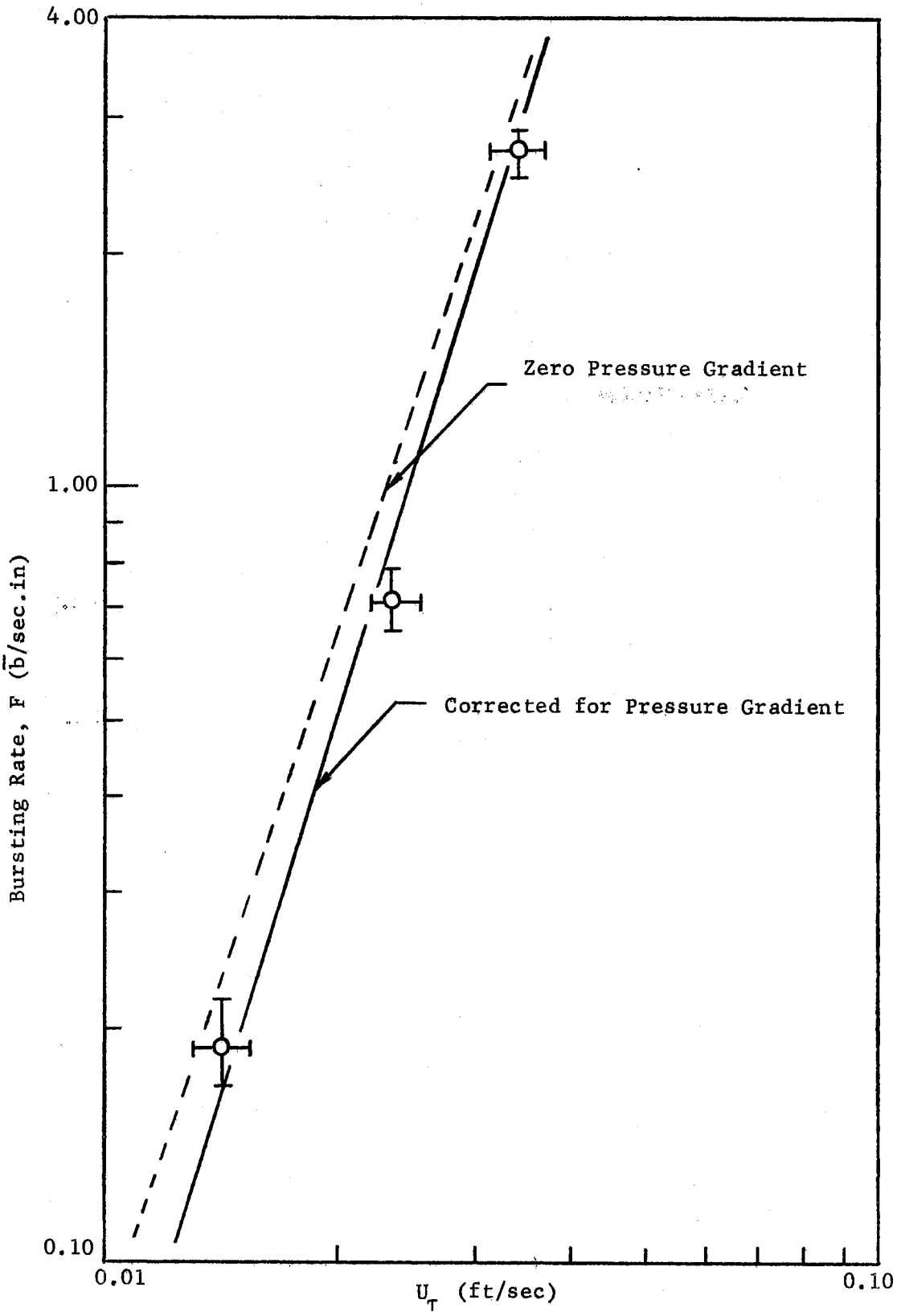

Figure 22. Bursting Rates in Water.

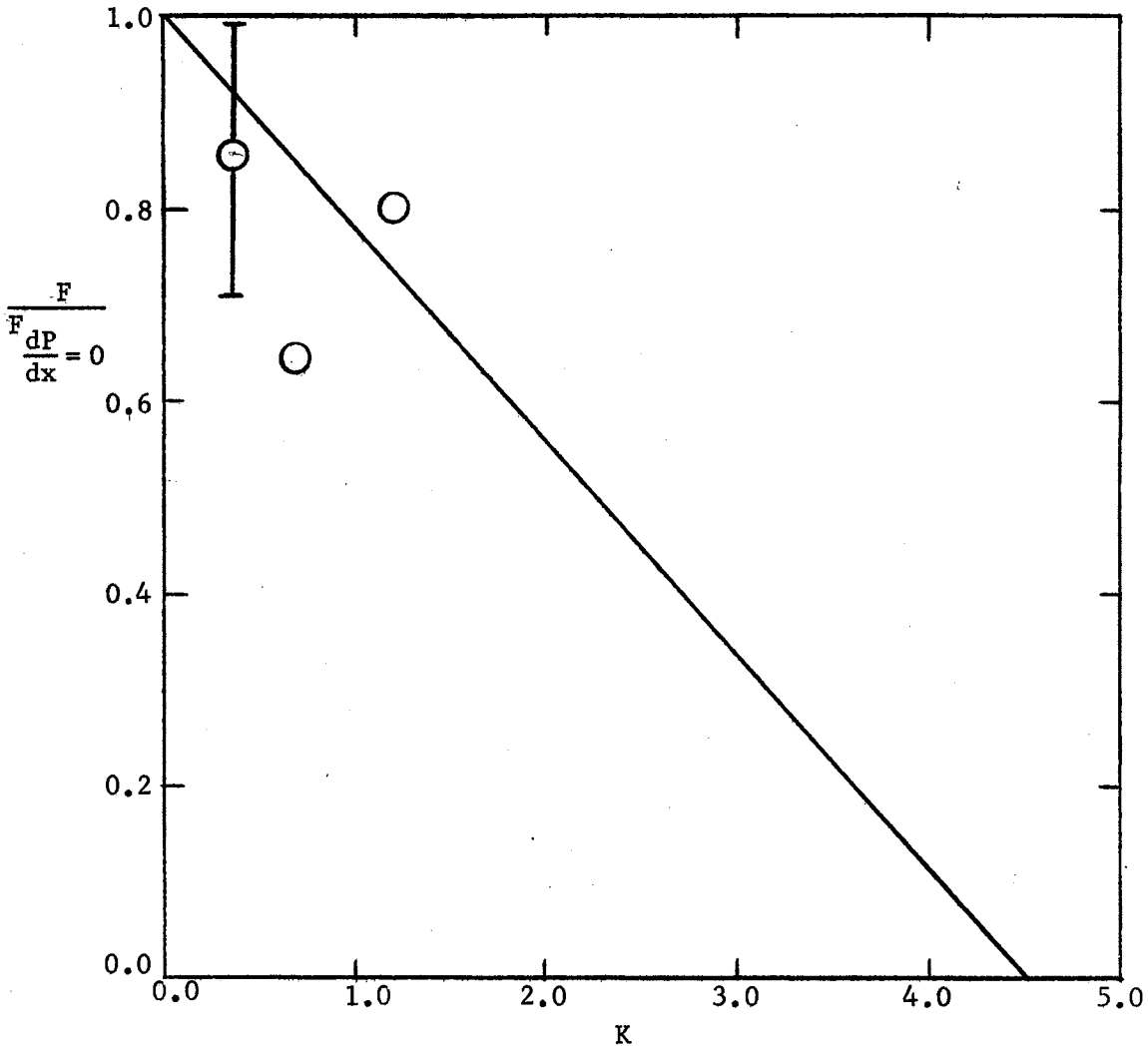

Figure 23. Pressure Gradient Effect on Bursting Rates

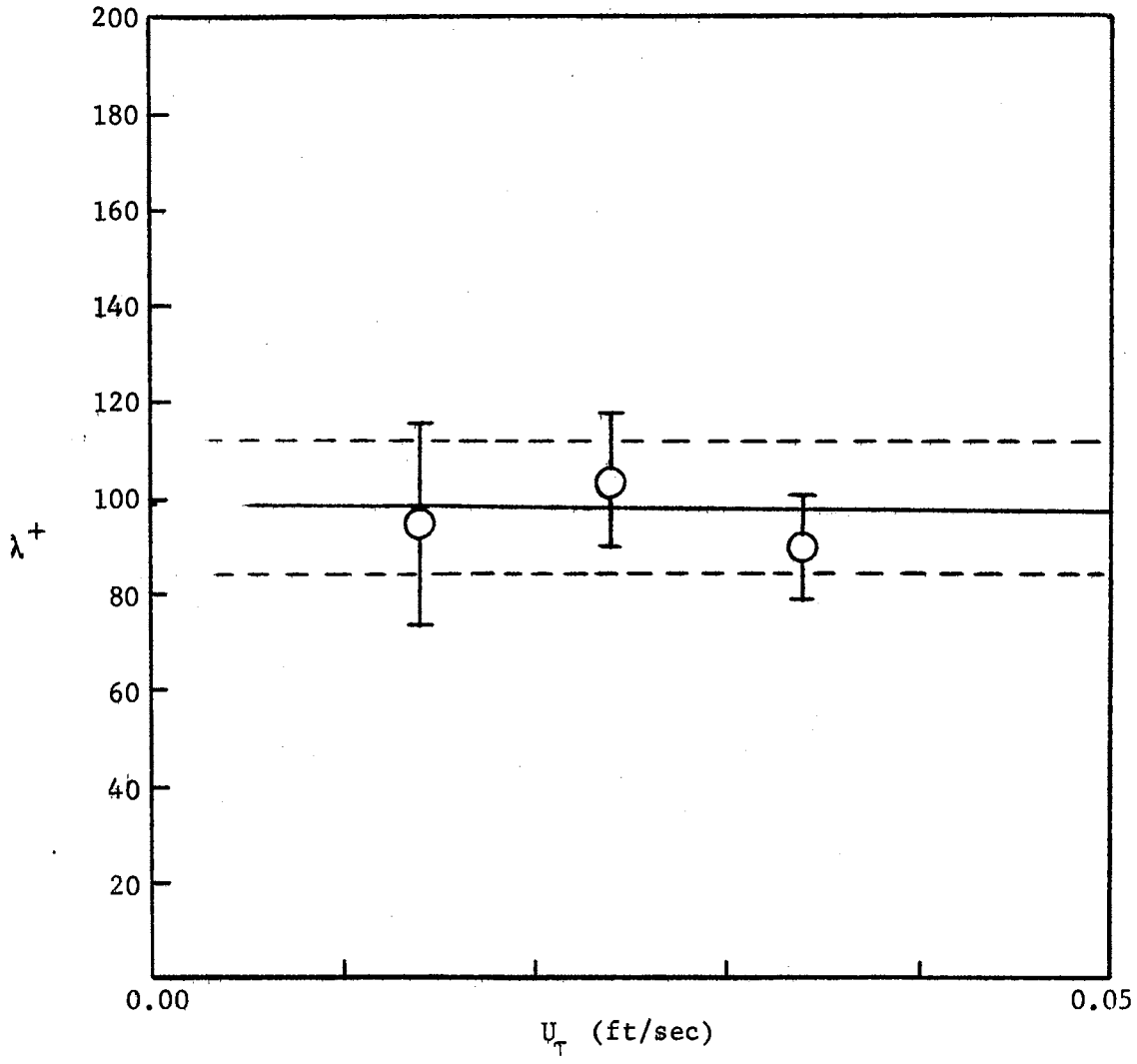

Figure 24. Nondimensional Streak Spacing in Water.

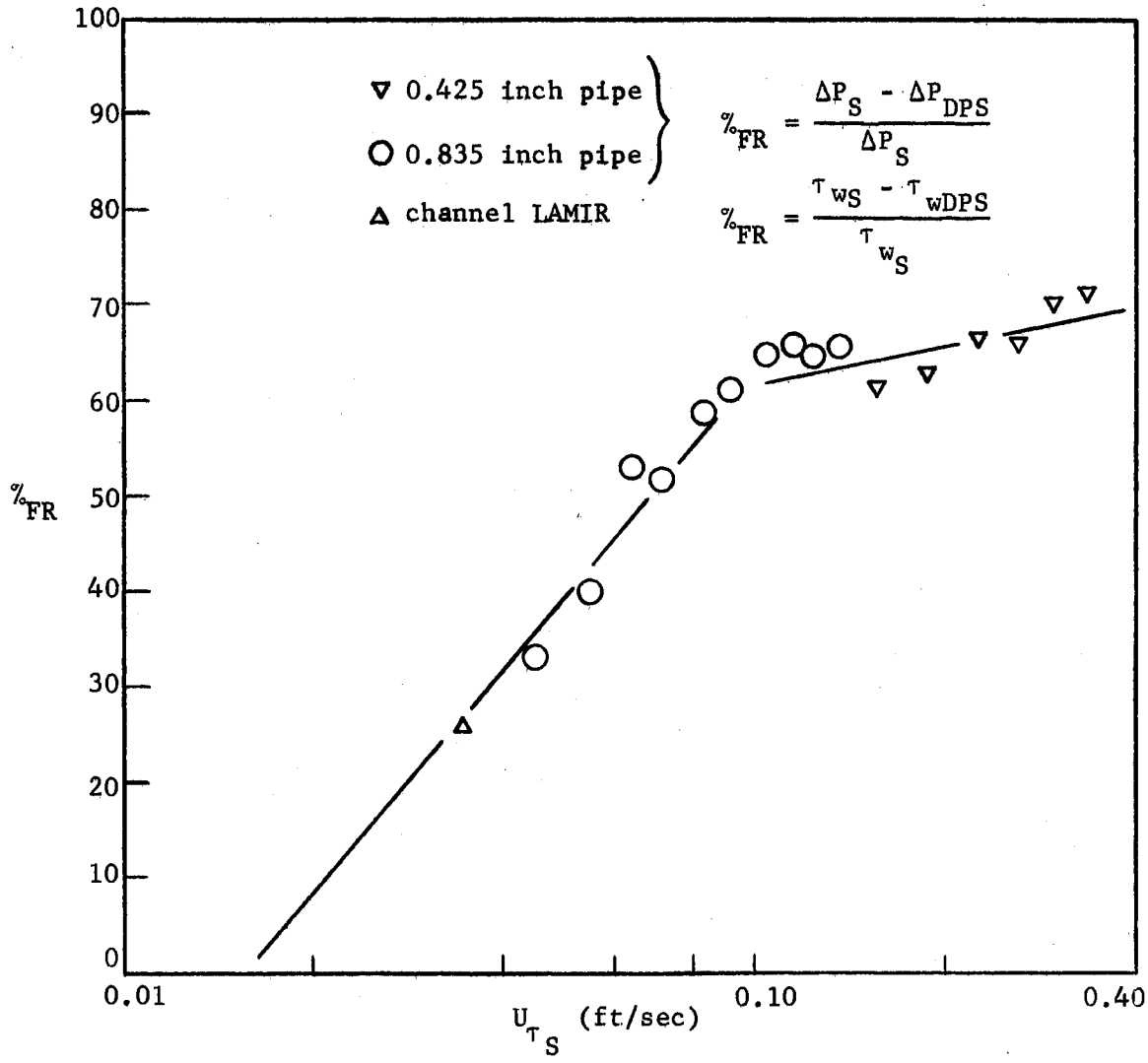

Figure 25. Per Cent Friction Reduction.

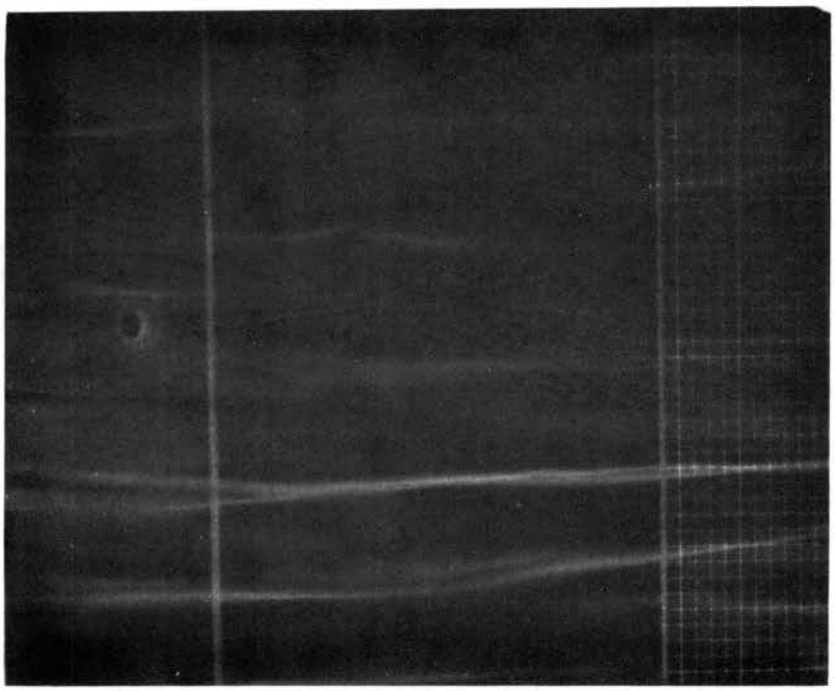

Figure 26. Photograph of Streak Spacing in Polymer Solution ($\bar{U}_{avg}$ = 0.43 ft/sec, 139 wppm PEO)

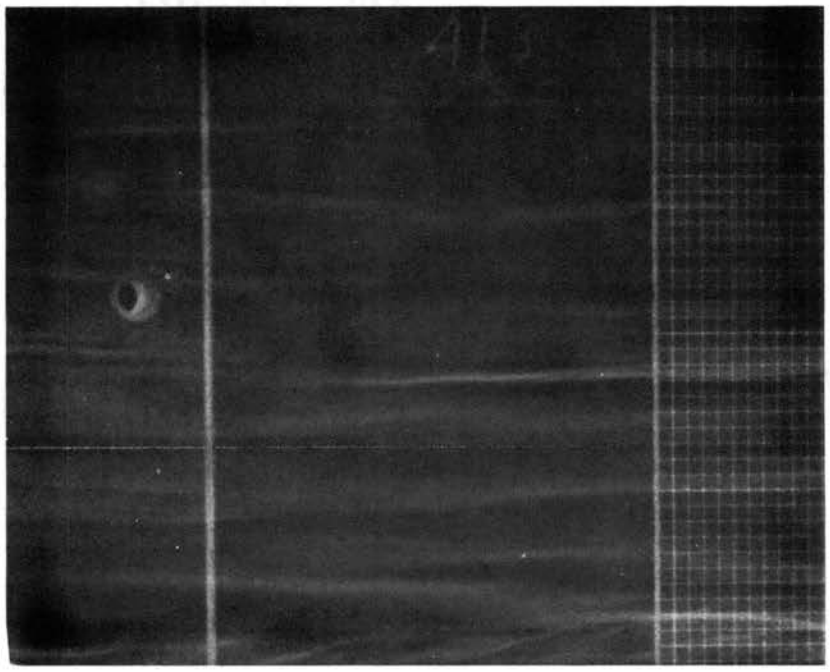

Figure 27. Photograph of Streak Spacing in Polymer Solution ($\bar{U}_{avg}$ = 0.69 ft/sec, 139 wppm PEO)

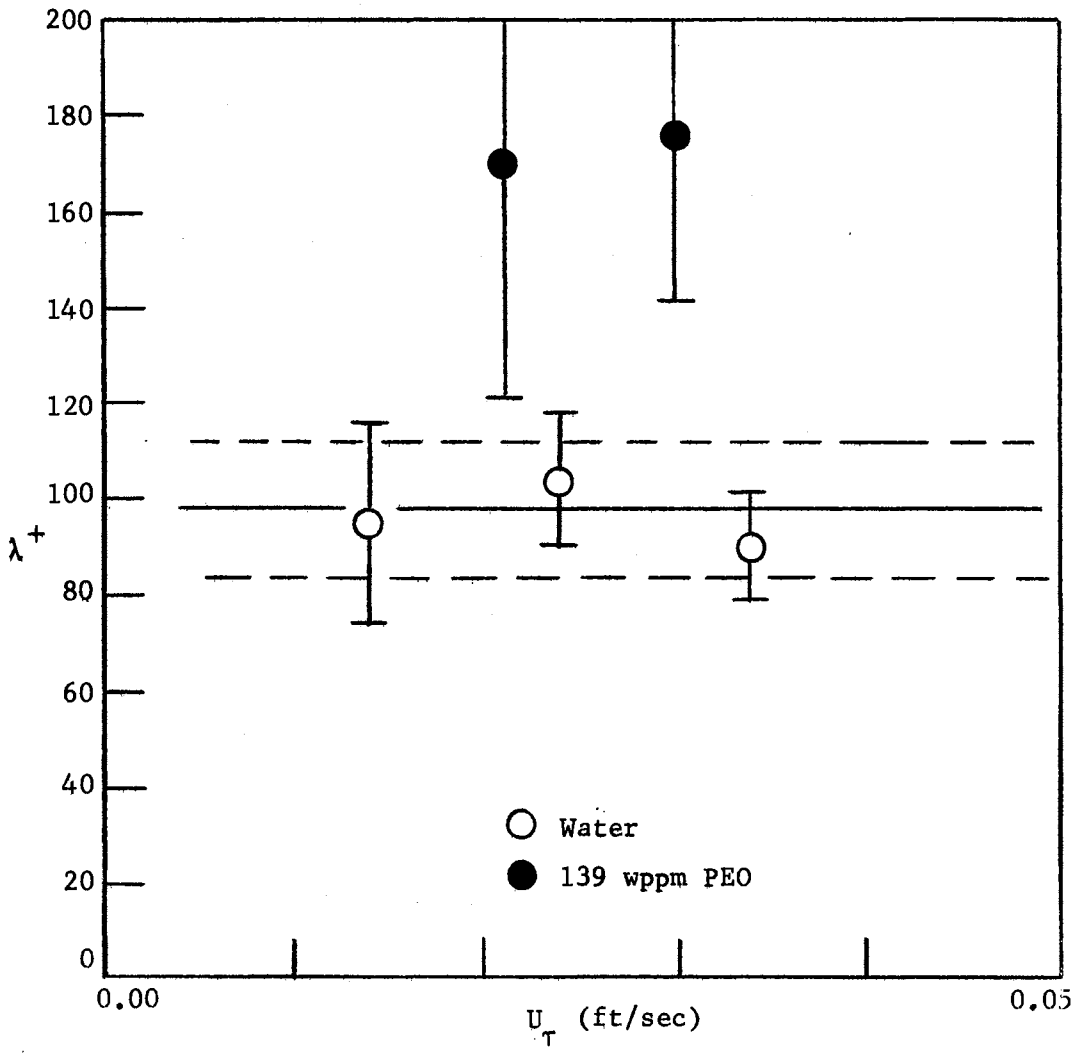

Figure 28. Nondimensional Streak Spacing in Water and Polymer Solution

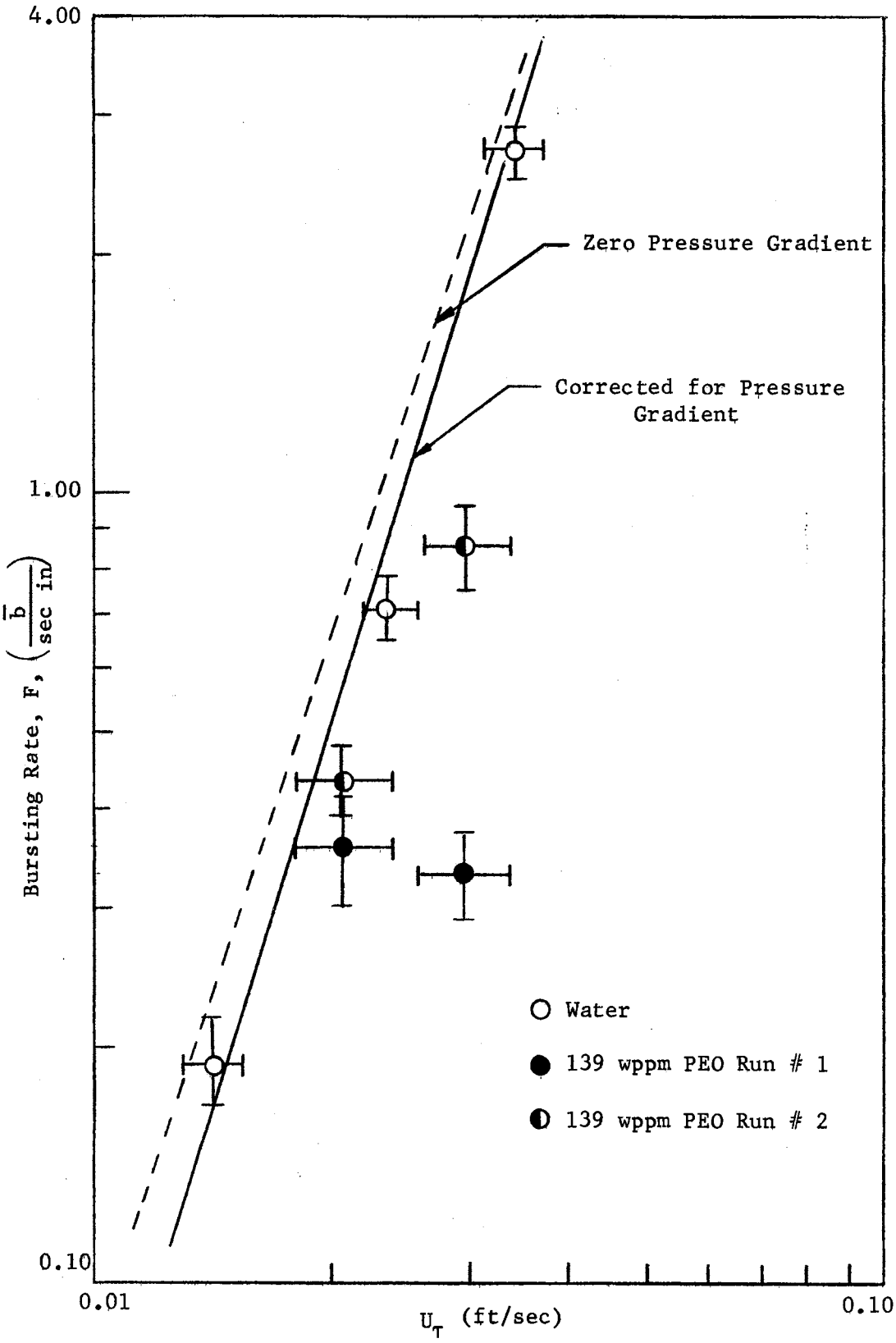

Figure 29. Bursting Rates in Water and Polymer Solution

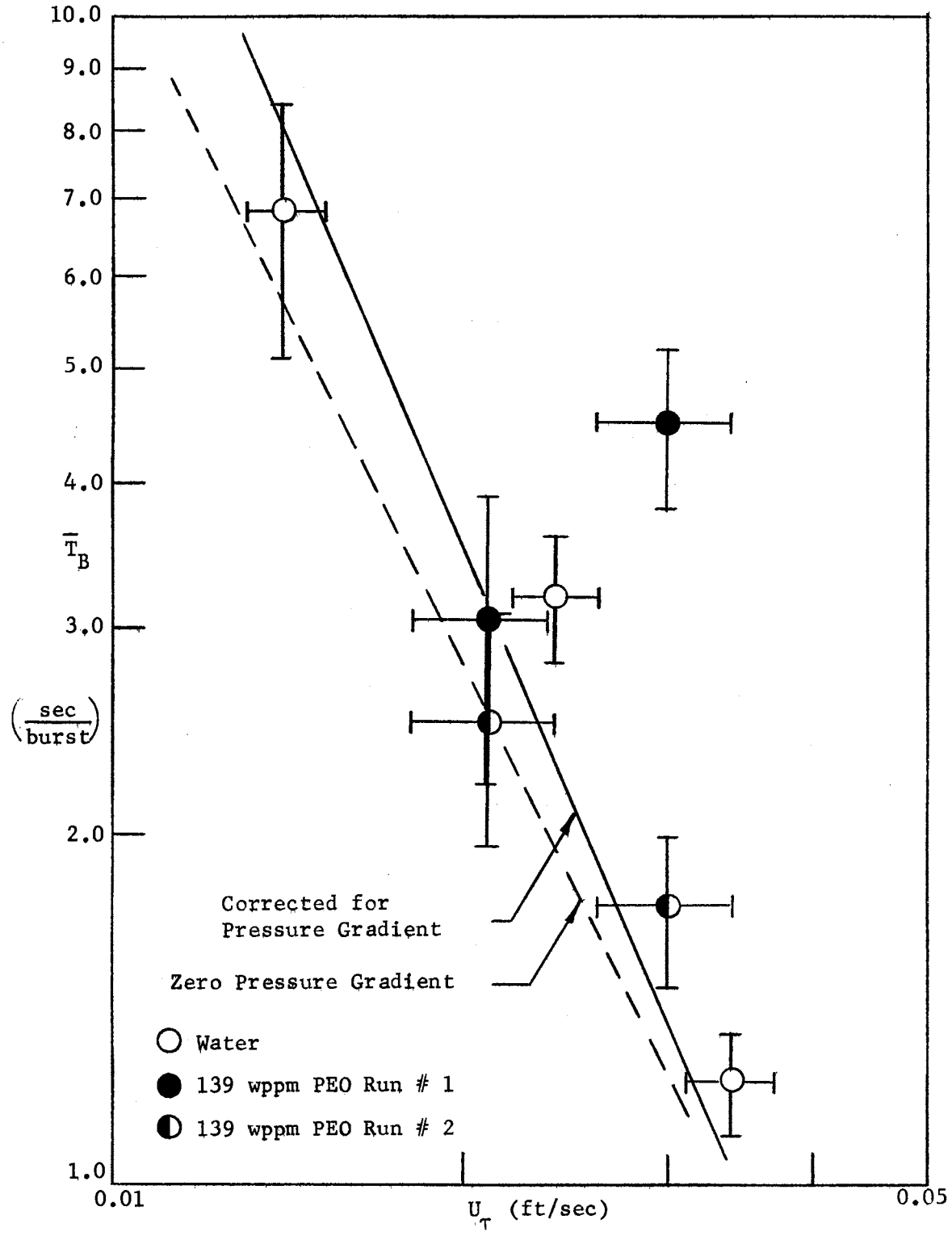

Figure 30. Average Time Between Bursts in Water and Polymer Solution.

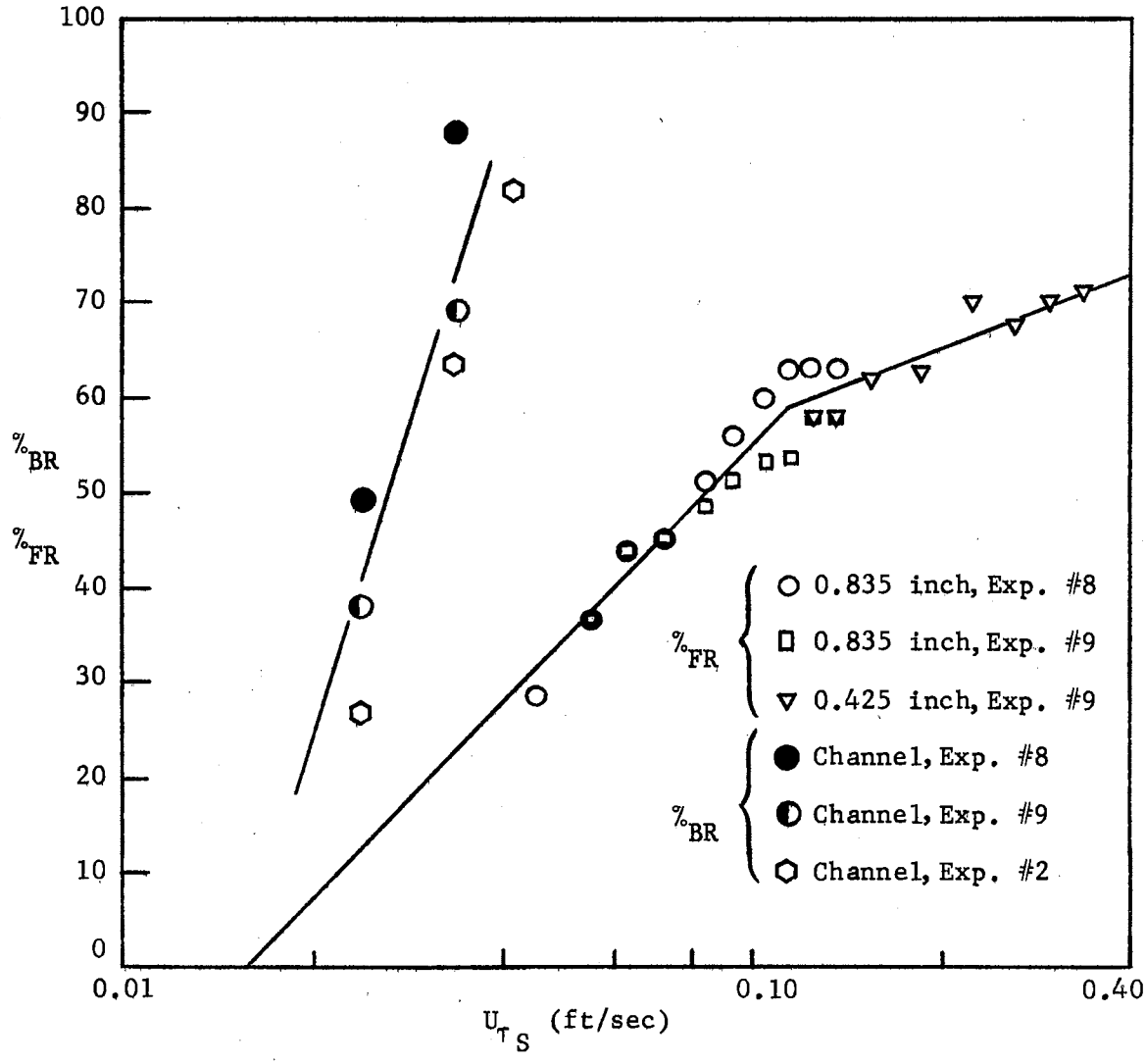

Figure 31. Per Cent Bursting Reduction and Per Cent Friction Reduction

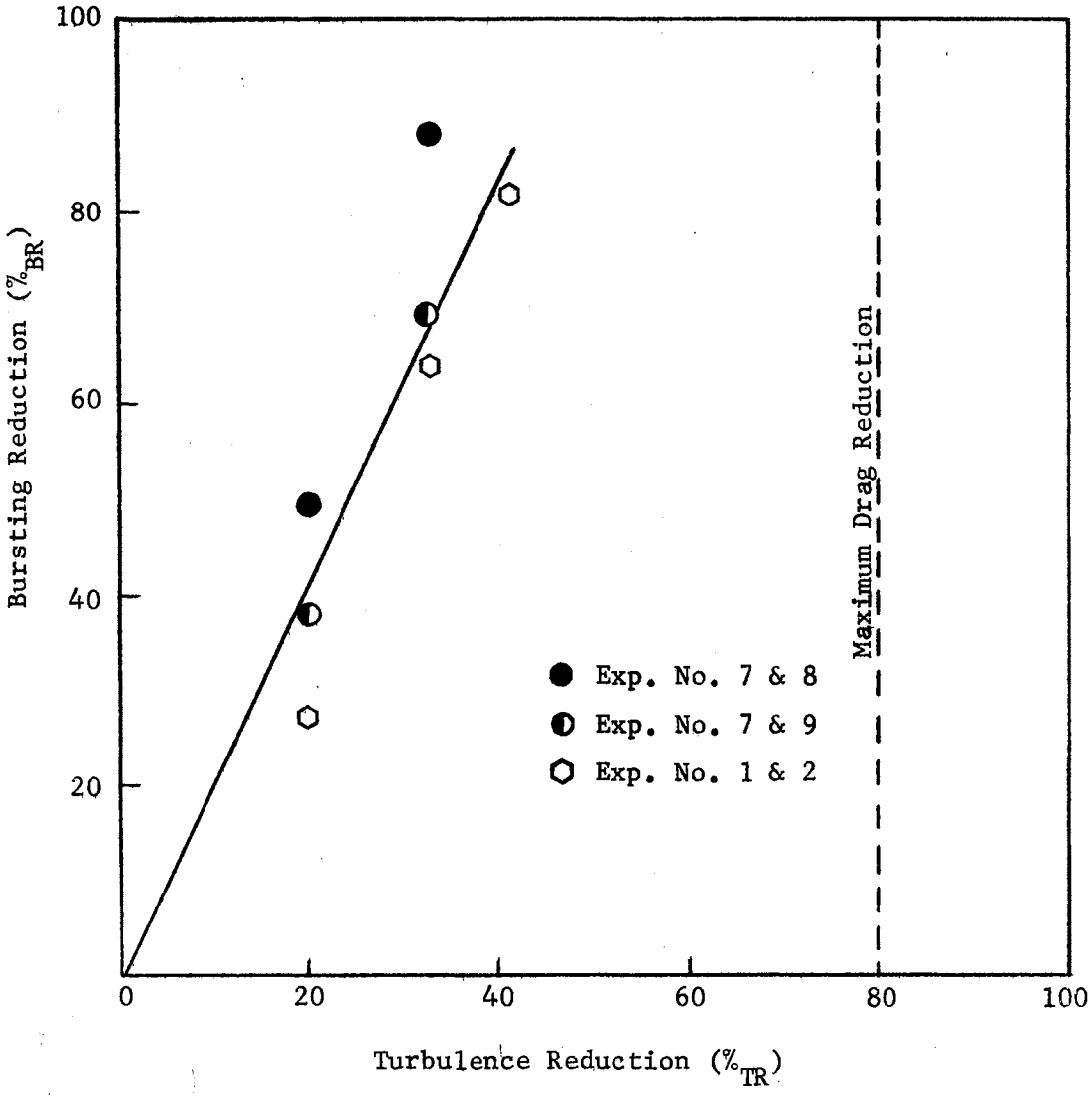

Figure 32. Per Cent Bursting Reduction in Relation to Per Cent Turbulence Reduction.

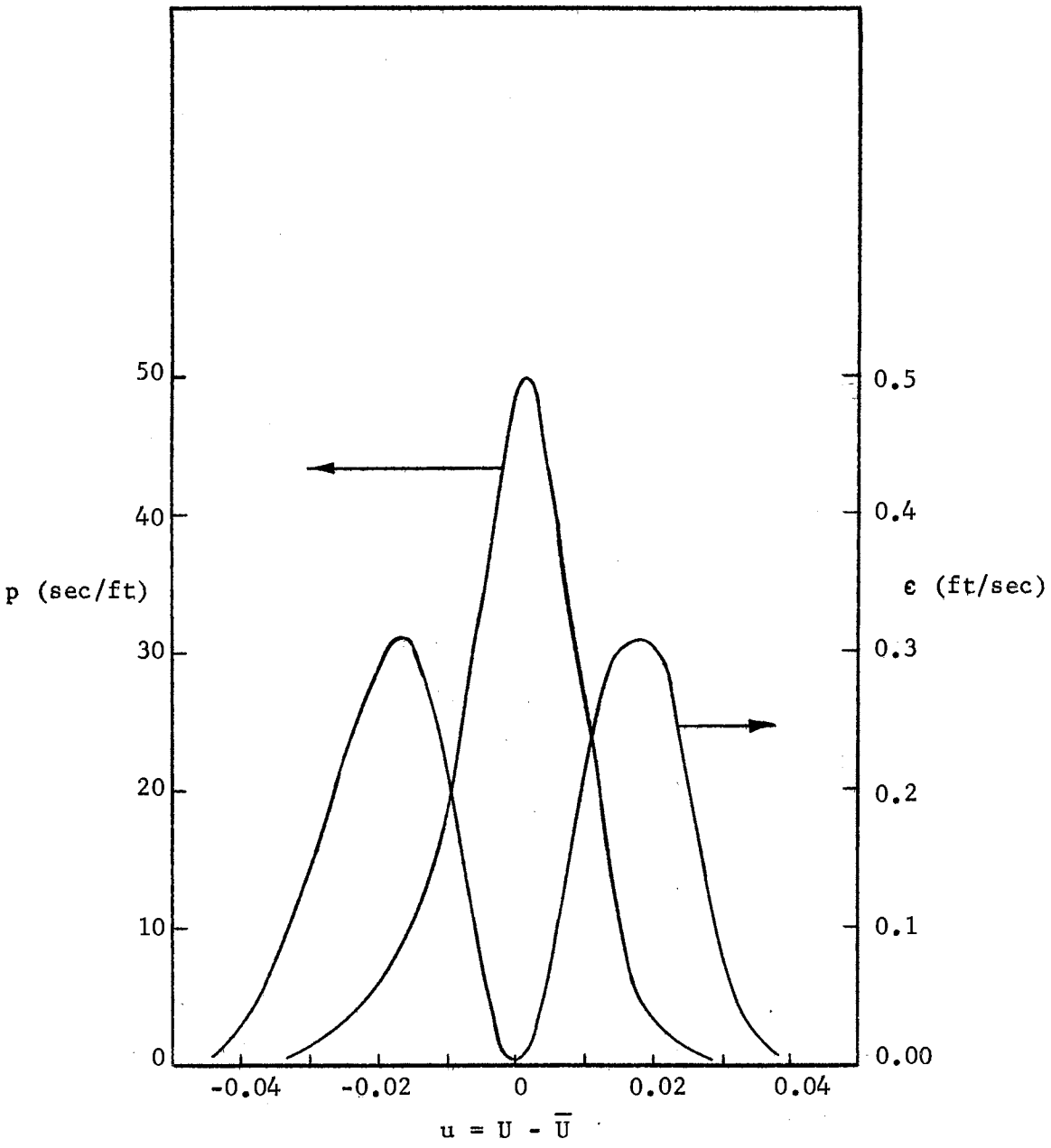

Figure 33. Probability Density Function and Energy Density Function, Uzkan (51)

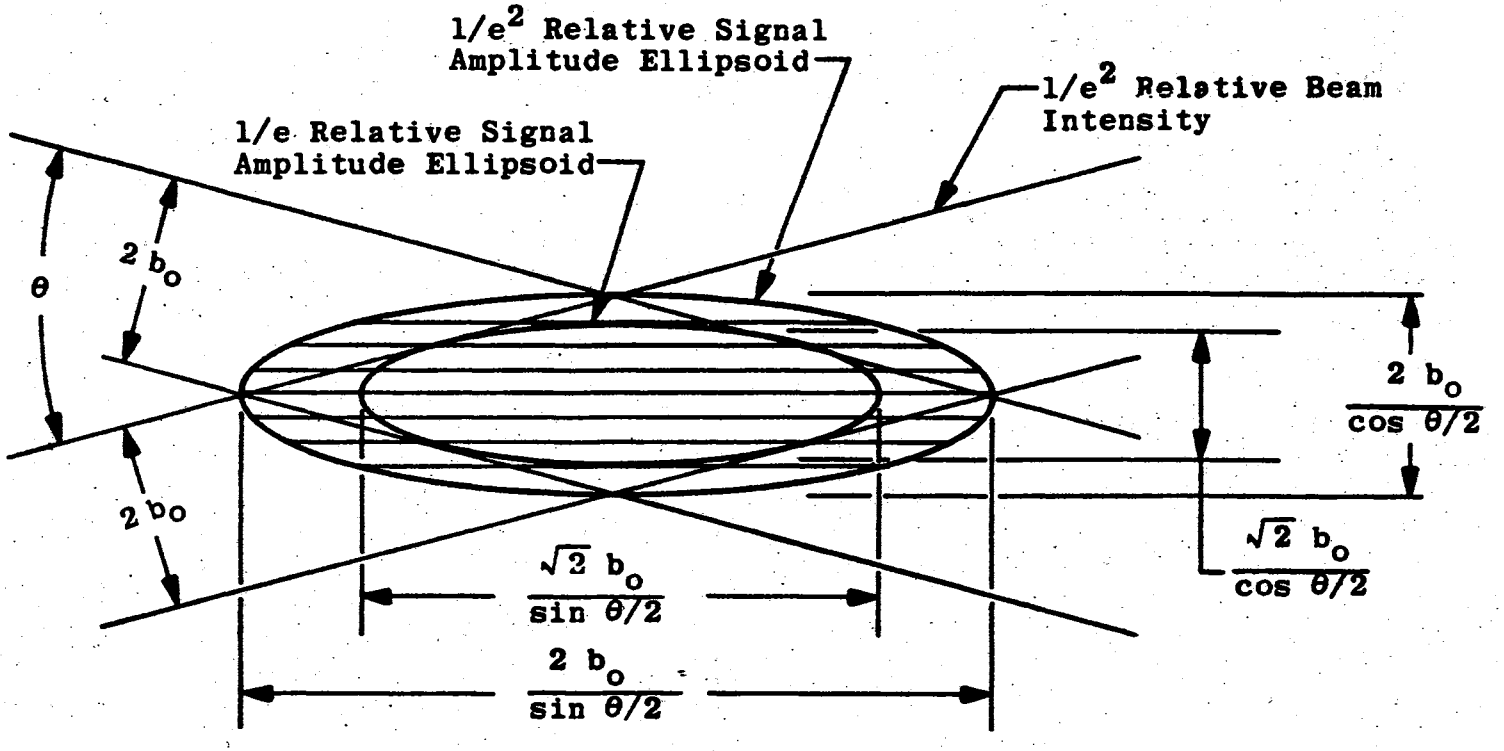

Figure 34. Relative Signal Amplitude Ellipsoids, Brayton, et al. (2)

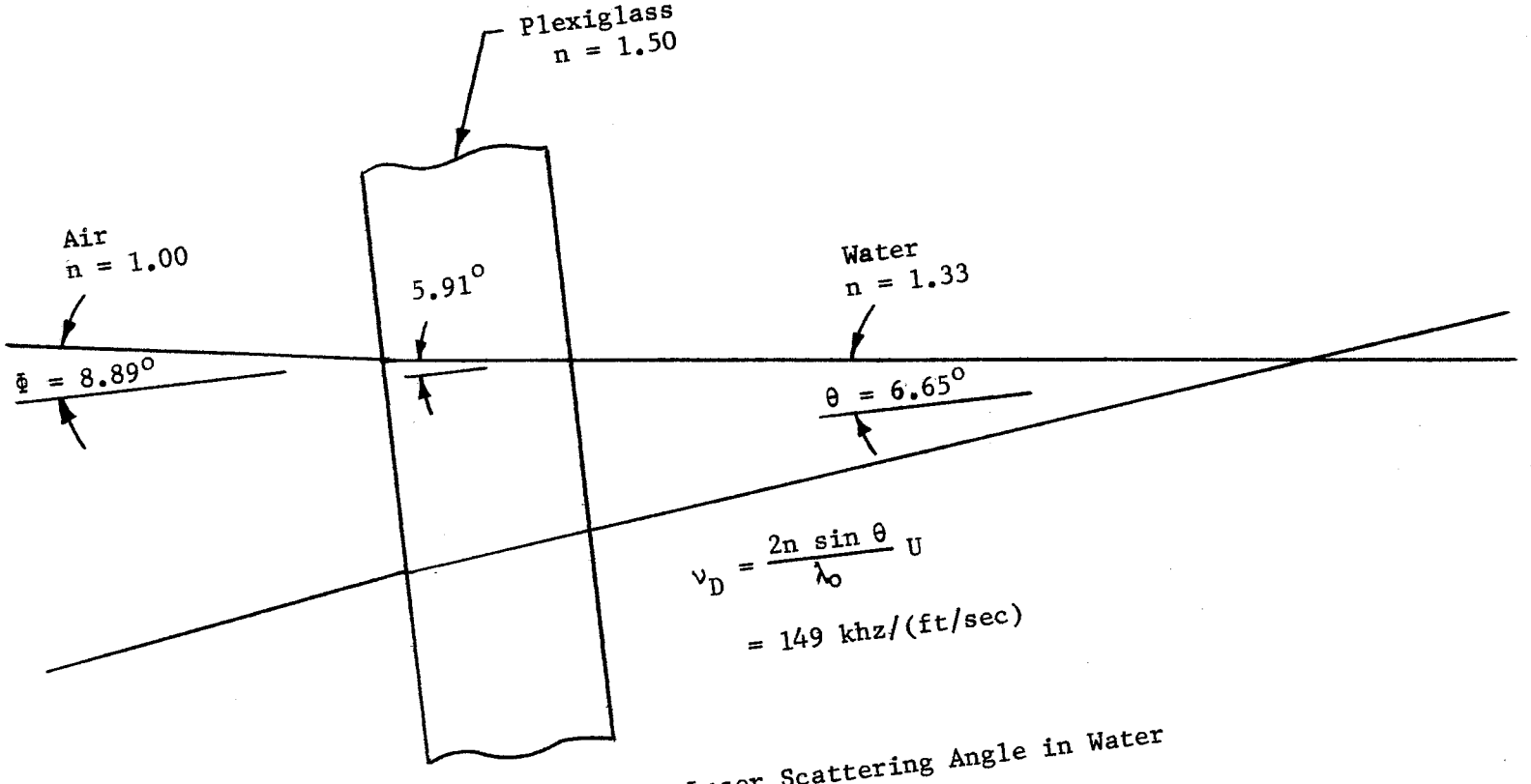

Figure 35. Laser Scattering Angle in Water

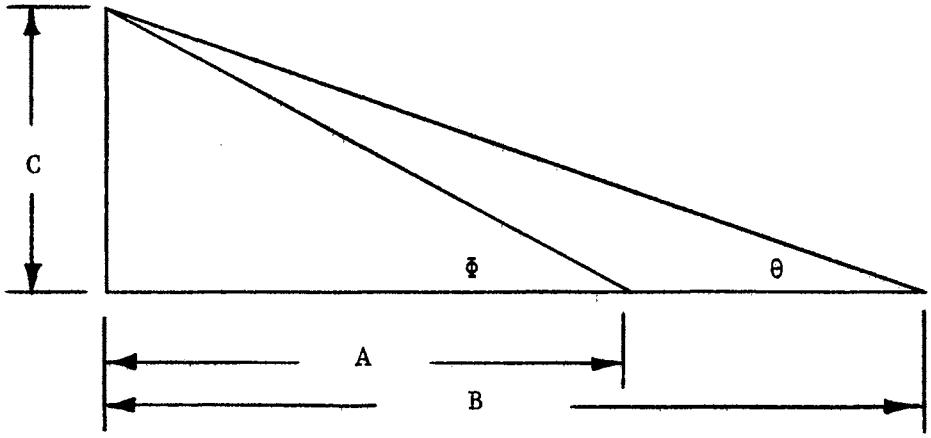

$$\text{Tan } \Phi = \frac{C}{A}$$

$$\text{Tan } \theta = \frac{C}{B}$$

$$B = A \frac{\text{Tan } \Phi}{\text{Tan } \theta}$$

$$B = 1.34\ A$$

Figure 36. Probe Volume Traverse Scaling Geometry

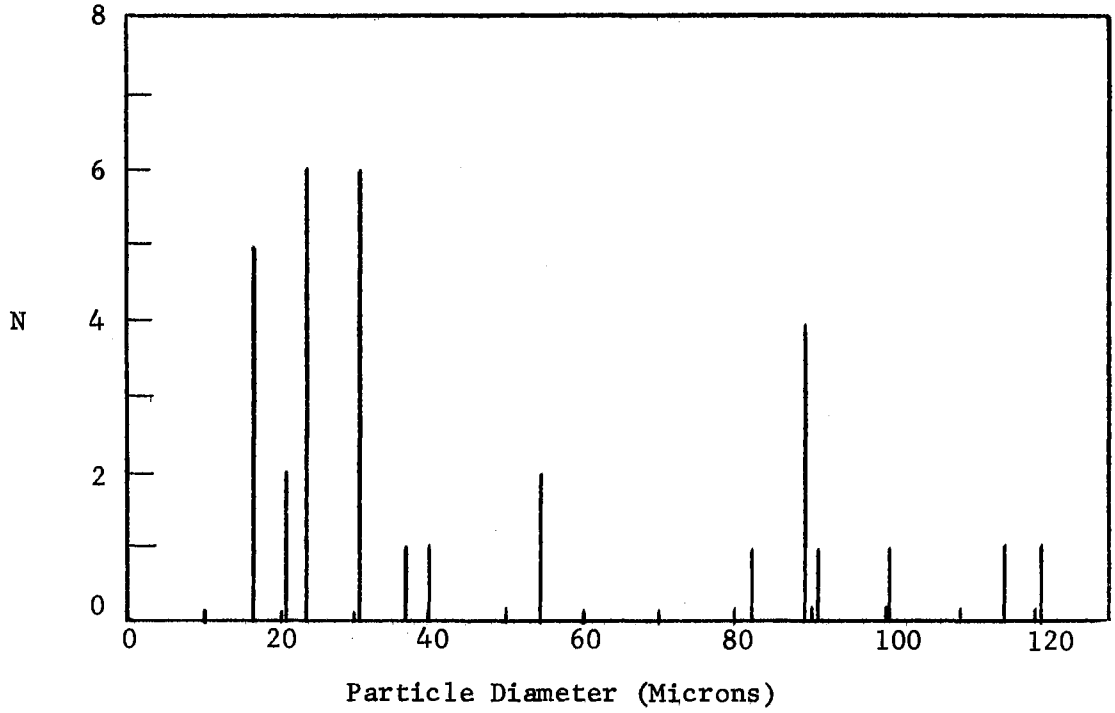

Figure 37. Scattering Particle Size Histogram

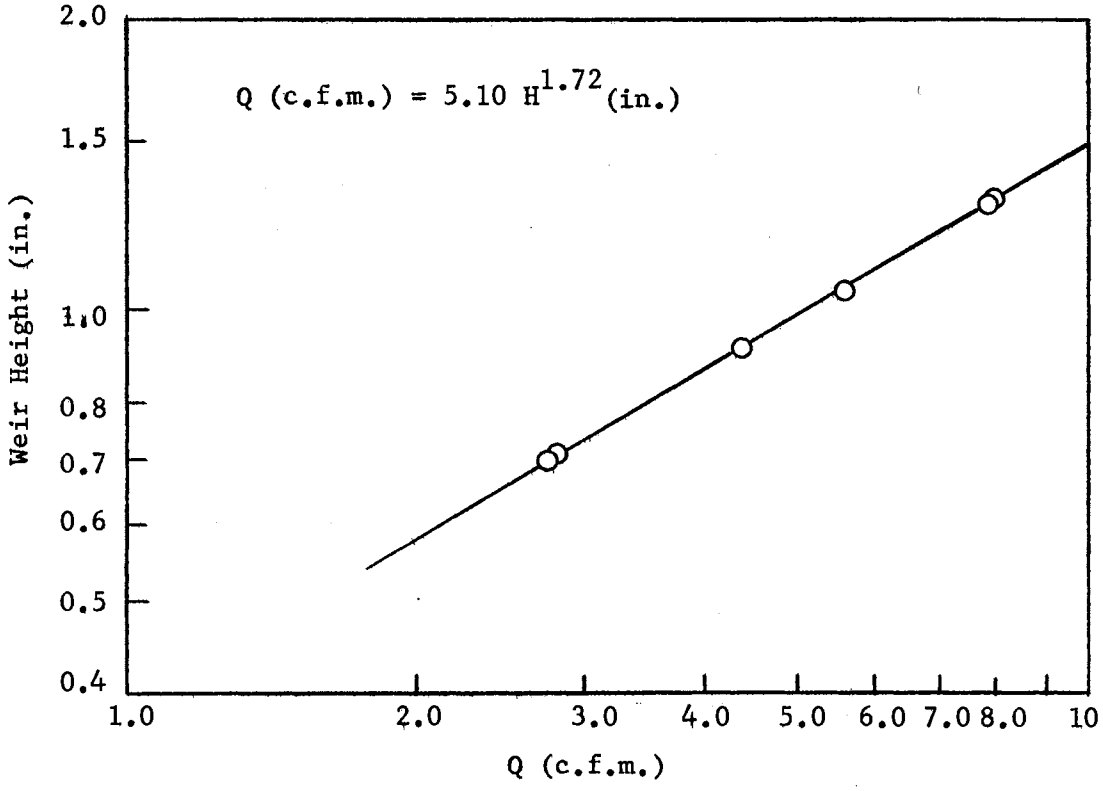

Figure 38. Weir Flow Meter Calibration Curve

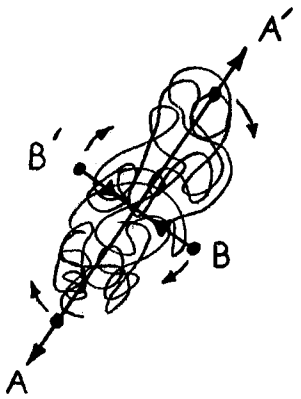

Figure 39. Macromolecule Rotating in a Simple Shear Field

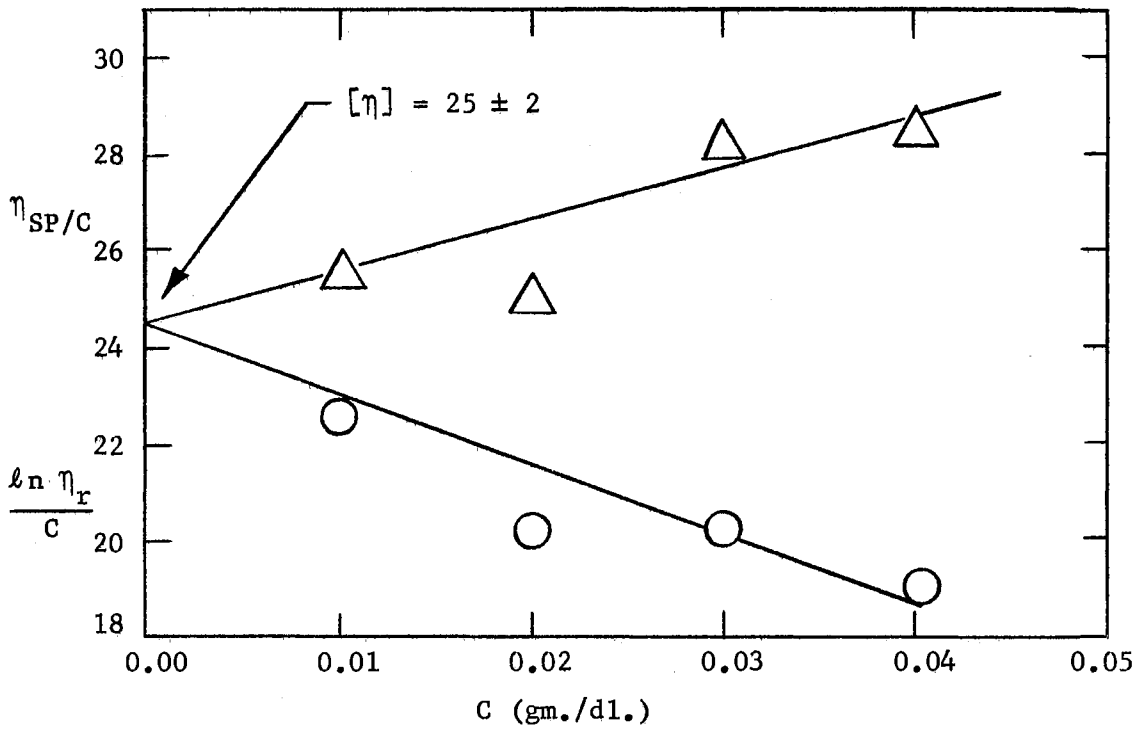

Figure 40. Intrinsic Viscosity [η] Extrapolation

VITA

George L. Custer Donohue

Candidate for the Degree of

Doctor of Philosophy

Thesis: THE EFFECT OF A DILUTE, DRAG-REDUCING MACROMOLECULAR SOLUTION ON THE TURBULENT BURSTING PROCESS

Major Field: Mechanical Engineering

Biographical:

Personal Data: Born in Wichita, Kansas, July 8, 1944, the son of Mr. and Mrs. G. E. Custer.

Education: Graduated from St. Thomas High School, Houston, Texas, in June, 1962; was enrolled in the Electrical Engineering Department at the Georgia Institute of Technology, 1962-64; received Bachelor of Science in Mechanical Engineering degree from the University of Houston in 1967; received Master of Science degree in Mechanical Engineering from Oklahoma State University in 1968; completed the requirements for the Doctor of Philosophy degree at Oklahoma State University in May, 1972.

Professional Experience: Co-operative Education student, NASA Manned Spacecraft Center, 1963-1967; graduate teaching assistant, Technical Institute, Oklahoma State University, 1970; research assistant, School of Mechanical and Aerospace Engineering, Oklahoma State University, 1971.